UNIVERSITY OF CALIFORNIA,
IRVINE

Title: Searches for Heavy Neutrinos and Supersymmetry in Dilepton Events at the ATLAS Experiment

DISSERTATION

submitted in partial satisfaction of the requirements
for the degree of

DOCTOR OF PHILOSOPHY

in Physics

by

Matthew Relich

CERN-THESIS-2013-275
02/12/2013

Dissertation Committee:
Professor Anyes Taffard, Chair
Professor Daniel Whiteson
Professor Arvind Rajaraman

2013

© 2013 Matthew Relich

DEDICATION

For all those who have helped me along the way...

TABLE OF CONTENTS

LIST OF FIGURES

LIST OF TABLES

ACKNOWLEDGMENTS

The work in this dissertation would not have been possible without the support of family and friends. First, I cannot thank enough my wife, Sayaka. Without her constant vigilance on my daily food intake, it is likely that I would have starved to death while writing analysis code. There are no words to describe how grateful I am for her patience in regards to my work schedule.

A special thanks to my Mother and Stepfather for their continued support and sound advice during difficult times. I would also like to thank my Father for teaching me at such a young age the importance of pursuing a career that you love, and not just something that is monetarily beneficial.

Thank you Anyes Taffard, for your patience and guidance that allowed me to reach this point in my career. Thanks are also due to Daniel Whiteson, for the meaningful analysis discussions and for maintaining a certain level of humor in the group. Also, thank you to the postdoctoral researchers Hideki Okawa, Ning Zhou, Serhan Mete, and Andrew Nelson for your willingness to work through problems and help me understand a variety of technical issues.

Thank you to the graduate students in the UCI ATLAS group that I have had the pleasure of working alongside: Steve Farrell, Kanishka Rao, Eric Albin, Brook Toggerson, and Michael Werth. Your help was invaluable. In addition, I would like to thank my fellow graduate students not involved directly with my research: Daniel Margala, Joseph McClenaghan, Daniel Fulton, Melissa Niiya, Trevor Gamble, Benjamin Ziemer, and Yavor Tatarov. The gaming nights and barbecues were a much needed distraction.

Finally, thank you to the University of California, the Department of Energy and CERN, for funding and providing the necessary tools in order for my work to be completed.

CURRICULUM VITAE

Matthew Relich

Research Interests

Searching for particle dark matter in the framework of Supersymmetry and searching for explanations of neutrino mass and the matter/anti-matter asymmetry at high energy experiments.

- Searched for heavy Majorana (Dirac) neutrinos in events with two leptons and at least one jet.
- Calibration of hadronic jets using events with photons and jets
- Search (ongoing) for Weakly produced Supersymmetry in events with two leptons and jets.

Education

University of California, Irvine

Ph.D., Physics, December 2013

- Thesis Topic: *Searches for Heavy Neutrinos and Supersymmetry in dilepton events at the ATLAS experiment.*
- Advisor: Professor Anyes Taffard

University of California, Irvine

M.S., Physics, 2010

University of Pittsburgh,

B.S., Physics, 2009

Journal Publications

[1] ATLAS Collaboration, *Search for heavy neutrinos and right-handed W bosons in events with two leptons and jets in pp collisions at* $\sqrt{s} = 7$ *TeV with the ATLAS detector,* [arXiv:1203.5420], Eur.Phys.J. C72 (2012) 2056 Phys. Rev. Lett. 109 (2012) 032001.

Conference Notes

[2] ATLAS Collaboration, *Search for direct slepton-pair and chargino-pair production in final states with two opposite-sign leptons, missing transverse momentum and no jets in 20* fb^{-1} *of pp collisions at* $\sqrt{s} = 8$ *TeV with the ATLAS detector,* ATLAS CONF Note [ATLAS-CONF-2013-049].

[3] ATLAS Collaboration, *Search for heavy Majorana neutrino and* W_R *in dilepton plus jets events with the ATLAS detector in pp collisions at* $\sqrt{s} = 7$ *TeV,* ATLAS CONF Note [ATLAS-CONF-2011-115].

[4] ATLAS Collaboration, *Probing the measurement of jet energies with the ATLAS detector using photon+jet events in proton-proton collisions at* $\sqrt{s} = 7$ *TeV,* ATLAS CONF Note [ATLAS-CONF-2012-063].

[5] ATLAS Collaboration, *In situ pseudorapidity intercalibration of the ATLAS detector using dijet events in* $\sqrt{s} = 7$ *TeV proton-proton 2011 data,* ATLAS CONF Note [ATLAS-CONF-2012-124]

Ongoing Projects

[6] Searching for direct gaugino production and direct slepton production with two leptons, missing transverse momentum and no jet at $\sqrt{s} = 8$ TeV, estimated completion by December, 2013.

[7] In-situ jet energy scale and its systematic uncertainty in proton-proton collisions at $\sqrt{s} = 8$ TeV with ATLAS 2012 data

PRESENTATIONS

[8] American Physical Society April Meeting, *Search for Heavy Majorana Neutrino in Same-Sign Dilepton Channel*, 2011.

[9] Physics at LHC 2012, *Search for Heavy Neutrinos and W_R in Events with Dileptons and Jets*, 2012.

[10] Hadronic Calibration Workshop *Status of Photon+Jet In-situ Results*, 2012.

[11] ATLAS Week, *Summary of 2012 In-situ Jet Energy Scale Results*, 2013.

[12] Large Hadron Collider Physics Conference, *Searches for Electroweak Production of Supersymmetric Neutralinos, Charginos and Sleptons with the ATLAS Detector*, 2013.

AWARDS

- Frederick Reines Fellowship, *University of California, Irvine*, 2009-2011
- *Magna Cum Laude* Graduation from *University of Pittsburgh*, 2009
- Halliday Award for Excellence in Undergraduate Research, *University of Pittsburgh*, 2008

TEACHING EXPERIENCE

University of California, Irvine

Teaching Assistant **September 2009 to June 2010**

- Instructor for undergraduate physics courses and labs for physics, mathematics, and engineering majors.

DESCRIPTION OF INVOLVEMENT IN ANALYSES

- **Searching for direct gaugino production and direct slepton production with two leptons, missing transverse momentum and no jet at $\sqrt{s} = 8$ TeV (ongoing)**
  I optimized signal regions for two production modes, direct slepton production and chargino pair production with intermediate sleptons. I performed two separate data-driven background estimates. The first is the background from fake-leptons, where fake-leptons are leptons from non-isolated sources. The second is a template method used to predict the high missing energy tails in Z+jet events due to fake missing energy. In addition, I will provide the final exclusion limits for two of the four signal grids. These results will be released as a paper in October 2013.
- **Search for direct slepton-pair and chargino-pair production in final states with two opposite-sign leptons, missing transverse momentum and no jets in 20 fb^{-1} of pp collisions at $\sqrt{s} = 8$ TeV with the ATLAS detector**
  I performed a data-driven background esimate to predict the contribution from fake-leptons in the signal region. In addition, I expanded and maintained a set of common code developed at UCI that has been used by many analyses within the SUSY working group.
- **In-situ jet energy scale and resolution and its systematic uncertainty in proton-proton collisions at $\sqrt{s} = 8$ TeV with ATLAS 2012 data (ongoing)**
  I calibrated the energy scale for hadronic jets using momentum balance against photons, and derived a systematic uncertainty on this calibration as a function of the jet energy. These results are then propagated to all physics analyses at ATLAS that are using jets. These in-situ results greatly reduce the overall uncertainty on the jet energy scale. These results will be included in the paper detailing the calibration of hadronic jets (2013).

- **Probing the measurement of jet energies with the ATLAS detector using photon+jet events in proton-proton collisions at $\sqrt{s} = 7$ TeV**
  My first contribution to the in-situ analyses where I made an independent cross-check on the final results propagated to all ATLAS analysers. I also expanded the analysis to include objects in the foward region of the detector.

- **In situ pseudorapidity intercalibration of the ATLAS detector using dijet events in $\sqrt{s} = 7$ TeV proton-proton 2011 data**
  I provided validation of the method in an independent event topology.

- **Search for heavy neutrinos and right-handed W bosons in events with two leptons and jets in pp collisions at $\sqrt{s} = 7$ TeV with the ATLAS detector.**
  I was the primary analyst. This was an extention of the previous analysis including the opposite-sign channel as well as seven times more data. I was responsible for generating all simulation for heavy neutrino signal points in the Effective Lagrangian framework. I performed all background estimates from simulation as well as using data driven techniques. I prepared the final plots and gave several of the internal talks as well as approval talks for the analysis. I wrote a majority of the internal documentation for the tools and methods used.

- **Search for heavy Majorana neutrino and W_R in dilepton plus jets events with ATLAS detector in pp collisions at $\sqrt{s} = 7$ TeV.**
  First analysis contribution which was done during my second year of graduate school. I performed background estimates from simulation as well as using data driven techniques. I calculated the cross-section limits on heavy neutrino production. I prepared the final plots, and gave several of the internal talks.

ABSTRACT OF THE DISSERTATION

Title: Searches for Heavy Neutrinos and Supersymmetry in Dilepton Events at the ATLAS Experiment

By

Matthew Relich

Doctor of Philosophy in Physics

University of California, Irvine, 2013

Professor Anyes Taffard, Chair

Two searches for new physics in events containing exactly two leptons performed at the ATLAS experiment are presented. The first searches for a new family of neutrinos in order to explain the observed small masses of the known neutrinos, while the second searches for the electroweak production of Supersymmetric particles. The Standard Model backgrounds are common between the two analyses, and an emphasis will be placed on the estimation techniques used. In both cases, the observed data candidates are found to be in agreement with the estimated Standard Model background.

Chapter 1

Introduction

Experimental particle physicists are akin to explorers of an uncharted territory. The current understanding of fundamental interactions and particle content can be expressed mathematically as the Standard Model (SM) of particle physics. This framework has been successful at describing physics up to the TeV scale. However, several observations have been made that are not consistent with the SM, which is a strong indication that the SM is not a fundamental theory of nature.

There are hints about which path should be further explored to go beyond the SM, two of which serve as the basis for the physics searches detailed in this dissertation. It has been over 50 years since the discovery that neutrinos can change flavors [2, 3] as they travel, providing strong evidence that neutrinos have mass, yet we have no experimentally verified way to explain how the known neutrinos obtain their mass. In addition, the cosmological evidence for dark matter [4] continues to compound, as well as the phenomenological models including particle dark matter, yet a viable dark matter candidate has not been observed.

In order to probe for physics beyond the SM, physicists have developed a new microscope in order to study, in great detail, the production and decay of fundamental particles with the

aim of discovering some new, exotic type of matter. This dissertation will present the results of two searches for new physics carried out using one such tool: the ATLAS detector at the Large Hadron Collider (LHC). These searches will probe for a new family of heavy neutrinos and Supersymmetry in events with exactly two leptons, which is a challenging final state where the prediction from the SM will be put to the test. Each of these searches did not yield a discovery of physics beyond the SM, however constraints for new physics signals in this particular final state have been placed.

An introduction to the particle content and forces explained within the SM is presented in Chapter 2, followed by the description of two theoretical hints for physics beyond the SM motivating the searches detailed in this dissertation in Chapter 3. Chapter 4 will introduce the Large Hadron Collider and an overview of the ATLAS detector used to carry out these searches. The physics objects that are reconstructed from the various components of the ATLAS detector are described in Chapter 5. These objects undergo a multitude of corrections, and one such correction for hadronic jets is described in Chapter 6. This is followed by the two searches for new physics carried out at ATLAS: the search for new, heavy neutrinos (Chapter 7) and the search for weakly produced Supersymmetry (Chapter 8). Finally, some concluding remarks are given in Chapter 9.

Chapter 2

The Standard Model of Particle Physics

The Standard Model (SM) of particle physics is a gauge theory based on the symmetry group $SU(3) \times SU(2) \times U(1)$. The mathematical framework of the SM is the most general way to describe fundamental particles and their interactions that is consistent with Special Relativity [5]. The $SU(2) \times U(1)$ group explains electroweak interactions and contains four generators, which will be the gauge bosons mediating the electromagnetic and weak forces. The physical bosons are the W^+, W^-, Z, and γ. $SU(3)$ is known as the "color" group as the generators associated with this group carry color charge. The eight generators are known as gluons and are responsible for the strong force. Gravity is the only fundamental force observed that is omitted in the SM. A major theoretical effort is ongoing in order to incorporate a quantum field theory of gravity with the other three fundamental forces.

All of the visible matter observed in the universe can be constructed from the fermionic fields present in the SM, which are known as the quarks and leptons. There are six types of quarks: up, down, charm, strange, bottom, and top. Each quark is a color triplet and carries

fractional electric charge. For each flavor there is a left- and right-handed chiral state, which are the gauge eigenstates of the SU(2) interactions [5]. The left-handed quarks pairs form a SU(2) doublet, and the right-handed quarks are singlets. The quarks participate in all interactions present in the SM, however only the left-handed quarks participate in the weak interactions. Isolated free quarks do not exist in nature. If one tries to pull a quark from a bound state, it quickly becomes energetically favorable to produce another quark to form a bound state [5]. This is known as color confinement and is the reason quarks are only found in a bound state [5]. A group of three quarks is known as a baryon (eg. proton and neutron) where a group of two quarks is known as a meson (eg. pion or kaon).

The leptons, on the other hand, do not carry color charge and do not participate in strong interactions. The charged leptons have electric charge $\pm$ 1 and are known as the electron, muon, and tau. Each charged lepton has a corresponding neutral lepton with electric charge 0 and are referred to as neutrinos (ν_e, ν_μ, and ν_τ). Like the quarks, the leptons also form left-handed SU(2) doublets and right-handed SU(2) singlets. A charged left-handed lepton and a neutral left-handed lepton form a SU(2) doublet and interact via the weak interaction, while the charged right-handed leptons form a SU(2) singlet and only interact via the electromagnetic interaction. There are no right-handed neutrinos in the SM. The basic properties of the leptons can be found in Table 2.2.

Generation	Particle	Mass [GeV]	Electric Charge [e]
1^{st}	u	2.3×10^{-3}	2/3
	d	4.8×10^{-3}	-1/3
2^{nd}	c	1.3	2/3
	s	0.95	-1/3
3^{rd}	t	173.5	2/3
	b	4.2	-1/3

Table 2.1: The properties of the quarks found in the SM. For each quark there is also a corresponding antiparticle with opposite electric charge.

The three interactions described in the SM are attributed to the exchange of a gauge boson,

Generation	Particle	Mass [GeV]	Electric Charge [e]	Stable
1^{st}	e	5.11×10^{-4}	-1	Yes
	ν_e	$< 2 \times 10^{-9}$	0	Yes
2^{nd}	μ	0.11	-1	No
	ν_μ	$< 2 \times 10^{-9}$	0	Yes
3^{rd}	τ	1.78	-1	No
	ν_τ	$< 2 \times 10^{-9}$	0	Yes

Table 2.2: The properties of the charged and neutral leptons found in the SM. For each lepton there is also a corresponding antiparticle with opposite flavor quantum numbers, and opposite charge for the charged leptons.

sometimes referred to as a vector boson. The gluon intermediates the strong interactions and is responsible for the observed quark bound states. The gluon is a massless particle. Three gauge bosons (W^+, W^-, and Z^0) are responsible for the weak interactions, and have rather large masses. The masses are given to these bosons during spontaneous symmetry breaking caused by the Higgs mechanism [5]. The final force carrier is the photon (γ) and is responsible for electromagnetic interactions. The photon, like the gluon, is a massless gauge boson. A summary of the bosons and their properties can be found in Table 2.3.

Force	Particle	Mass [GeV]	Electric Charge [e]
Weak	$W^\pm$	80.4	$\pm$ 1
	Z^0	91.2	0
Electomagnetic	Photon (γ)	0	0
Strong	Gluons (g)	0	0

Table 2.3: The properties of the SM gauge bosons that are responsible for intermediating the interactions between the fermions.

The symmetry in the SM is spontaneously broken by the non-zero vacuum energy of the Universe, which resulted in massive fundamental particles [5]. Spontaneous symmetry breaking is explained by the Higgs mechansim, and the physically realized Higgs boson was discovered in July of 2012 at the LHC [6, 7]. This important discovery is the final observation needed to complete the SM, and represents tremendous theoretical genius to have postulated correctly a mechanism to generate all masses within the SM.

Chapter 3

Beyond the Standard Model

With the discovery of the Higgs boson, the SM is complete. There are, however, both conceptual and phenomenological problems that are left unanswered. The analyses presented in this dissertation aim to address the origin of neutrino masses, the hierarchy problem, and dark matter.

Neutrinos have been observed to mix between flavor states [2, 3], which implies that they are massive particles. Neutrinos are massless in the SM, given that only left-handed neutrinos are incorporated and can therefore not gain mass via the Higgs mechanism. A potential solution is to introduce a new family of neutrinos, which will be further explored in Section 3.1.

In the SM, the Higgs boson mass recieves quantum contributions that act to drive the mass of the Higgs boson beyond the observed value [5]. In order to achieve the observed light Higgs boson mass, large cancellations of these quantum corrections are required without any theoretical motivation. This is known as the hierarchy problem. In addition, there is cosmological evidence that there exists a new kind of matter known as dark matter. This new kind of matter as been indirectly observed by studying the rotational curves of galaxies and finding that the luminous matter only accounts for a small fraction of matter required

for the galaxy to rotate as observed [4]. If there is some unseen matter that exists, there should also exist a particle (or particles) that constitute this matter. This conceptual and phenomenological problem could be solved by introducing a new symmetry, which is the subject of Section 3.2.

3.1 Heavy Neutrinos

The discovery of neutrino mixing [2, 3] unambiguously establishes that neutrinos are massive particles, contrary to their original definition within the SM. The mixing between flavor and mass eigenstates occurs due to a misalignment between the two bases and is described mathematically by the Pontecorvo-Maki-Nakagaw-Sakata (PMNS) matrix [5]. The addition of this mixing matrix is analogous to the mixing observed in the quark sector [5], and it has served as the foundation for neutrino oscillation studies.

While the PMNS matrix provides a framework to study neutrino oscillations and requires that the particles are massive, it does not describe how these neutrinos obtain their mass. In addition, the three observed neutrinos are found to be extremely light, ($\mathcal{O}(eV)$), which extends the fermion mass hierarchy by six orders of magnitude. Some extension of the SM particle content is required in order to generate masses for the neutrinos.

Generating these masses via the Higgs mechanism requires the addition of a right-handed neutrino to the SM and very small Yukawa couplings, which then begs the question: why is this coupling so small? An attractive idea that is associated with many Grand Unified Theories (GUT) is to introduce a new family of heavy neutrinos in order to explain the small masses of the observed SM neutrinos. In these frameworks, the observed light neutrino masses can be explained by the see-saw mechanism [8, 9, 10, 11] which, after diagonalization of the mass matrix, results in $m_\nu \approx m_{Dirac}^2/M_N$, where m_ν represents the mass of a known

neutrino, m_{Dirac} is the Dirac mass term, and M_N is the heavier mass of the new neutrino. As the new neutrino's mass is increased, the Dirac mass can take on more *natural* values, resulting in the observed small neutrino masses (m_ν).

This dissertation presents a search for hypothetical heavy neutrinos of either Majorana or Dirac type. If the see-saw mechanism is responsible for the low SM neutrino masses, then both the light and heavy neutrinos are Majorana particles. Majorana particles are defined to be their own antiparticles, which implies that all quantum numbers are identical. For Majorana neutrinos, this implies that they can violate lepton number, which could lead to interesting collider signature of same-sign pair of leptons in the final state. The Dirac case is considered as well, however the same-sign lepton channel is not accessible since Dirac neutrinos preserve lepton number.

3.2 Supersymmetry (SUSY)

A strong indication for physics beyond the SM is embedded in the mass of the Higgs boson. The SM is an effective theory that is valid up to a certain energy scale, which is typically denoted as Λ_{UV} and referred to as the ultraviolet cut-off. The cut-off isn't a physical parameter within the theory, but is a mathematical tool to regulate divergent integrals in order to keep the theory renormalizeable. The mass of the Higgs boson is dependent upon this cut-off scale as it receives quantum contributions from all particles that couple to the Higgs field that are either quadratically or logorithmically dependent on Λ_{UV} [12]. For example a fermion of mass m_f will contribute to the Higgs boson mass following,

$$\Delta m_H^2 = -\frac{|\lambda_f|^2}{8\pi^2}\Lambda_{UV}^2 + ... \tag{3.1}$$

where m_H is the Higgs boson mass and λ_f is the coupling strength [12]. The exact value of Λ_{UV} is unknown, however one possibility is that it is near the Planck scale $\mathcal{O}(10^{19})$. At the Planck scale the quantum effects of gravity can no longer be ignored [13]. If Λ_{UV} is at the Planck scale, the quantum contributions would have to cancel out precisely to one part in 10^{30} in order to achieve the observed Higgs boson mass at 125 GeV [13]. The need for this precise cancellation is known as the hierarchy problem.

One attractive option to deal with the hierarchy problem in a natural way is to exploit a feature that appears in these quantum contributions. The contributions outlined in Equation 3.1 are negative for fermions and positive for bosons. It is therefore possible to have the contributions from fermions cancel those from bosons by requiring a new symmetry relating these two types of particles, thus avoiding fine tuning of the theory parameters. This new symmetry is known as supersymmetry [12]. If every quark and lepton in the SM is given two complex scalar partners with $\lambda_s = |\lambda_f|^2$, then the corrections proportional to Λ_{UV} that appear in Equation 3.1 will cancel [12]. Fermions were used as an example, however the same is true for all SM particles coupling to the Higgs field. There are other potential solutions to the hierarchy problem, for example Technicolor [14], theories containing extra dimensions [15], and little Higgs models [16, 17], however these are not explored in this dissertation.

As mentioned, supersymmetry relates fermionic states to bosonic states. A supersymmetric transformation can be expressed as

$$Q|Boson>=|Fermion>, \qquad Q|Fermion>=|Boson>, \tag{3.2}$$

where Q denotes the operator that generates the transformation [12]. This transformation implies that if SUSY is realized in nature, then each SM particle should have a corresponding supersymmetric particle that has identical quantum numbers except that the spin is different

by 1/2 unit [12].

The minimal way to augment the SM to account for supersymmetry is known as the Minimal Supersymmetric Standard Model (MSSM), where the existing SU(3) $\times$ SU(2) $\times$ U(1) symmetry group is preserved . In the MSSM all of the single particle states are grouped into supermultiplets, where a supermultiplet is the irreducible representation of the supersymmetric algebra [12]. These supermultiplets contain both fermion and boson states, and the supersymmetric partners are referred to as superpartners. The superpartners will be denoted by including a tilde (eg. μ gets a superpartner $\tilde{\mu}$). The SU(2)-doublet supermultiplet will contain the left-handed fermions and scalar fermions (called sfermions), and the SU(2)-singlet supermultiplet will contain the right-handed fermions and sfermions [12]. Similarly, the SU(3) color gauge group containing the spin-1 gluon will receive a superpartner with spin-1/2 known as the gluino [12]. The SU(2) $\times$ U(1) group containing the spin-1 gauge bosons gain the spin-1/2 superpartners known as winos and binos [12]. The Higgs sector is more complex and cannot be simply modified by constructing one supermultiplet as in the other cases. Two SU(2)-doublets are necessary to give mass to the up- and down-type squarks, which will have both charged and neutral components collectively known as the higgsinos [12].

If SUSY were an exact symmetry of nature, all SUSY particles would have the same masses as their SM counterparts [12]. Since no SUSY particles have been observed, if SUSY exists, it must be a broken symmetry. There are many ways in which to break the symmetry which have implications for the phenomenology and sparticle masses, however the details of the breaking mechanism can be integrated out to yield an effective theory. This approach is taken in this dissertation.

There are over 105 independent parameters in the MSSM which will control the masses and production cross sections at the LHC. The number of parameters makes it experimentally difficult to search for SUSY at the LHC. Therefore, several assumptions are made based on

phenomenological constraints observed in the SM in order to reduce the parameter space to 19 free parameters [18]. These assumptions are:

1. No new sources of CP-violation
2. Minimal flavor violation
3. Degenerate first and second sfermion generation

The first two are motivated by the results of precision measurements, while the last is a useful simplification to work around constraints from the flavor sector [18]. The resulting 19 parameter model is known as the phenomenological MSSM (pMSSM).

Performing a search over these reduced 19 parameters is still experimentally challenging. Well motivated choices need to be made in order to construct manageable models with broad impact. Out of the 19 parameters in the pMSSM only a subset are relevant to searches for gauginos and sleptons performed in this dissertation: M_1, M_2, μ, and the 10 sfermion mass terms. The first three (M_1, M_2, and μ) parameters control the composition of the gaugino mass eigenstates [12]. They also dictate the relative masses of the observable gauginos. The 10 sfermion masses will dictate what sfermions are accessible at the LHC. The specific values of these parameters are discussed in Section 8.1.

To meet the the constraint of electroweak symmetry breaking in the SM, mixing between the neutral higgsinos ($\tilde{H}_u^0$ and $\tilde{H}_d^0$) and the neutral gauginos ($\tilde{B}$ and $\tilde{W}^0$), as well as mixing between the charged higgsinos ($\tilde{H}_u^+$ and $\tilde{H}_d^-$) and the charged gauginos ($\tilde{W}^+$ and $\tilde{W}^-$), does occur [12]. The mass eigenstates are referred to as neutralinos (χ_1^0, χ_2^0, χ_3^0, χ_4^0) and charginos ($\chi_1^\pm$, $\chi_2^\pm$) [12]. The composition of the mass eigenstates in terms of $\tilde{B}$, $\tilde{W}$, and $\tilde{H}$ are determined by the choices for the parameters mentioned previously (and discussed further in Section 8.1). In the MSSM and the pMSSM, there is no mixing in the 1^{st} and 2^{nd} generation sfermions, but there is in the 3^{rd}. This dissertation does not consider the 3^{rd}

generation, so a complete explanation of sfermion mixing is not given but can be found in [12].

A dark matter candidate exists within the pMSSM (and MSSM) where $R-$parity is conserved. $R-$parity represents a new symmetry in which the difference between baryon and lepton number is conserved and is denoted as,

$$P_R = (-1)^{3(B-L)+2s}, \tag{3.3}$$

where B and L are the baryon and lepton numbers respectively and s is the spin of the particle [12]. $R-$parity is not a prerequisite for an internally consistent theory, however it is well motivated as it prevents proton decay, which is a process that has yet to be observed [12]. If $R-$parity is conserved it would imply that sparticles are produced in pairs and that the lightest supersymmetric particle (LSP) could be a viable dark matter candidate. In the analysis that follows in Chapter 8 $R-$parity conservation is imposed following the pMSSM.

Initially, the dominant production mode for SUSY expected at the LHC was to be strong production involving squarks and gluinos due to the fact that the LHC is a hadron collider and the production cross section for these modes are larger as illustrated in Figure 3.1. However, the bounds on squark and gluino masses from searches performed at ATLAS and CMS have reached the point ($\mathcal{O}$(TeV)) where the weak production modes have competitive cross sections. The search presented in this dissertation targets the direct production of weak gauginos ($\tilde{\chi}_1^{\pm}\tilde{\chi}_2^0$ and $\tilde{\chi}_1^{\pm}\tilde{\chi}_1^{\mp}$) and sleptons ($\tilde{l}^{\pm}\tilde{l}^{\mp}$) in final states containing two leptons and missing energy.

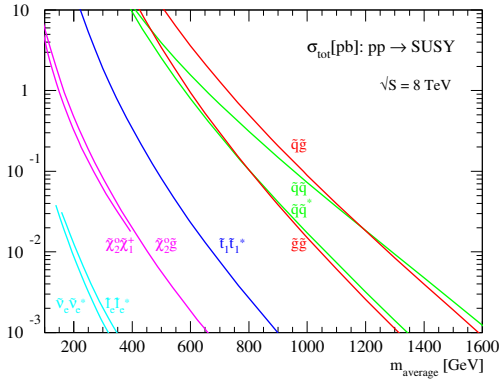

Figure 3.1: The projected cross section as a function of the average mass for pp collisions at $\sqrt{s} = 8$ TeV for a variety of production mechanisms [1].

Chapter 4

The LHC and the ATLAS Experiment

4.1 LHC

In 1994 the Large Hadron Collider (LHC) was approved and construction began to install this synchrotron in the 27 km underground tunnel that previously housed the Large Electron Positron (LEP) collider. This machine would surpass the Tevatron collider in center of mass energy ($\sqrt{s}$) by a factor of 14, however due to some initial complications the beam energy did not achieve the desired 14 TeV. The first dataset compiled prior to 2011 consisted of 7 TeV center of mass beam energy, which was increased to 8 TeV the following year. The center of mass energy is important as it sets an upper bound on the mass of particles produced at the collider.

The goal of the LHC is to reveal the physics that goes beyond the SM by giving physicists an ample dataset of the highest energy particle collisions manufactured in a laboratory setting. Each experiment has a detector sitting on the ring, as shown in Figure 4.1, which will record the resulting particles created in each collision. From this data one hopes that a statistically significant signature of a new particle will be found.

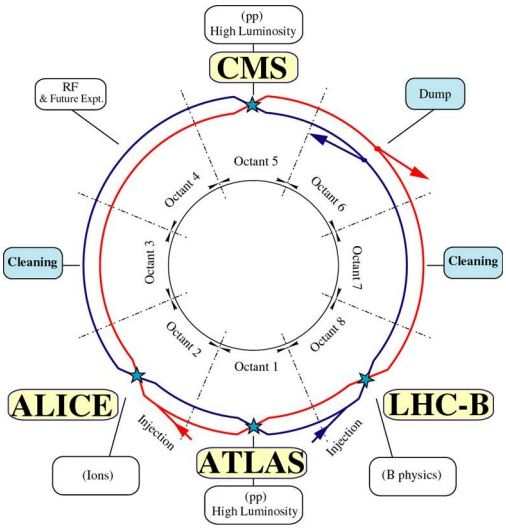

Figure 4.1: The layout of the LHC with the four main experiments: ATLAS, ALICE, CMS, and LHCb.

4.2 The ATLAS detector

The ATLAS detector is a general purpose particle detector designed to study a wide range of particles in a challenging environment. It has a cylindrical geometry, as seen in Figure 4.2, is symmetric in ϕ, and has forward-backward symmetry with respect to the point of interaction. The detector has multiple layers surrounding the beam pipe, which contain numerous systems targeting specific particle detection.

The inner most layer contains the inner detector which provides momentum and vertex measurements for particles, followed by the electromagnetic calorimeter which primarily serve to measure the energy and direction of photons and electrons. The next layer contains the hadronic calorimeter used for measuring the hadronic activity in the event, which is then followed by the last layer, the muon spectrometer, which primarily measure the momentum of muons by recording the amount of deflection caused by the magnetic field. These various systems work independently to record aspects of a given event, which is then combined to give a complete picture of the collision. The trigger system utilizes the information recorded by the various detector modules in order to filter the billions of collisions per second into a

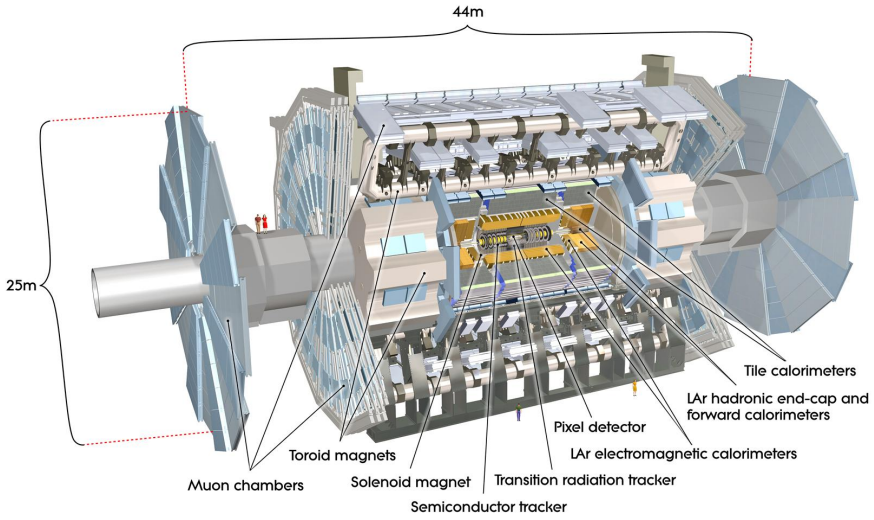

Figure 4.2: The ATLAS detector with labeling for the various components.

data set that is manageable. These components will be discussed in detail in Section 4.2.1 to 4.2.5.

4.2.1 Magnet System

The purpose of the magnet systems is to provide an intense magnetic field which will bend the energetic, charged particles. The amount of deflection, or the curvature of the track, that is recorded will yield a precise measurement of the particles momentum and charge.

The ATLAS superconducting magnet system consists of three basic entities: the central solenoid, the barrel toroid, and the end-cap toroid. The central solenoid encases the inner detector and provides a 2 T axial magnetic field with a peak magnetic field of 2.6 T. The barrel (end-cap) toroid produces a toroidal magnetic field with an average strength of 0.5 T (1 T). The toroid magnets have a complicated field structure which varies from 0.15 to 2.5 T in the barrel region and 0.2 to 3.5 T in the end-cap region [19].

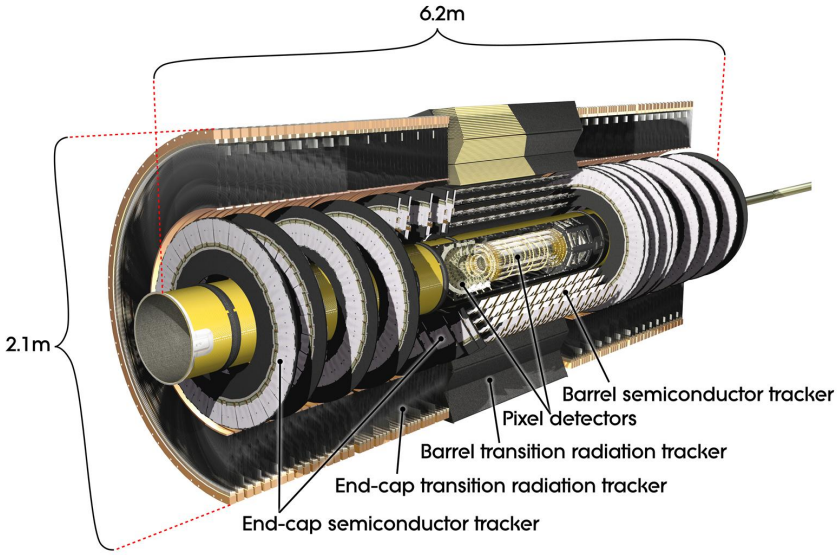

Figure 4.3: The ATLAS inner detector system labeling the Pixel detectors, SCT, and TRT.

4.2.2 Inner Detector

The inner detector (ID) must answer the physics demand for high precision measurements with fine granularity in events with large track density. Three separate detector technologies are incorporated to meet this demand. These detectors are the pixel detector, the semiconductor tracker (SCT), and the transition radiation tracker (TRT) pictured in Figure 4.3.

The pixel detector is the first element that the particle will interact with. It is designed to provide high resolution three dimensional measurements close to the interaction point, which allows for discrimination of promptly decaying particles and long-lived particles. The system contains three concentric barrels encasing the LHC beam pipe with an average radii of 4, 10, and 13 cm respectively, and 5 disks on either side of the barrels which yield the additional angular coverage. The system as a whole contains 140 million detector elements, which fit compactly in 50 μm in the R-ϕ direction and 300 μm in z [19].

The SCT encases the pixel detector and is comprised of four barrel and nine end-cap disks located on both sides of the interaction point. Each silicon detector is 6.36×6.40 cm^2. Two

detectors are bonded together to form a 12.8 cm long strip, and then two strips are glued together back-to-back to form a single module yielding a three dimensional measurement. These modules are aligned parallel (perpendicular) to the beam pipe in the barrel (end-cap). The detector contains 6.2 million readout channels with the ability to distinguish tracks that are separated by more than 200 μm [19]. This resolution allows one to identify leptons from converted photons as well as tag b-quarks and τ-leptons.

The final detector sub-system making up the ID is the TRT, which yields an additional 36 measurements per track. The TRT is again divided into two basic components, the barrel and end-cap, which are composed of 100k and 320k straws respectively that are embedded in polypropylene fibres. Each straw is 4mm in diameter and filled with a gas mixture of 70% Xe, 27% CO_2 and 3% O_2 [19]. In the center of the straw are 31μm tungsten wire anodes with a thin gold coat. As the particle passes between materials with different dielectric constants (eg. the polypropylene fibres and the gas mixture), transition radiation is emitted and then collected by the anodes. The transition radiation photons form a cone around the charged particle with half opening angle given by the β factor ($1/\gamma$). This relativistic factor is inversely proportional to the mass, and therefore offers a way to distinguish between particles of varying mass. This is particularly useful in differentiating electrons and pions, which otherwise have similar detector signatures.

4.2.3 Calorimetry

The ATLAS calorimeter system (Figure 4.4) consists of an electromagnetic (EM) calorimeter, providing fine granularity measurements for electrons, photons, and hadronic jets, and a coarser hadronic calorimeter, providing additional measurements for jets. The calorimeter coverage extends up to $|\eta| < 4.9$. Depth is an important factor to consider for the ATLAS calorimetry system in order to contain electromagnetic and hadronic showers and to prevent

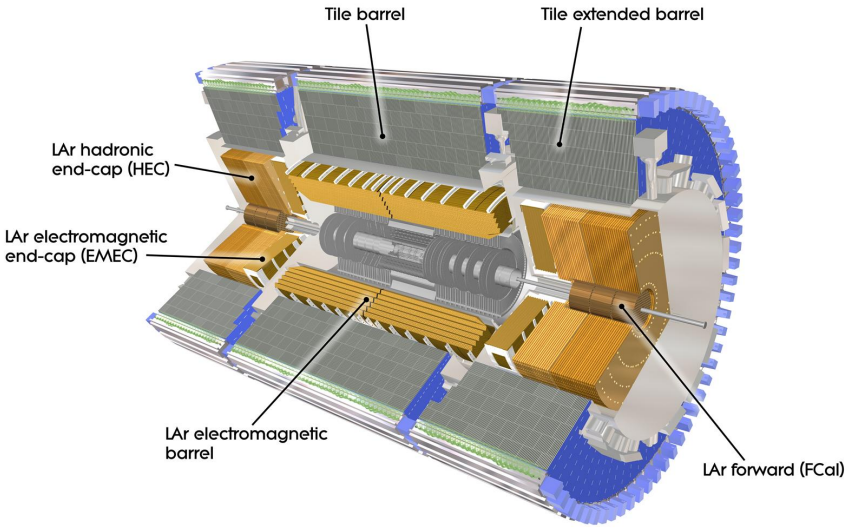

Figure 4.4: The ATLAS calorimetry system.

leakage into the muon systems. The typical unit of measure for this length is radiation length and interaction length. Radiation (interaction) length is defined as by the average amount of matter traversed by an electron (hadron) that reduces it's energy by $1/e$ through electromagnetic (hadronic) showering. To this end, the minimal thickness of the electromagnetic calorimeter is 22 (24) radiation lengths in the barrel (end-caps), which is adequate to provide good energy resolution from electromagnetic showers [19]. The hadronic calorimeter has approximately 9.7 (10) interaction lengths of active material in the barrel (end-caps), which will provide good resolution for high energy jets [19].

Liquid Argon EM Calorimeter The EM calorimeter is comprised of two barrel sections and two end-cap sections. The barrel is split into two separate pieces at z=0 with a gap of 4mm and providing coverage $|\eta| < 1.475$ [19]. The end-cap is split into two coaxial wheels, with the outer wheel covering $1.375 < |\eta| < 2.5$ and the inner wheel covering $2.5 < |\eta| < 3.2$. The EM calorimeter utilizes an accordion geometry (Figure 4.5) which interleaves lead and liquid Argon (LAr). The wave pattern introduced by the accordion geometry increases in amplitude radially, which is done to not only maximize azimuthal coverage but also to

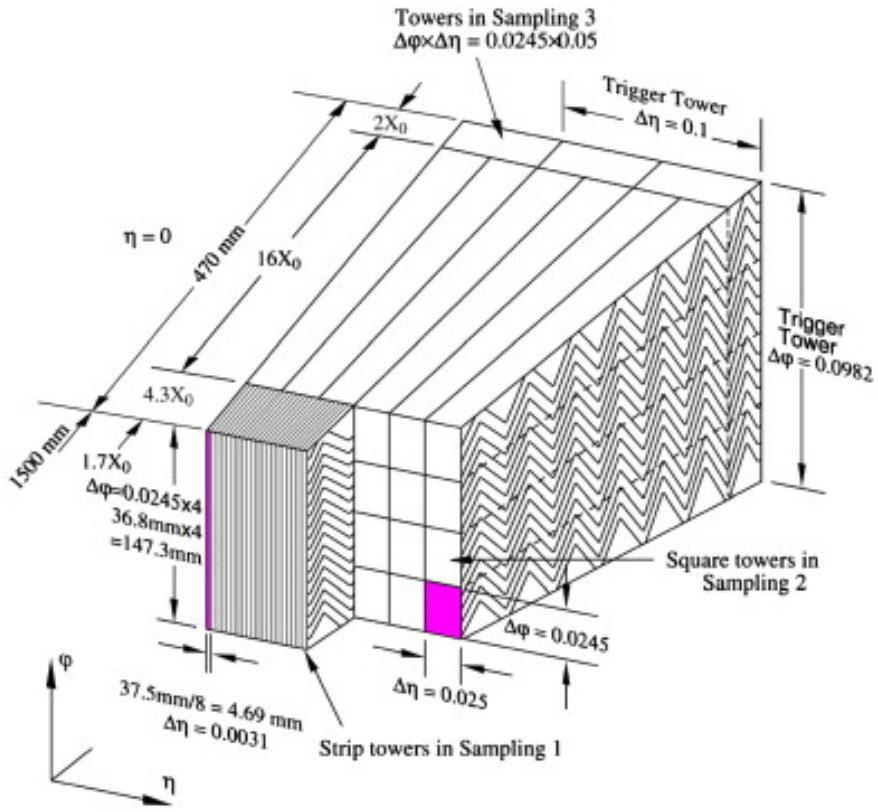

Figure 4.5: Three layers of the ATLAS electromagnetic calorimeter system highlighting the accordion geometry

provide excellent resolution, good linearity in the response, and an accurate measurement of the shower shape.

Hadronic Calorimeter The hadronic calorimeter contains three separate parts and utilizes different detector technologies. The central hadronic calorimeter lies just beyond the EM calorimeter and is made of interleaved steel and scintillating tiles [19]. The central calorimeter is divided into the barrel and two extended barrels, covering the range $|\eta| < 1.0$ and $0.8 < |\eta| < 1.7$ respectively. In the end-caps, just beyond the EM end-cap calorimeter, lies the LAr hadronic end-cap calorimeter. It employs a flat plate design of alternating copper and LAr scintillator, covering a range of $1.5 < |\eta| < 3.2$ [19]. The last piece of the hadronic calorimeter system is the forward LAr calorimeter, and is incased in the LAr hadronic end-cap calorimeter close to the beam pipe. This final piece provides uniform

calorimetric coverage ($3.1 < |\eta| < 4.9$), reducing energy loss in crack regions [19].

4.2.4 Muon Spectrometer

Muons, unlike electrons, do not stop in the calorimeter system, and it is for this reason that a dedicated outer layer is needed to record charge and directional information, which can then be used to extract the momentum of the particle. The ATLAS muon spectrometer provides coverage up to $|\eta| < 2.7$ and implements a three station design utilizing various detector technologies. Measurements for muon momentum rely on the toroid magnets to bend the muons trajectory giving a measurement in η as it passes through the muon spectrometer, and primarily is determined from the muon drift tube chambers (MDTs). The MDT barrel chambers form three concentric shells at 5, 7.5, and 10 m away from the beam axis [19]. Additionally, the end-caps contain large wheels placed perpendicular to the beam. The MDT chambers consist of three to eight layers of drift tubes, which are filled with a gas mixture of Ar and CO_2 [19]. As the muon passes through the tube, the gas is ionized and the free electrons are collected by the anode wire placed in the center. An illustration is given in Figure 4.6.

The forward region of the detector requires different technology given the background radiation levels and the overall counting rate. The cathode strip chambers (CSCs) provide an $\eta - \phi$ measurement, which when chambers are combined yields a three dimensional measurement. The maximum rate of the CSCs is nearly 10 times that of the MDT [19], and are designed to be radiation hard. The entire CSC system is made up of two disks with eight chambers each and provides coverage from $2 < |\eta| < 2.7$.

A complimentary system to the MDT known as the resistive plate chambers (RPCs) provide the orthogonal ϕ-coordinate measurement to the MDTs as well as support the muon trigger system in the range $|\eta| < 1.05$. As the name implies, it consists of two resistive, parallel plates

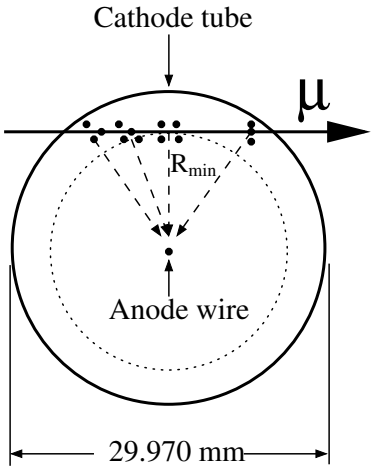

Figure 4.6: Cross-section of a MDT tube. The image depicts a muon traveling through a tube and ionizing the gas. The electrons then travel to the anode wire and the electrical signal is recorded.

with a 4.9 kV/mm electric field maintained between them. The muon traveling between the plates will ionize the gas, thus producing an electric signal that is readout.

In addition to the RPCs, the thin gap chambers (TGCs) also service the muon trigger system, providing trigger coverage for the forward region $1.05 < |\eta| < 2.4$. Also, like the RPCs, they provide the azimuthal coordinate measurement to compliment the MDTs. The chambers are defined by a gas volume containing a wire plane and two cathodes, which provide the radial bending coordinate [19]. The cathodes can be segmented into strips to provide additional measurement in ϕ [19].

4.2.5 Trigger System

The collision rate at ATLAS happens at such a high frequency that it is impossible to record all events. Therefore a triggering system has been developed to filter events based on the characteristics of the objects in a given event.

The ATLAS trigger system consists of three levels: Level 1 (L1), Level 2 (L2), and the event

filter. The L1 trigger utilizes custom made electronics specific to the experiment, while the High-Level Trigger (HLT), which consists of the L2 and event filter levels, is primarily software based [19].

The L1 trigger searches for signatures containing high p_{T} leptons, photons, or jets, as well as events containing appreciable $E_{\mathrm{T}}^{\mathrm{miss}}$ and flags them for further processing. The maximum processing rate from the L1 trigger is 75 kHz [19]. The L1 trigger creates regions of interest (ROI) which is used to seed the L2 trigger [19]. The L2 trigger has access to the full detector resolution using the objects within this ROI [19]. The L2 trigger checks the properties of the trigger-objects for quality criteria to insure the events that are recorded contain useful physics objects. The L2 trigger further reduces the event rate to below 3.5 kHz [19]. The final stage includes further event reduction by utilizing offline analysis procedures to analyze the contents of the event to reduce the rate to approximately 200 Hz [19]. At this stage, the fully reconstructed and calibrated objects are used in order to make the decision of whether or not to write the events to disk.

The choice of trigger will dictate the amount of data available to an analysis. The amount of data is expressed as the integrated luminosity,

$$\mathcal{L} = \frac{\mu n_b f_r}{\sigma_{inel}}, \tag{4.1}$$

where μ is the average number of interactions per bunch crossing, n_b is the number of bunch crossing per revolution, f_r is the frequency of revolutions, and σ_{inel} is the proton-proton inelastic cross section [20, 21]. These parameters are measured using two detectors: LUCID and ALFA [19]. These will record the total luminosity delivered to the ATLAS detector, which is then filtered by the trigger system. This luminosity is crucial to know with a high degree of accuracy in order to perform precision measurements at the LHC.

Chapter 5

Object Reconstruction

Offline algorithms are needed to reconstruct physics objects (eg. electrons) from detector hits and energy deposits recorded by the ATLAS detector. The reconstruction algorithms and approaches for each object are described in Section 5.1 to Section 5.5.

5.1 Electrons

Electron reconstruction begins by selecting calorimeter energy deposits recorded in a 5×5 (4×4) $\eta - \phi$ region of calorimeter cells in the barrel (end-cap) that are passed to a sliding window reconstruction algorithm [19]. An electromagnetic cluster is then built around this seed. The size of this window is optimized to collect a majority of the shower energy while also preserving energy resolution and reducing the impact of noise, pile-up, and energy leakage [19].

Additional tracking information is provided by the inner detector in order to start a complimentary reconstruction algorithm. This algorithm takes good quality tracks as a seed and extrapolates to a calorimeter cluster [19]. This algorithm will rely more on the inner detector

identification capabilities, and is useful at recovering low p_{T} electrons [19].

Information from both the inner detector and the EM calorimeter are used to identify the quality of an electron. Selection on shower shapes, track information and information from the reconstruction algorithms are combined to identify electrons [19]. The identification requirements are needed in order to separate electrons from jets that have properties similar to electrons. A set quality criteria have been developed in ascending order of background rejection power and are known as loose, medium and tight (tight containing the strictest requirements). These criteria qualitatively describe the requirements on the electron:

- **Loose** cuts require basic selection on shower shape and loose matching between tracks and calorimeter cluster [19, 22].
- **Medium** cuts will include the loose requirements as well as additional selection on the first layer of the EM calorimeter to further distinguish isolated electrons from non-isolated electrons and hadrons. Additional requirements on the number of hits in the ID are required for the track [19, 22].
- **Tight** cuts will include the medium requirements as well as a tighter matching criteria between calorimeter clusters and inner detector tracks. Additional requirements on the number of hits in the inner detector modules and calorimeter energy isolation are also imposed [19, 22].

5.2 Photons

Photons share the same sliding window algorithm with electrons, which is seeded by calorimeter cells [19]. Photons are broken into two categories: converted and unconverted photons. Converted photons will have one or two associated tracks originating from a vertex that

is displaced from the primary vertex, whereas unconverted photons will have no associated tracks in the inner detector. This distinction is useful in separating electron candidates from photon candidates. A set of quality criteria on shower shape and the presence of tracks has been optimized to further separate photons from other particles depositing energy in the calorimeter (eg. neutral pions) [19].

5.3 Muons

Three reconstruction strategies are employed to identify and measure muons with momentum ranging from approximately 3 GeV to 3 TeV [19]. The first reconstruction method is known as *Standalone* and it solely relies on the muon spectrometer over the region $|\eta| < 2.7$. The second utilizes information from both the inner detector and the muon spectrometer over the range of $|\eta| < 2.5$ and is known as *Combined*. The final strategy is called *Segment Tag* and uses the inner detector track information and a single muon spectrometer segment [19].

Standalone muons are reconstructed from muon spectrometer tracks that have been propagated back to the interaction point [19]. The energy of the muon is corrected by estimating the energy lost in the calorimeter depending on the amount of material traversed. The energy loss (dE/dX) is taken as the maximum from either the parameterized expected energy loss or what is measured in the calorimeter [19].

Combined muons are built by matching tracks from the inner detector to those in the muon spectrometer within the region $|\eta| < 2.5$ [19]. The matching is done by taking the inner detector track $\mathbf{T}_{ID}$ with the covariance matrix $\mathbf{C}_{ID}$ and a muon spectrometer track $\mathbf{T}_{MS}$ with the covariance matrix $\mathbf{C}_{MS}$ in order to get the combined track:

$$\mathbf{T}_{combined} = (\mathbf{C}_{ID}^{-1} + \mathbf{C}_{MS}^{-1})^{-1}(\mathbf{C}_{ID}^{-1}\mathbf{T}_{ID} + \mathbf{C}_{MS}^{-1}\mathbf{T}_{MS}) \tag{5.1}$$

where $\mathbf{T}$ is a five component vector given as,

$$\mathbf{T} = (z_0, d_0, \phi, \theta, q/p), \tag{5.2}$$

where z_0 and d_0 are the impact parameters, ϕ and θ are spacial coordinates, q is the charge of the muon, and p is the momentum [23]. Using both sets of information will significantly improve the momentum resolution for muons with energy below 100 GeV, and act to discriminate between muons and charged pions that punch through the calorimeter [19].

Some muons do not have the required number of segment hits in order to build a muon spectrometer track. Segment tagged muons are built in this case utilizing the inner detector tracks and extrapolating to the inner muon stations to associate the track with a muon spectrometer segment not associated with a track [19]. These typically recover low p_{T} muons that did not deposit enough energy in the muon spectrometer or muons not reconstructed due to geometrical acceptance.

5.4 Jets

There are three types of jets used at ATLAS: truth jets, track jets, and calorimeter jets. Jets are reconstructed using the anti-k$_T$ algorithm [24] with two radial distance parameters, $R = 0.4$ and $R = 0.6$. It should be noted that there exists other distance parameters, however they are used for specific applications while $R = 0.4$ and $R = 0.6$ jets are predominantly used for physics analyses. The input to the algorithm defines the type of jet.

Truth jets are created from stable particles and are only available in simulated events. Track jets are made from reconstructed inner detector tracks. Calorimeter jets are constructed from energy deposits in the calorimeter system. Each reconstructed jet has a particular usage, and this dissertation will focus on calorimeter jets as they are used for physics analyses.

Calorimeter jets are built from topological clusters (topo-clusters) of energy measured in the calorimeter [19]. The deposits are scattered in η-ϕ space and can be thought of as a two-dimensional matrix, where the matrix entries are the energies in those particular cells. These cells are then grouped based on their signal to noise ratio to form the energy clusters, which are measured at electromagnetic (EM) scale. The EM scale implies that the shower energy has been calibrated assuming that the shower is electromagnetic, and not hadronic which has a different calorimeter response. This represents the first measurement of the jet and it's corresponding EM scale energy, and will be referred to as an EM-jet [25]. Additional corrections to take into account the non-compensating nature of the ATLAS calorimeter come in the form of local cluster weighting (LCW) which defines the second type of calorimeter jet, LCW-jet. The responses for an electromagnetic shower and a hadronic shower are different, and the LCW method accounts for this. The LCW method will try to classify energy deposits used to make the jet as coming from electromagnetic or hadronic showers and then correct each fraction by their respective responses [25]. This is in then combined to form the jet energy prior to any scale or resolution corrections.

Additional corrections to the jet direction and energy are applied offline after the reconstruction phase. The goal of these corrections are to take the measured jet energy and correct back to the original parton energy, as measured by the detector. This is done in various steps described in detail in Section 6.1.

In physics analyses it is important to distinguish jets originating from the primary vertex and those from secondary vertices in the event. The numerous amount of vertices in the event is known as pile up, and is a general feature of crossing bunches of protons during the collision. In order to do this, a variable known as the jet vertex fraction (JVF) has been defined as the fraction of tracks in the jet cone originating from the primary vertex to the total number of tracks. Jets having JVF close to one have a large fraction of are from the primary vertex. Jets with low JVF are constructed with tracks not originating from the

primary vertex.

b-tagging Identifying whether or not a particular jet originated as a b-quark can be a powerful tool in searching for new physics. ATLAS employs several b-tagging algorithms, three of which have been utilized in this dissertation. Two were used in the search for heavy neutrinos (Chapter 7), which use the secondary vertex [26] and an impact parameter based [27] algorithms. The last was used in the search for supersymmetry (Chapter 8) and utilizes a multivariate approach which combines the results of the previous two algorithms [28]. The choice of the algorithm was made based on the recommendations from the b-tagging performance group within ATLAS as well as what algorithms were available to the analyzers at the time the analyses were carried out.

5.5 Missing Transverse Momentum (MET)

Missing transverse momentum ($E_{\mathrm{T}}^{\mathrm{miss}}$) is an important variable needed in searches where non-interacting particles (eg. SM neutrino or LSP in SUSY) are expected to escape the detector without being measured. The full coverage in ϕ of the ATLAS detector allows this measurement to be possible. Missing transverse energy is calculated by taking all of the recorded objects and imposing energy conservation in the transverse plane. Any imbalance is assigned as missing energy.

One way to construct $E_{\mathrm{T}}^{\mathrm{miss}}$ is to follow an ordered vector summation of all the reconstructed and identified objects in the event. This is the preferred method to calculate the missing energy since all physics objects will be included with their appropriate energy calibrations. The vector sum of all the objects is then projected onto the transverse plane (perpendicular to the beam pipe). This vector is then inverted such that it balances the system of objects used in the event. The order in which each object is included in the $E_{\mathrm{T}}^{\mathrm{miss}}$ calculation is

electrons, photons, hadronically decaying τ-leptons, jets and muons [19]. This ordering is important, as it will take into account the overlap between objects. After all reconstructed and identified objects are included, additional calorimeter cells that survive a series of noise cuts are also calibrated and included in the $E_{\mathrm{T}}^{\mathrm{miss}}$ calculation. These objects are known as the "soft terms", and will be a necessary ingredient for a background prediction method described in Subsection 8.3.4. It is important to note that the $E_{\mathrm{T}}^{\mathrm{miss}}$ used in the search for supersymmetry described in this dissertation does not include hadronically decaying τ-leptons, and instead treats these objects as jets.

Chapter 6

Jet Calibration

6.1 Jet Calibration Procedure

The ATLAS calibration scheme used for calorimeter jets can be seen in Figure 6.1. There are four basic steps to obtain calorimeter jets ready for physics analysis.

1. The jets are first treated for the effects of pile-up on the energy measurement. Pile-up is defined as the contribution to a given event that does not originate from the primary interaction. Tracks and energy deposits from pile-up can be counted as being a part of the jet, when in fact it is not. Pile-up is classified as in-time, meaning tracks and energy deposits originating from other reconstructed primary vertices in the event (N_{PV}), or it is out-of-time, which is the contribution from past collisions to the current event. The corrections due to pile-up are derived using simulated events as a function of N_{PV}, the average number of interactions (μ, which is representative of out-of-time pile-up) and in bins of η and p_{T} to account for detector effects and the properties of the jet [29, 30].

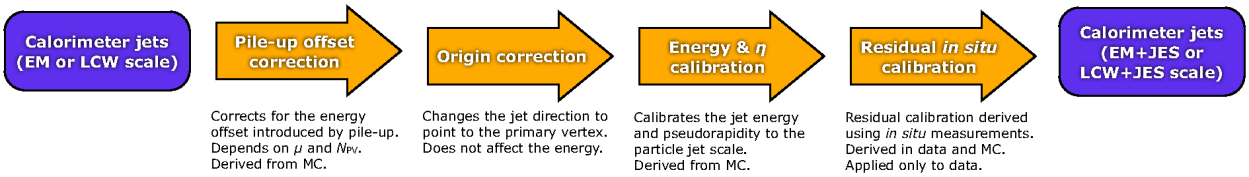

Figure 6.1: An overview of the ATLAS jet calibration scheme beginning with the calorimeter jets at EM-scale or LCW-scale and ending with the full jet energy scale calibration (EM+JES or LCW+JES).

2. The original construction of the jet has the jet oriented such that the direction points back to the center of the detector. A correction is applied that adjusts the jet such that it points to the primary vertex [29].

3. The jet energy scale (JES) correction is an overall correction to the jet's energy based on the η and p_{T} of the jet [29]. This correction is derived in Monte Carlo for isolated jets by comparing the jet's reconstructed energy to that of the truth jet from simulation, where truth jet represents the calorimeter response to the quark undergoing hadronization [29]. It is designed to bring the calorimeter jet as close to the truth jet as possible. Jets beyond this calibration stage are denoted as EM+JES or LCW+JES depending on the initial energy calibration. The EM scale and LCW scale are described in Section 5.4.

4. A residual correction derived *in-situ* is applied as the final step. This correction is derived in a variety of event topologies by comparing the response ($R = p_{\mathrm{T}}^{jet}/p_{\mathrm{T}}^{reference}$) in data with simulation [29, 31].

6.2 γ + Jet Analysis

This section describes the *in-situ* calibration of hadronic jets using events with photons and jets [29, 31]. The method utilizes a simple balancing procedure in order to derive a residual correction to the jet's energy. This is the final step in the calibration procedure, as laid out in Section 6.1 and shown pictorially in Figure 6.1.

The method is aptly named direct p_{T} balance (sometimes referred to as simply 'direct balance'), where it exploits the conservation of momentum in the transverse plane. In QCD hard scatter events a photon can be emitted along with a recoil jet. The p_{T} should be balanced between the well-measured photon and the jet. In these events a response ratio is constructed,

$$R = \frac{p_{\mathrm{T}}^{jet}}{p_{\mathrm{T}}^{\gamma}} \tag{6.1}$$

whereby one can compare this response in data and simulation for a range of photon p_{T}. Under the assumption that the differences between the photon energy in data and simulation is negligible, one can derive a correction factor to be applied to jets in data that is the ratio of these responses. The aim of this procedure is to correct any residual differences between simulation, which contains the calibrated parton response in the calorimeter, and data.

The selection criteria outlined in Subsection 6.2.1 insures that the event topology contains well measured photons and jets that are back-to-back. Subsection 6.2.2 presents the direct balance results, and Subsection 6.2.3 presents the dominant systematic uncertainty considered. The final subsection (6.2.4) will review some of the more recent developments that will be included in the final *in-situ* results for the dataset recorded in 2012.

6.2.1 Event Selection

The event selection closely follows that described in Ref. [32], with some slight modifications to account for the changes in data taking conditions. The event selection criteria can be found in the following detailed list.

1. Events are required to have a primary vertex with at least five associated tracks. The primary vertex assigned to the hard scattering collision is the one with the highest

$\sum(p_{\mathrm{T}}^{track})^2$, where the scalar sum is taken over all tracks associated to the vertex.

2. There must be at least one reconstructed photon with $p_{\mathrm{T}} > 25$ GeV. The leading photon is taken as the one from the hard process. This threshold is set by the lowest trigger available.

3. The leading photon is required to trigger the event, and a single photon trigger is used with varying p_{T} thresholds depending on the photon p_{T}. The thresholds and offline triggers are given in Table 6.1. Due to the high production rate for low p_{T} photons, the triggers with lower p_{T} thresholds are further filtered in data. To account for these "prescales" in simulated events, the event weight is augmented to include the appropriate luminosity recorded by that trigger.

4. The photon is required to be 'tight', which implies that the pattern of energy deposition in the calorimeter is consistent with the expected showering of a photon.

5. The leading photon must have $|\eta| < 1.37$, keeping it in the barrel region of the calorimeter, further insuring that it is well measured.

6. It is possible that jets may be misidentified as photons. In order to reduce the effect of this background, the leading photon is required to be isolated from other calorimeter activity. The isolation variable (E_T^{cone}) is computed in a cone of $R = 0.4$ around the photon and corrected for pile-up energy inside the isolation cone. This analysis requires that the leading photon have $E_T^{cone} < 3$ GeV.

7. Only jets with $p_{\mathrm{T}} > 12$ GeV are considered to reject fake jets from noise bursts in the calorimeters or from non-collision background.

8. The highest p_{T} jet must be in the region $|\eta| < 0.8$.

9. Two requirements are placed to suppress the effects of soft radiation that would affect the balancing between the photon and leading jet. The first is that the leading photon

and jet are required to be back-to-back in the ϕ-coordinate system by requiring $|\phi^{jet} - \phi^{\gamma}| > 2.9$ radians. The second requirement is to remove events that have a subleading jet that is more than 20% of the leading photon p_{T}. The subleading jet is defined as the next highest p_{T} jet with jet vertex fraction (JVF) larger than 0.5 or less than zero for events which JVF could not be computed due to the jet being outside the tracking coverage region.

p_{T} Range [GeV]	Trigger
$25 < p_{\mathrm{T}}^{\gamma} < 45$	EF_g20_loose
$45 < p_{\mathrm{T}}^{\gamma} < 65$	EF_g40_loose
$65 < p_{\mathrm{T}}^{\gamma} < 85$	EF_g60_loose
$85 < p_{\mathrm{T}}^{\gamma} < 105$	EF_g80_loose
$105 < p_{\mathrm{T}}^{\gamma} < 125$	EF_g100_loose
$125 < p_{\mathrm{T}}^{\gamma}$	EF_g120_loose

Table 6.1: Definitions for the trigger regions. The left column gives the p_{T} of the photon and the right column gives the corresponding trigger applied.

6.2.2 Energy Measurement

The jet response is measured in bins of photon transverse momentum and then fitted with a truncated poisson distribution. The poisson is truncated to deal with the lower p_{T} thresholds outlined in the event selection found in Section 6.2.1.

Distributions for the jet responses for $25 < p_{\mathrm{T}}^{\gamma} < 45$ GeV and $110 < p_{\mathrm{T}}^{\gamma} < 160$ GeV can be found in Figure 6.2 for data and simulation. The mean values from the fits define the response for that particular bin. This is done for many p_{T}^{γ} bins and combined to form Figure 6.3, which represents the result of fitting each p_{T}^{γ} bin for data and simulation and plotting the mean. The ratio of the fitted responses is the *in-situ* correction to be applied to data. Examing Figure 6.3 more closely, one can see that the correction is 1% for $p_{\mathrm{T}}^{\gamma} > 110$ GeV, but increases for $p_{\mathrm{T}}^{\gamma} < 110$ GeV. This is due to the contamination from jets that are identified as photons, which happens at a much larger rate for lower p_{T}.

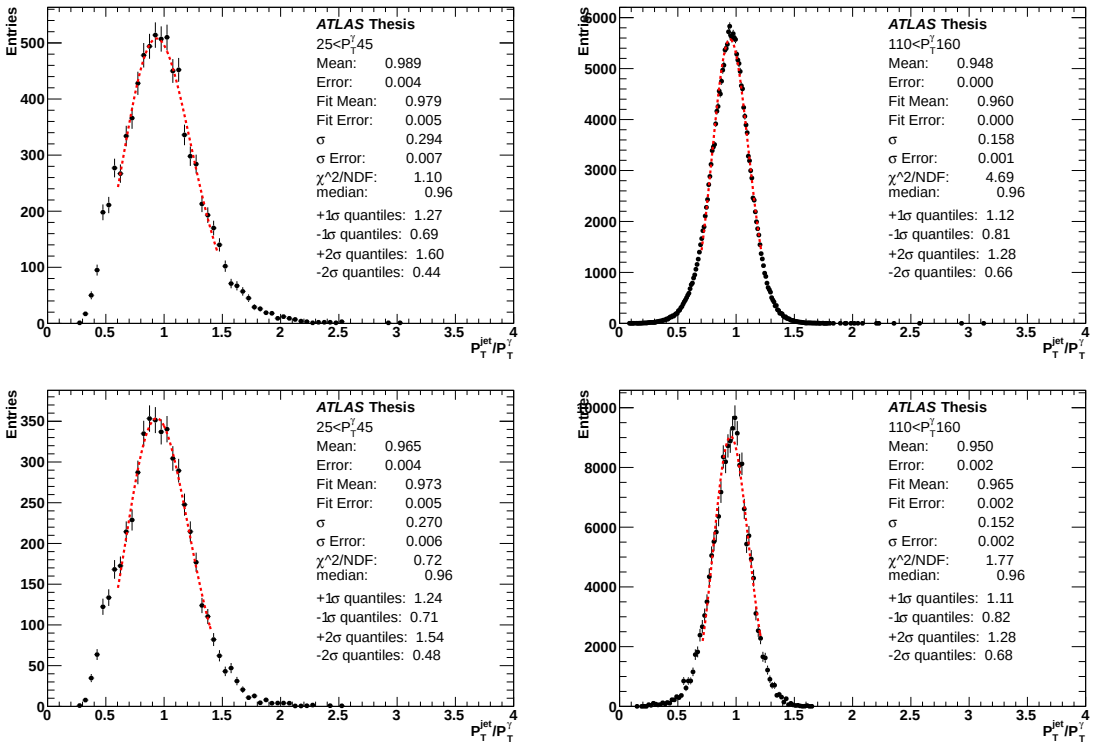

Figure 6.2: Example responses from two specific photon p_{T} bins for data (top) and γ+jet MC (bottom). The jets used have a cone size of $R = 0.4$ and are calibrated at the EM+JES scale. The difference in the width of the responses for the two p_{T} bins is representative of the energy resolution for the jets. The energy resolution for jets increases as the jets energy increases.

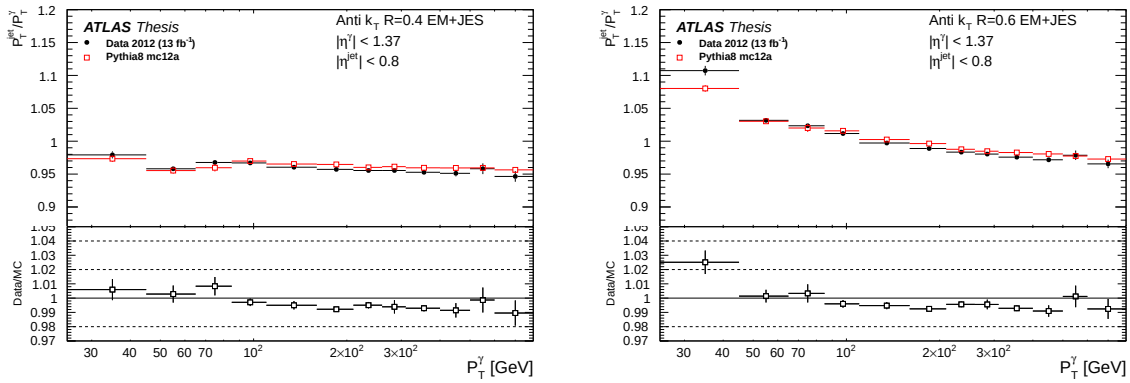

(a)$R = 0.4$,EM+JES

(b)$R = 0.6$,EM+JES

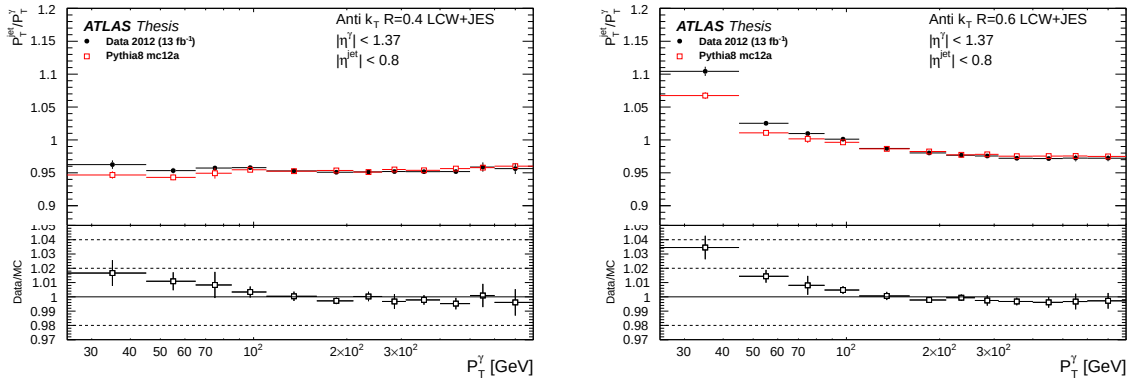

(c)$R = 0.4$,LCW+JES

(d)$R = 0.6$,LCW+JES

Figure 6.3: Average jet response for anti-k_T jets with distance parameter at 0.4 (left) and 0.6 (right) for EM+JES (top) and LCW+JES (bottom). The data-to-MC response ratio is given at the bottom of each figure. Only the statistical uncertainties are shown.

6.2.3 Systematics

Several sources of systematic uncertainties are associated with the direct balance method. These uncertainties are associated with the event selection, the calibration of the reference object, and the properties of the jet being balanced. The uncertainties are propagated through the response ($p_{\mathrm{T}}^{jet}/p_{\mathrm{T}}^{\gamma}$) to the data-to-MC ratio. The next subsections describe the procedure to measure the dominant systematics.

Soft radiation suppression Two selection criteria outlined in Subsection 6.2.1 are responsible for reducing the contribution from soft radiation, which can impact the stability of the data-to-MC response ratio. The first is the cut on the subleading jet's p_{T}. The nominal requirement is p_{T}^{jet2} <max$(12, 0.2 \times p_{\mathrm{T}}^{\gamma})$, and the systematic is evaluated by shifting the cut value ± 0.1. The average change in the response from these shifts is of the order 0.5%.

The second criteria is requirement on $\Delta\phi$(jet,photon)> 2.9 radians, which is shifted by ± 0.1 to allow for additional soft radiation to contribute to the response. This is again propagated through to the data-to-MC response ratio, and the contribution is found to be of the order 0.5%.

Similar studies were performed by loosening and tightening the requirements on these two criteria simultaneously. The results were compatible with the independent shifts.

Contamination Contamination from a jet that fakes a photon is the major source of uncertainty in the direct balance method. This effect is most noticeable for photons with $p_{\mathrm{T}} < 110$ GeV, where the data-to-MC ratio rises, which is attributed to the increase in the response.

To first order, the uncertainty is estimated as $(1-P) \times (R_{dijet} - R_{\gamma+jet})/R_{\gamma+jet}$, where P is the

purity and R_{dijet} and $R_{\gamma+jet}$ is the response from dijet events and $\gamma + jet$ events respectively. The purity is estimated using a data driven, sideband technique which is described in Refs. [25, 33]. The purity is about 70% at $p_{\mathrm{T}}^{\gamma} = 55$ GeV and steadily increases to 93% for higher values of p_{T}^{γ}. The difference in the response is estimated from MC, and the relative response differences are found to be below 5% across the p_{T} range [32]. A conservative, flat 5% is chosen.

Photon Energy Scale The photon energy is calibrated by extrapolating from the electron energy calibration, which is done *in-situ* using Z boson decays to $e^{\pm}e^{\mp}$ [34]. The systematic uncertainties are broken into three categories: Z scale uncertainty, pre-sampler scale uncertainty, and the material uncertainty. These errors are all propagated through to the data-to-MC ratio and are found to be of the order $\pm 0.5\%$ for all photon p_{T} bins.

Choice of Generator Two generators were made available for this analysis, `PYTHIA` [35] and `HERWIG` [36]. Their intrinsic differences in the modeling of the parton shower, jet fragmentation and multiple parton interactions can lead to differences in the p_{T} balance, and therefore differences on the data-to-MC ratio. `PYTHIA` is chosen as the nominal generator and `HERWIG` is used to assess the systematic. The differences are found to be as large as 1.4% at low photon p_{T} which becomes negligible at higher values of photon p_{T}.

Out-of-cone Correction Even in events where the photon's transverse momentum is equal to that of the truth, particle-level jet originating from the parton, the response for the reconstructed jet is not unity [32]. This is due to two primary factors:

1. The photon does balance the the entire system of recoiling particles, but it may not balance the jet since the jet is a subset of that system due to the limited size of the jet cone.

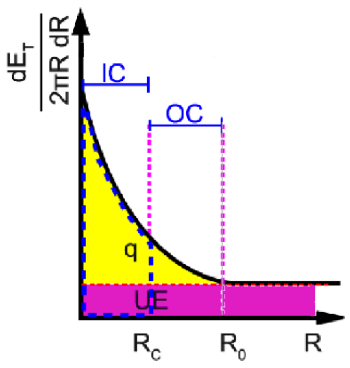

Figure 6.4: A schematic representation of the average scalar track p_{T} sum distribution centered around the jet axis. IC stands for in-cone and OC stands for out-of-cone. The yellow shaded region represents the contribution from the quark. The pink shaded region represents that of the underlying event. The area encompassed by the dashed blue line is what contributes to the jet.

2. There are contributions to the jet that are not associated with the hard scatter, for example contributions from pile-up and the underlying event. Any discrepancy between data and simulation for the migration of energy in and out of the jet cone needs to be taken into account.

A factor relating the p_{T} of the photon to that of the truth jet is estimated by computing the average scalar track p_{T} sum distribution around the jet axis. This factor is defined as,

$$k - term = \frac{p_T^{IC,ALL}}{p_T^{IC+OC,ALL} - p_T^{IC+OC,UE}} \tag{6.2}$$

where $p_T^{IC,ALL}$ is the average p_{T} sum of all the tracks inside the jet cone with radius R, $p_T^{IC+OC,ALL}$ is the average scalar p_{T} sum of all tracks inside a concentric cone with radius $R_0 \geq R$, where R_0 is the radius at which the average p_{T} sum distribution becomes approximately constant, and $p_T^{IC+OC,UE}$ is an estimation of the contribution from the underlying event [32]. An illustration of the components can be found in Figure 6.4.

Extracting the necessary quantities needed to calculate the out-of-cone correction is relatively simple. Both $p_T^{IC,ALL}$ and $p_T^{IC+OC,ALL}$ are determined directly from the distribution,

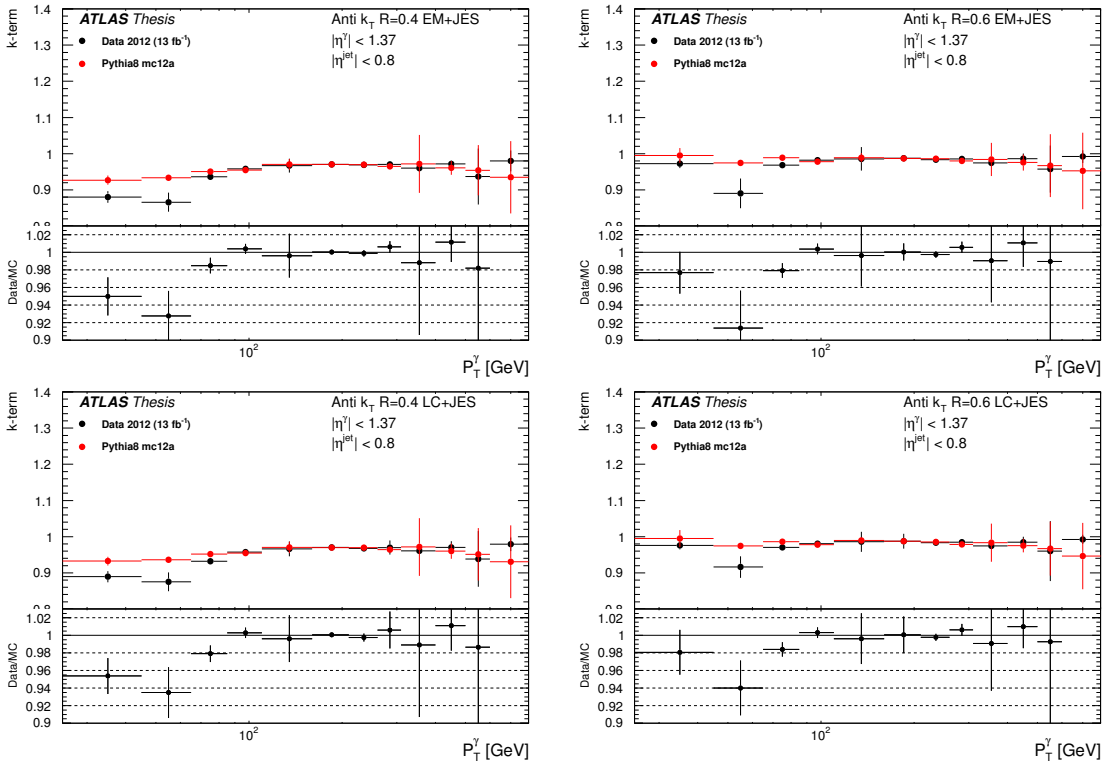

Figure 6.5: The factor measuring the migration of energy out of the jet cone for cone sizes of 0.4 (left) and 0.6 (right) for EM-scale (top) and LCW-scale (bottom). The data-to-MC ratio is shown in bottom of the figure. The statistical and systematic uncertainties are added in quadrature and incorporated into the error bars.

numerically integrating out to R_0. The final component, $p_T^{IC+OC,UE}$, is obtained by fitting the average transverse momentum distribution with the following function,

$$f(\Delta R) = \frac{a}{\Delta R^b + c} + d, \tag{6.3}$$

where a, b, c, and d are fit parameters that are allowed to float. The 'd' parameter is a measure of the underlying event both in-cone and out-of-cone.

The results for the out-of-cone correction are shown for data and simulation in Figure 6.5. The end goal is to apply this as a correction, however at the time this analysis completed the difference between data and MC is taken as a systematic error.

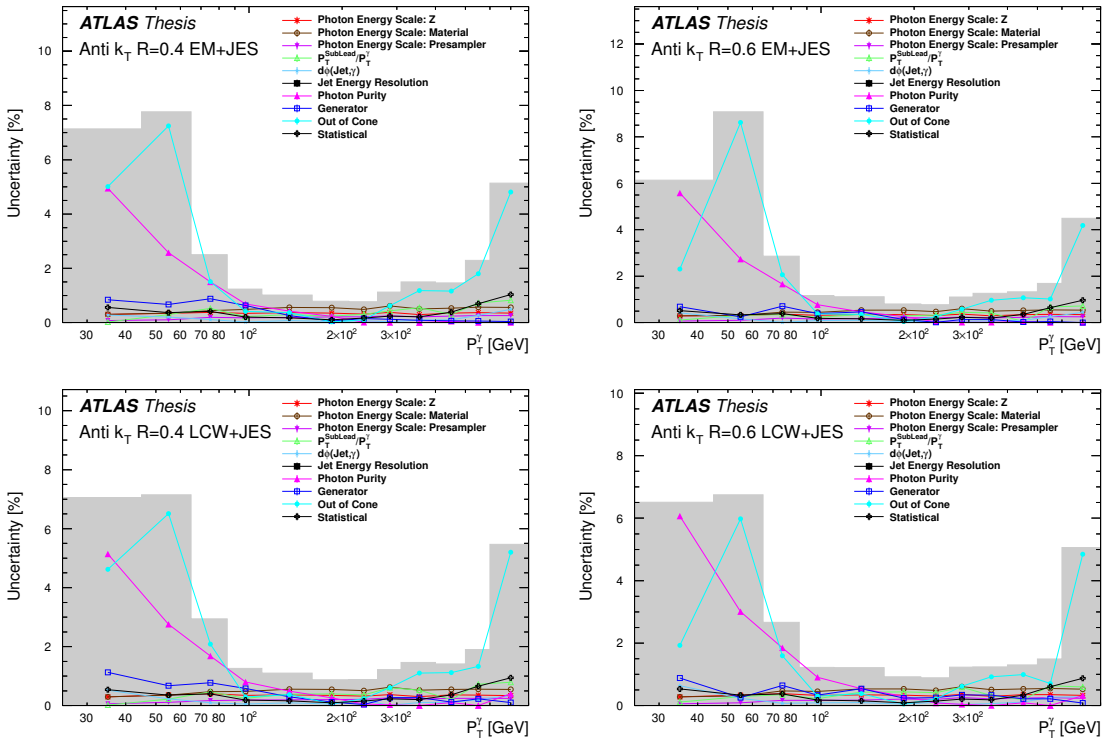

Figure 6.6: The summary of the systematic uncertainties considered for this method for both EM+JES (top) and LCW+JES (bottom) for cone sizes $R = 0.4$ (left) and $R = 0.6$ (right). These figures represent the maximum deviations with respect to the nominal. The gray shaded region is the total systematic uncertainty taking into account correlations. For the statistical combination with the Z+jet and multi-jet results, the sign and the statistical error on the systematic uncertainty is taken into account.

Summary The systematic uncertainties outlined in this section are summarized in Figure 6.6. The real power of this method is that it reduces the overall jet energy scale uncertainty to a few percent. The results of this analysis are combined with the Z+jet analysis and the multi-jet analysis [31], which dominate in the low p_{T} regime and extreme p_{T} regime respectively. This is in part due to contamination at low p_{T} ($p_{\mathrm{T}}^{\gamma} < 110$ GeV), which resulted in further studies that will be presented in Subsection 6.2.4.

6.2.4 Future Studies

Several improvements have been made to this analysis since the last distribution for the Moriond 2013 conference, including an updated treatment of the systematic uncertainties to take into account the statistical uncertainty on the systematic uncertainty, and an updated isolation criteria to improve the results at lower photon p_{T}. The first is still in its infancy, while the second is in place and will be discussed here in some detail.

As seen in Figure 6.3, the lower p_{T} bins are where the data-to-MC ratio suffers the most due to contamination from dijet events. The purity in this region could be improved by tightening up the requirements on the photon. This is done by requiring the photon to satisfy a tighter isolation requirement. Following Figure 6.7 a p_{T}-dependent isolation has been developed, which is outlined in Table 6.2. Applying this p_{T}-dependent isolation increases the purity at low p_{T} from 70% to $> 80\%$, which leads to a more stable data-to-MC ratio as seen in Figure 6.8. This improvement will be folded into the final *in-situ* result for the 2012 dataset.

p_{T} Range [GeV]	Isolation Requirement
$25 < p_{\mathrm{T}}^{\gamma} < 45$	$E_T^{cone} < 0.5$
$45 < p_{\mathrm{T}}^{\gamma} < 65$	$E_T^{cone} < 1.0$
$65 < p_{\mathrm{T}}^{\gamma} < 85$	$E_T^{cone} < 2.0$
$85 < p_{\mathrm{T}}^{\gamma}$	$E_T^{cone} < 3.0$

Table 6.2: Definitions for the isolation regions. The left column gives the p_{T} of the photon and the right column gives the corresponding isolation requirements.

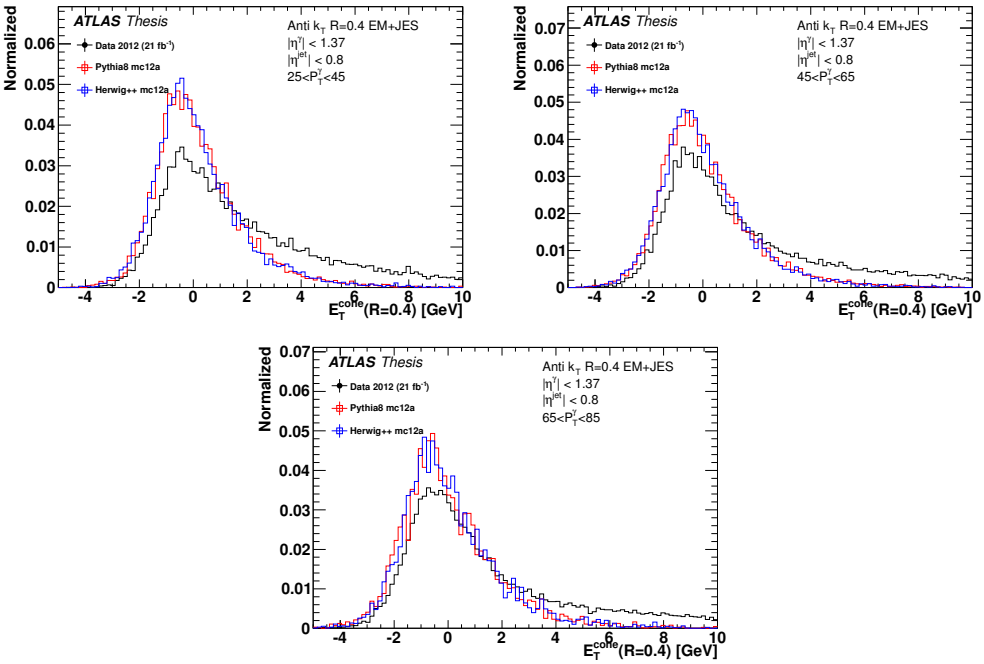

Figure 6.7: The normalized distribution for the photon isolation variable for data and the two simulated samples for the full event selection applied. The tails extending to higher values in data are indicative of the jet like nature of these mis-identified photons. Placing a tighter cut on this variable leads to a more pure photon sample.

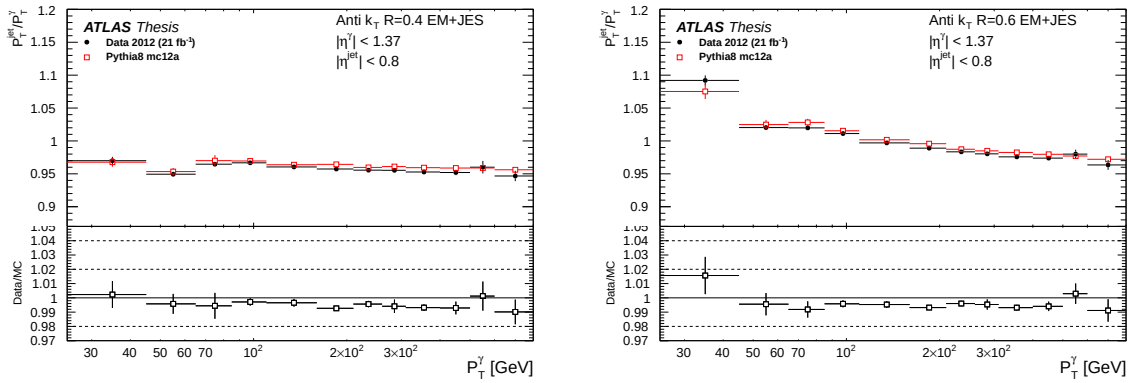

(a)$R = 0.4$,EM+JES (b)$R = 0.6$,EM+JES

(c)$R = 0.4$,LCW+JES (d)$R = 0.6$,LCW+JES

Figure 6.8: Average jet response for anti-k_T jets with distance parameter at 0.4 (left) and 0.6 (right) for EM+JES (top) and LCW+JES (bottom). These results contain the updated isolation outlined in Table 6.2. The data-to-MC response ratio is given at the bottom of each figure. Only the statistical uncertainties are shown.

Chapter 7

Search for Heavy Neutrinos

7.1 Interpretations

Two independent, but complimentary, approaches are used to search for the possible existence of a heavy neutrino-like particle. The first is a generic approach using a parameterized effective Lagrangian [37]. The primary assumption is that the intermediate particle responsible for the production of the hypothetical neutrino is beyond the reach of the LHC beam energy, however it is assumed to couple to the LHC initial state. The hypothetical neutrino is assumed to be accessible at the LHC energies and the mass of this particle can be reconstructed using the final state objects. If an observation were to be made, constraints on the coefficients used in the parameterized Lagrangian could be used to constrain the properties of the propagator [37].

The second approach is model specific and involves the introduction of a new chiral symmetry. The left-right symmetric model [38] proposes the existence of a new, right-handed W (W_R) boson to mediate the new, heavy neutrino production. Both the mass of the new, heavy neutrino and the W_R can be reconstructed in this approach. If an excess of events were to be

found consistent with the left-right symmetric model, it would indicate that the SM would only need to be augmented in a minor way by adding an additional SU(2) group to account for the observed small neutrino masses.

The introduction of the right-handed W boson is the primary difference between the two approaches used in this dissertation, as it presents an additional observable in the final state (m_{W_R}). For this reason, even though the approaches share the same final state of two leptons and two hadronic jets, they utilize different variables to guide the search. The left-right symmetric model, described in Subsection 7.1.2, will utilize all final state objects to reconstruct the mass of a proposed new boson, while the effective operator approach, described in Subsection 7.1.1, will use a subset of the final state objects to reconstruct the mass of the proposed heavy neutrino. Both approaches probe the possibility that the heavy neutrino is a Dirac fermion or a Majorana fermion. Majorana fermions are, by definition, their own anti-particles. If the neutrino were to be a Majorana fermion, the final state would contain a striking same-sign dilepton signature, for which the SM background is small. If the neutrino is Dirac, only the opposite-sign dilepton channel is accessible given that Dirac neutrinos would not be able to violate lepton number and produce a same-sign signature.

7.1.1 Effective Operator Approach

A general approach to studying collider signatures involving a new, heavy neutrino is explored in the context of a Lagrangian of effective operators (HNEO). The primary assumption made is that the propagator responsible for the production of the heavy neutrino is beyond the reach of the LHC beam energy, and can therefore be integrated out of the Lagrangian. This allows one to parameterize the hypothetical neutrino interactions using effective operators

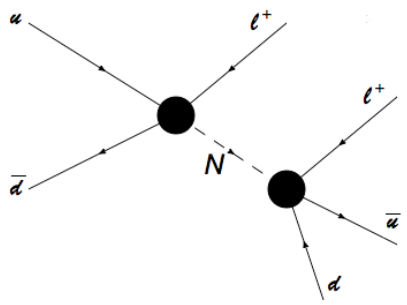

Figure 7.1: Feynman diagram for the effective operator approach for heavy neutrino production and decay.

$\mathcal{O}_i$ to construct a Lagrangian that can be added onto the SM Lagrangian,

$$\mathcal{L} = \mathcal{L}_{SM} + \sum_{n=5}^{\infty} \frac{1}{\Lambda^{n-4}} \sum_i \alpha_i \mathcal{O}_i^{(n)}, \tag{7.1}$$

where Λ is the scale of new physics, n is the mass dimension, α is the coupling strength, and $\mathcal{O}$ is the operator [37]. The production cross section is suppressed by the dimension of the operator, and therefore for this search the lowest possible dimension is chosen with the constraint that it couples to the initial state at the LHC. This analysis probes four-fermion interactions (which have mass dimension $n = 6$) as shown in Figure 7.1 using one vector operator (V) and three scalar operators ($s1$, $s2$, and $s3$), which corresponds to the processes having large enough cross sections in order for this analysis to be sensitive [37]. The corresponding interactions related to each operator can be seen in Table 7.1. The event topology is the same for all three operators, but the underlying physics between the operators varies, which leads to differences in the kinematics of the decay products as well as different cross sections.

The neutrino produced can either be Dirac or Majorana, which will impact the sign of the leptons in the final state. If the neutrino is Dirac, the final state will only include opposite-sign leptons, given that Dirac neutrinos cannot violate lepton number. If it is Majorana, the decay of the heavy neutrino will lead to equal amounts of same-sign and opposite-sign

Operator	Interaction
V	$duNe$
$s1$	$QuNL$
$s2$	$LNQD$
$s1$	$QNLd$

Table 7.1: Summary table of the operators considered and their corresponding four-fermion interactions. The right-handed $SU(2)$ singlets are represented by e, u, and d, while the left-handed $SU(2)$ doublets are represented by Q and L.

dilepton pairs in the final state. The cross sections for both cases are related to the energy scale of new physics and the strength of the coupling constant $\sigma \approx \alpha^2/\Lambda^4$. In each scenario, the mass of the heavy neutrino can be reconstructed from one lepton and up to two hadronic jets. In the absence of observing a heavy neutrino signal, bounds will be set on the coupling constant and the new physics scale.

7.1.2 Left-Right Symmetric Model

The Left-Right Symmetric Model (LRSM) is a grand unified theory (GUT) inspired extension of the SM Lagrangian to treat equally the right-handed and left-handed chiral fields. The gauge symmetry is represented by $SU(3)_C \times SU(2)_L \times SU(2)_R \times U(1)_{B-L}$, where the inclusion of the right-handed fields is explicit as well as the introduction of a new conserved quantity, $B - L$ (the difference between baryon (B) and lepton (L) quantum numbers) [38].

The LRSM includes an attractive mechanism for generating the observed light neutrino masses by introducing a family of new, heavy right-handed neutrinos, right-handed gauge bosons, and doubly charged Higgs bosons [39, 40]. This hypothetical boson could be produced at the LHC through a $q\bar{q}$ interaction as shown in Figure 7.2. This interaction would produce a charged lepton and a heavy neutrino, which would then decay to yield a final state with two leptons and two jets. The final state particles, two leptons and up to two jets, can be used to reconstruct the mass of the W_R. The reconstructed W_R mass will be the search

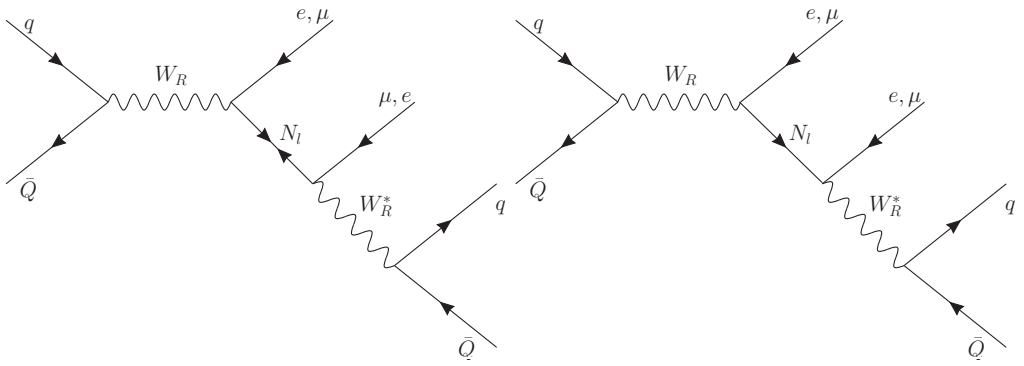

Figure 7.2: Feynman diagram for Left-Right Symmetric Model production and decay of right-handed W boson and heavy neutrino in the mixing (left) and no mixing (right) cases.

variable utilized in this analysis. The heavy neutrino mass can also be reconstructed from one lepton and up to two jets, however this adds further complexity as one has to choose the appropriate lepton from the dilepton final state.

7.2 Selection

7.2.1 Event Selection

Events selected for this analysis are required to satisfy a set of quality criteria unique to the data taking period in 2011. Additionally the primary vertex in the event is required to have at least 5 associated tracks originating from it. If additional vertices are reconstructed, the one having the highest $\Sigma(p_T^{track})^2$ is chosen.

The events are required to have at least two leptons with $p_{\mathrm{T}} > 25$ GeV to meet the offline trigger thresholds. In addition, the leptons are required to have associated tracks that are matched to the primary vertex. There must also be at least one jet with $p_{\mathrm{T}} > 20$ GeV, instead of two as indicated by the final state for LRSM and HNEO. If the hypothetical neutrino is light then it will be boosted and the decay products can be close together. If this happens, the detector cannot resolve two independent jets and puts them together as one. In order

to reduce the background from Drell-Yan production and mis-identified leptons, events are required to have dilepton mass larger than 110 GeV for both same-sign and opposite-sign as well as for all flavor combinations.

Electron Electrons are required to satisfy the "medium" identification criteria [41] with $p_{\mathrm{T}} > 25$ GeV and $|\eta| < 2.47$. The transition region in the electromagnetic calorimeter is excluded ($1.37 < |\eta| < 1.52$) due to the poor electron energy resolution. Electrons are also required to not share an inner detector track with a reconstructed muon to reduce the effect of mis-identified electrons. The electrons used in this analysis were required to satisfy a calorimeter isolation by requiring the topological cluster energy in a cone of $R = 0.2$ around the electron to be less than 15% of the electrons transverse energy, which will reduce the probability that a hadronic jet is identified as an electron.

Muon Muons are required to be identified in the inner detector (ID) and the muon spectrometer (MS), and must have at least one hit in the pixel detector, five in the SCT, and an $|\eta|$-dependent hit requirement in the TRT. Only muons with $p_{\mathrm{T}} > 25$ GeV and $|\eta| < 2.4$ are considered in this analysis. Requirements on the longitudinal (z_0) and transverse (d_0) impact parameters are summarized in Table 7.2, and are used to discriminate prompt muons and muons from the decays of b-quarks.

The dimuon channel was the most powerful channel used in this search, and for this reason a detailed study of the muon isolation was performed in order to extract the most sensitivity from the same-sign region. The track and calorimeter isolation requirements are:

- If $p_{\mathrm{T}} < 80$ GeV, require the sum of the p_{T} of the tracks in a cone of $R = 0.3$ around the muon to be less than 1 GeV.
- If there is a jet in the event with $\Delta R = \sqrt{\Delta\eta^2 + \Delta\phi^2} < 0.4$ require the muon to have

$p_{\mathrm{T}} > 80$ GeV and (Etcone30/p_{T}- 3)/$p_{\mathrm{T}} >$ -0.02 GeV^{-1}, where Etcone30 is the sum of the calorimeter energy in a cone of $R = 0.3$ around the muon.

- If there is no jet in the event with $\Delta R < 0.4$, require the calorimeter energy in a cone of $R = 0.3$ around the muon to be less than 15% of the muon p_{T}.

These requirements are designed to recover signal acceptance in LRSM where the mass of the neutrino is close to the mass of the right-handed W boson. In this situation, the heavy neutrino is boosted which causes the lepton from this decay to be closer to the jets also produced in the decay, making them less isolated. This modified isolation recovered up to 40% of the dimuon signal events where this issue was present, and enhances the rejection power of mis-identified prompt muons.

Impact Parameter	Requirement
$\lvert z_0 \rvert$	< 5 mm
$\lvert d_0 \rvert$	< 0.2 mm
$\lvert d_0/\sigma_{d_0} \rvert$	< 5

Table 7.2: Details of the muon impact parameter requirements.

Jet The jets used for this analysis are calibrated at the EM+JES scale and are required to have $p_{\mathrm{T}} > 20$ GeV. The jets used must satisfy $|\eta| < 2.8$. Pile-up jets are rejected by requiring |JVF| > 0.75. Additionally, the closest jet to each electron within $\Delta R(e, jet) < 0.5$ is removed in order to avoid the double counting of physics objects.

7.2.2 Triggers

This analysis employs the use of single lepton triggers, where only one of the two leptons in the event are required to match to the trigger. During the data taking period used in this analysis the trigger menu was updated in order to deal with the increased rate of collisions.

Electrons were required to have an offline p_{T} of at least 20 GeV, satisfy several shower-shape requirements and match an ID track. For the final 0.5 fb^{-1} the threshold was increased to 22 GeV. Muons were required to have an offline p_{T} of at least 18 GeV and $|\eta| < 2.4$ in order to match to the trigger. For this analysis, only leptons with $p_{\mathrm{T}} > 25$ GeV are used, and the typical efficiencies for the electron trigger for offline analysis are $99 \pm 1\%$ and 74% (91%) for muons in the barrel (end-cap) regions with an uncertainty of about $\pm 1\%$.

7.3 Standard Model Backgrounds

Several background sources contain events with two leptons and at least one jet. These processes are estimated from simulation and fully and semi-data driven techniques. Table 7.3 lists the dominant backgrounds in the opposite-sign and same-sign channels and how they are estimated.

Process	Opposite-sign	Same-sign
Z+jet	MC Validated	Charge-flip
Top	MC Validated	Charge-flip
Diboson	Simulation	Simulation + Charge-flip
Fake Leptons	Matrix Method	Matrix Method

Table 7.3: Summary of the four dominant background categories and the technique used to estimate the contribution to the signal region.

The simulated samples used in this analysis are found in Subsection 7.3.1 and the systematic uncertainties associated with the simulated samples can be found in Subsection 7.3.2. For dominant backgrounds in the opposite-sign channel ($t\bar{t}$ and Z+jets), dedicated data control regions are designed to validate the simulated prediction, which is described in Subsection 7.3.3. The charge-flip background contributes in the same-sign ee and $e\mu$ channel and cannot be estimated from simulation. The method used to estimate this background can be found in Subsection 7.3.4. The dominant background in the same-sign channels are

from fake leptons and are described in Subsection 7.3.5.

7.3.1 Monte Carlo Samples

Fully simulated MC event samples enter into the background estimation as either the central value used in the analysis or serve as a cross-check against a data-driven estimate. Many SM processes contribute to dilepton searches and for this reason great care has gone into choosing which generator and showering software are used for each sample.

Top Processes involving the top quark have numerous ways of contributing to the signal region. $t\bar{t}$ production is simulated using `MC@NLO` [42, 43, 44] with the next-to-leading order (NLO) parton distribution function (PDF) `CTEQ6.6` [45]. Fragmentation and hadronization is handled by `HERWIG` [46]. Single top quark production via s- and t-channel processes are generated with `MC@NLO`. The associated production of $t\bar{t}$ with a vector boson (W,Z, or γ) is simulated with `Madgraph` [47] interfaced with `PYTHIA` [35].

V+jet The production of Z/γ^*+jets is generated with `ALPGEN` [48] with leading order PDF `CTEQ6L1` [45] Production of W+jet, $Wb\bar{b}$, and $Wc\bar{c}$ are generated using `ALPGEN` as well. These samples are only used for studies involving leptons from non-isolated sources and are not used to derive a background estimate for the signal region.

Diboson Diboson (WW,WZ, and ZZ) processes are generated using `HERWIG`. Diboson samples involving a photon ($W\gamma$ and $Z\gamma$) are generated using `Madgraph` interfaced with `PYTHIA`.

QCD The QCD estimate is taken from a data-driven technique, however comparison with MC is sometimes necessary to validate the method. Samples containing $b\bar{b}$ events are generated with `PYTHIA` including an event filter to select events with at least one lepton.

7.3.2 Monte Carlo Systematic Uncertainties

The simulated samples have several sources of systematic uncertainty to account for energy calibration differences between data and simulation as well as uncertainty associated with lepton identification. The largest uncertainty is from the jet energy scale (2-6%) and resolution (5-12%), which are applied to each jet and are p_{T} and η dependent [25]. An additional 2-7% is included on top of the JES uncertainty to account for the effects of pile up.

The lepton p_{T} scale and resolution have an associated uncertainty that is dependent on the lepton kinematics. The scale varies from 0.2-2%, while the resolution is larger at 0.4-10% [34, 49, 50]. The uncertainty in correctly identifying a lepton is also taken into account and ranges from 0.2-3.3% [34, 49, 50].

In addition to the uncertainty on the physics objects, there is an uncertainty associated with the modeling of the simulated physics processes. Theoretical uncertainty on the diboson cross section ranges from 5-7% [51]. For $t\bar{t}$, there are six associated uncertainties that are summed in quadrature:

1. To estimate an uncertainty on the top quark mass, three separate masses are used as input for the MC simulation: 170, 172.5, and 175 GeV, where 172.5 GeV is used in the simulation of the nominal sample. The number of events in the signal regions is then counted for each input mass, and the relative difference with the nominal value is taken as a systematic uncertainty.

2. The uncertainty on the theoretical cross section and the PDF used [52].

3. The uncertainty on the choice of MC generator is evaluated by comparing the prediction from the nominal `MC@NLO` to that of `POWHEG`.

4. The uncertainty on the showering algorithm used is estimated by comparing the nominal `HERWIG` to `PYTHIA`.

5. An uncertainty associated with the initial state and final state radiation is evaluated by varying the PDF uncertainty up and down.

6. An uncertainty associated with the statistics on the nominal sample is included.

Each uncertainty is combined in quadrature and the final result is a 15% uncertainty. In the case of single top production with a W boson, the theoretical uncertainty on the cross section is estimated to be 10% [52]. For $t\bar{t}$ production with an associated vector boson(s), an uncertainty of 50% on the theoretical cross section is included [53].

The signal samples also contain an uncertainty based on the limited knowledge of the PDFs and α_s. The uncertainty is evaluated using a range of current PDF sets, as described in Ref. [54], and taking the maximum overall uncertainty. The resulting uncertainty was found to be 9% and 12% for LRSM and HNEO signal samples respectively.

7.3.3 Monte Carlo Validation

The dominant backgrounds in the same-sign channel are from fake leptons, which is extracted in a fully data driven way and detailed in Subsection 7.3.5. In the opposite-sign channel, the dominant backgrounds are contributed from Z+jets and $t\bar{t}$. Two dedicated control regions are designed to select events from these two processes in data in order to validate the MC prediction.

Z+jets The contribution from Z+jets is estimated from MC and corrected by a jet dependent scale factor that is measured in a data control region. The control region requires that the invariant mass of the lepton pair (both opposite-sign and same-sign are considered) be in the range of 80-100 GeV. The number of observed $Z \to \ell\ell$ events is determined by subtracting the additional SM backgrounds. The ratio between data and MC Z+jets events is then taken in order to obtain a scale factor (sf) which is defined as,

$$sf = \frac{N_{data} - N_{non-Z}}{N_{Z,MC}} \tag{7.2}$$

where N_{data} is the observed events in the control region, N_{non-Z} is the contribution of non-Z sources to the control region, and $N_{Z,MC}$ is the contribution from Z+jet MC samples. The resulting scale factors are parameterized as a function of the number of jets, and can be found in Table 7.4.

Process	0-jet	1-jet	2-jet	3-jet	$\geq$ 4-jet
$Z \to ee$	1.026 ± 0.003	1.002 ± 0.005	0.954 ± 0.010	0.938 ± 0.019	0.890 ± 0.031
$Z \to \mu\mu$	0.975 ± 0.002	0.930 ± 0.005	0.908 ± 0.009	0.863 ± 0.018	0.906 ± 0.030

Table 7.4: Estimated sf for Z+jets as a function of number of jets estimated by requiring the invariant mass of the two leptons to be within 80-100 GeV ($\int L = 2.1$ fb^{-1}). The uncertainty is the statistical error propagated through to the sf.

Top The dominant contribution to the opposite-sign channel is from $t\bar{t}$ events. A control region was designed in order to validate this background by requiring at least one b-tagged jet, $E_{\mathrm{T}}^{\mathrm{miss}} > 50$ GeV, and $m_{llj(j)} < 400$ GeV. The first two requirements populate the region with $t\bar{t}$ events, while the last requirement is needed in order to remain orthogonal to the signal region. The non-$t\bar{t}$ processes contribute $< 1\%$. The agreement between data and SM is found to be well within the systematic uncertainty, which are dominated by the uncertainty in correctly identifying a b-tagged jet and the theory uncertainty on the the top quark mass. The yield and associated sf (where the sf is the same as defined previously, but for $t\bar{t}$ instead

of Z+jets) can be found in Table 7.5. No scale factor was applied to MC $t\bar{t}$ events given the good agreement found within the uncertainty.

	ee ± stat ± syst	$\mu\mu$ ± stat ± syst	$e\mu$ ± stat ± syst	ll ± stat ± syst
$t\bar{t}$	134.01 ± 1.90 ± 28.22	136.23 ± 1.93 ± 28.46	677.70 ± 4.36 ± 147.56	947.94 ± 5.13 ± 204.20
t, Wt	9.92 ± 0.82 ± 1.87	12.18 ± 0.86 ± 2.31	46.90 ± 1.66 ± 8.90	69.01 ± 2.04 ± 13.08
Z+jets	0.22 ± 0.16 ± 0.03	0.90 ± 0.48 ± 0.17	1.47 ± 0.55 ± 0.27	2.59 ± 0.74 ± 0.47
Diboson	0.37 ± 0.26 ± 0.08	0.54 ± 0.37 ± 0.12	1.43 ± 0.54 ± 0.19	2.34 ± 0.71 ± 0.40
MC fake	0.08 ± 0.08 ± 0.01	0.00 ± 0.00 ± 0.00	0.64 ± 0.46 ± 0.10	0.72 ± 0.47 ± 0.12
SM	144.61 ± 2.09 ± 28.22	149.85 ± 2.20 ± 28.46	728.13 ± 4.75 ± 147.56	1022.59 ± 5.64 ± 204.21
Data	157 ± 12.53	138 ± 11.75	765 ± 27.66	1060 ± 32.56
Data/SM	1.09 ± 0.09 ± 0.21	0.92 ± 0.08 ± 0.17	1.05 ± 0.04 ± 0.21	1.04 ± 0.03 ± 0.21

Table 7.5: Number of events that passed $t\bar{t}$ control region selection in ee, $\mu\mu$, $e\mu$ and combined ll channels with ≥ 1 jets ($\int L = 2.1$ fb^{-1}).

7.3.4 Charge-Flip Estimate

Contributions of SM processes to the same-sign ee and $e\mu$ channels can occur when an electron from the Z decay emits a hard, Bremsstrahlung photon. The photon can then produce an $e^{\pm}e^{\mp}$ pair, imparting a majority of the energy to an oppositely charged electron ($e^{\pm}_{\text{hard}} \rightarrow e^{\pm}_{\text{soft}}\gamma_{hard} \rightarrow e^{\pm}_{\text{soft}}e^{\pm}_{\text{soft}}e^{\mp}_{\text{hard}}$) yielding a same-sign pair. This effect is not only present in Z decays, but also other SM processes involving electrons such as WW and $t\bar{t}$. It is also not contained to $e^{\pm}e^{\pm}$ channel, but contributes to $e^{\pm}\mu^{\pm}$ as well.

The rate at which this happens is correlated with the amount of material the electron traverses in the detector. Estimates from this background cannot be extracted from simulation due to differences in the amount of material included in simulation compared with the actual detector, therefore a partially data-driven approach is used in order to obtain an accurate estimate.

Method Description The method is built around the probability that an electron will "flip" charge based on the processes described previously. This probability is parameterized as a function of the electron η, to account for the amount of material traversed by the

electron, and p_{T}, to account for kinematic dependencies following the method in Ref. [55]. This p_{T}-η parameterization can be found in Table 7.6, which is derived from simulation. In order to correct for the differences between data and simulation, an η dependent scale factor is measured in inclusive bins of electron p_{T} using a Z tag-and-probe method. The tag-and-probe method is carried out by requiring a same-sign ee event with an invariant mass between 80 and 100 GeV. Both electrons are required to lie in the same η region as used in the parameterization, which insures that one electron has flipped charge and allows for the extraction of the flip probability in data for that given bin. Imposing the requirement that both electrons are in the same η region leads to large statistical uncertainty, which is the dominant source of error for this method. The scale factors and error on the scale factors can be found in Table 7.7.

The probabilities are then used to weight opposite-sign simulated events in order to obtain the estimated contribution to the same-sign signal region. The process follows the simple binomial probability equation:

$$w = p \cdot (1 - q) + q \cdot (1 - p), \tag{7.3}$$

where "p" is the probability that the first electron flipped charge, "q" is the probability that the second electron flipped charge, and w represents the probability that one of the electrons flipped charge, which is used to weight the events. This is done for each opposite-sign event from $Z + jet$, $t\bar{t}$, and diboson backgrounds in order to obtain the final background estimate from this process.

Validation The signal region requires that $m_{\ell\ell} > 110$ GeV, therefore a suitable validation region can be created by reversing this requirement and looking in the ee channel. To further reduce the contributions from other background sources, a window around the Z boson mass of $80 < m_{\ell\ell} < 100$ is constructed. The dominant background in the validation region is from

	[25,45] GeV	[45,65] GeV	[65, 85] GeV	$>$ 85 GeV
[0,0.6]	4.6×10^{-4}	4.0×10^{-4}	4.9×10^{-4}	1.7×10^{-3}
[0.6,1.0]	8.1×10^{-4}	9.1×10^{-4}	2.4×10^{-3}	4.3×10^{-3}
[1.0,1.37]	1.6×10^{-3}	1.6×10^{-3}	2.8×10^{-3}	5.0×10^{-3}
[1.52,2.2]	9.3×10^{-3}	8.5×10^{-3}	1.1×10^{-2}	2.2×10^{-2}
[2.2,2.5]	2.6×10^{-2}	3.1×10^{-2}	4.1×10^{-2}	5.4×10^{-2}

Table 7.6: The p_{T}-η parameterization for the probability that a given electron will flip charge. This probability is derived from simulated $Z \to e^{\pm}e^{\mp}$ events.

$\lvert\eta\rvert$	[0,0.6]	[0.6,1.0]	[1.0,1.37]	[1.52,2.2]	[2.2,2.5]
Scale Factor	1.07 $\pm$ 0.2	0.33 $\pm$ 0.22	0.83 $\pm$ 0.23	0.90 $\pm$ 0.04	0.46 $\pm$ 0.06

Table 7.7: The η dependent scale factors that are to be applied to the parameterization of the the probability for an electron to flip charge.

charge-flip leptons originating from a Z boson decay. In order to compare the charge-flip prediction with what is expected from data, all other SM contributions are subtracted from the data. The expected yield from charge-flip electrons in data, MC, and from the estimate utilizing the flip probabilities can be found in Table 7.8. The data and the result of applying the flip probabilities are in good agreement.

	Same-sign $Z \to ee$
Data	2542 $\pm$ 63
MC prediction	3615 $\pm$ 48.9
Flip probability	2566 $\pm$ 4.6

Table 7.8: The yield from charge-flip electrons in data, MC Z events, and the result of applying the flip probability. The data yields have been adjusted by subtracting off all other SM contributions to this region. Only the statistical uncertainty is given.

Uncertainty The statistical error associated with the parameterization given in Table 7.6 is propagated through to the event weight used in Equation 7.3. An additional systematic error is evaluated based on the choice of binning used in the p_{T}-η parameterization. This is evaluated by shifting the p_{T} and η bins and then reevaluating the probability. Any differences are propagated through to the event weight. The final uncertainty is attached to the scale

factor derived by comparing the probabilities in data and simulation, which is quoted in Table 7.7.

7.3.5 Fake Lepton Background

This section describes a method to estimate the contribution of events with one or two "fake" leptons to the signal region. There are a number of background sources that can contribute to a dilepton signature, for example:

- semi-leptonic decay of a b or c jet
- decay in flight of a $\pi^{\pm}$ or K meson
- reconstruct a π^0 as an electron
- reconstruct a photon as an electron

The dominant processes yielding fake leptons are $b\bar{b}$, $c\bar{c}$, $t\bar{t}$, and W+jets. Simulation fails to produce a reliable estimate due to the uncertainties on the SM cross-section for $b\bar{b}$ and $c\bar{c}$, as well as the difficulty of modeling the lepton kinematic variables produced in this class of processes. For this reason, a fully data-driven estimate is employed to extract the contribution of fake leptons to the signal region.

Method Description The Matrix Method (MM) [56] is used to provide a data-driven estimate for the number of events with non-prompt leptons. The method relies heavily on two measured quantities, the real efficiency (r) and the fake rate (f). The real efficiency is the probability of a real, prompt lepton to pass the tight selection criteria, while the fake rate is the probability of a fake, non-prompt lepton to pass the tight selection criteria. In this analysis, signal leptons satisfy the tight criteria, while baseline leptons pass a looser criteria.

For muons, this means dropping the isolation requirement, and for electrons we loosen the identification criteria from "medium" to "loose" and we drop the isolation.

When estimating the fake lepton background for two leptons, the MM utilizes a system of four equations with four unknowns that can be expressed as a matrix. This matrix relates the number of tight-tight (TT) tight-loose (TL), loose-tight (LT) and loose-loose (LL) leptons in the event to the number of real-real (RR), real-fake (RF), fake-real (FR), and fake-fake (FF) leptons in the event.

$$\begin{pmatrix} N_{TT} \\ N_{TL} \\ N_{LT} \\ N_{LL} \end{pmatrix} = \begin{bmatrix} r_1 r_2 & r_1 f_2 & f_1 r_2 & f_1 f_2 \\ r_1(1-r_2) & r_1(1-f_2) & f_1(1-r_2) & f_1(1-f_2) \\ (1-r_1)r_2 & (1-r_1)f_2 & (1-f_1)r_2 & (1-f_1)f_2 \\ (1-r_1)(1-r_2) & (1-r_1)(1-f_2) & (1-f_1)(1-r_2) & (1-f_1)(1-f_2) \end{bmatrix} \cdot \begin{pmatrix} N_{RR} \\ N_{RF} \\ N_{FR} \\ N_{FF} \end{pmatrix} \quad (7.4)$$

The matrix in equation 7.4 [56] can then be inverted to take the measured quantities $(N_{TT}, N_{TL}, N_{LT}, N_{LL})$ and extract the quantities we want to know (N_{RF}, N_{FR}, N_{FF}) in order to arrive at our final fake lepton estimate.

The method will sample from the region populated by at least two *loose* leptons. From this region the tight lepton selection criteria can be checked and the left hand side of Equation 7.4 can be filled. If there are more than two loose leptons in the event, all permutations to form a dilepton event are considered.

The real efficiency and fake rate are derived in dedicated data control regions and utilize a few different parameterizations. The choice of the kinematic parameterization was based on observed dependencies of the rates and efficiencies for a given variable. Furthermore, a distinction between leptons that passed, or didn't pass the analysis trigger is made in order to account for differences between the rates and efficiencies of the leptons in our loose sample. The lepton in the loose sample is not necessarily required to trigger the event.

Real Efficiency Control Region The real efficiency is measured in a tag-and-probe control region designed to be dominated by real leptons from Z boson decays following Ref. [56]. The control region consists of events that pass the baseline event selection described in Subsection 7.2.1, with the following additional requirements:

- Require exactly two opposite-charge leptons of the same flavor.
- Require at least one tight lepton to be the tag.
- The tight tag lepton triggered the event.
- The additional probe lepton must satisfy the loose criteria.
- Require $86 < m_{\ell\ell} < 96$ GeV.

The probe lepton is used to measure the efficiency of passing the tight lepton selection requirements. In the case where both leptons pass the tight selection, the event is used twice, where each lepton is treated as a probe.

Fake Rate Control Region The fake rate is measured in a single lepton control region, which has slightly different requirements for electrons and muons in order to combat differing background contamination. Both require the baseline event selection with a looser trigger requirement as compared to the signal leptons used in this analysis. The selection criteria for each control region is outlined in Table 7.9. Even with the judicious steps to reduce the contamination from electroweak sources, some residual contamination still exists. Therefore in order to remove the contamination, the MC estimate for Z+jet, W+jet and $t\bar{t}$ is subtracted.

Parameterization Both the muon and electron real efficiency follows a bin parameterization as a function of the lepton p_{T}. The real efficiency is quite flat, with small deviations

Requirement	Electron	Muon
N_ℓ^{loose}	Exactly One	
m_T	< 40 GeV	
$\lvert\Delta\phi(E_T^{miss}, jet)\rvert$	< 0.1	–
$\lvert\Delta\phi(E_T^{miss}, \ell)\rvert$	–	< 0.5
N_{jet}	–	At least One

Table 7.9: The definitions for the control region used to measure the fake rate for electrons and muons. The criteria are developed to reduce the amount of electroweak contamination in the control region.

at low p_{T}. The electron fake rate is parameterized as a function of p_{T} as well, while the muon fake rate utilizes a two-dimensional parameterization as a function of H_T/p_{T} vs. p_{T}, where H_T is defined as the sum of the transverse momentum of the leptons and the jets. The choice of this parameterization is motivated by the large variation of the muon fake rate as a function of this variable as seen in Ref. [55].

Flavor Separation It was found that the fake rate for a muon from a heavy flavor (HF) jet was significantly different than it was for a light flavor (LF) jet, and for this reason an additional separation is done for the muon fake rate [55]. An additional requirement is imposed upon the control region definitions outlined in Table 7.9 to separate these two processes. In order for the muon to be considered as having originated in a HF jet, the muon has either an overlapping ($\Delta R(\mu, jet) < 0.4$) b-tagged jet, or a b-tagged jet sufficiently far from the muon ($\Delta R(\mu, jet) > 2.0$). The latter requirement is to pick up $b\bar{b}$ decays where one of the jets is lost. In order for the muon to be considered as having originated in a LF jet, the muon either has no overlapping jet and no jet with $\Delta R(\mu, jet) > 2.0$, or it has an overlapping jet that fails the b-tagging requirements. Unlike in Ref. [55], the separateion was found to have a negligible impact for electrons.

Fake Rate and Real Efficiency The real efficiency and fake rate are measured in the control regions described previously and corrected for electroweak contamination as esti-

mated in MC. The efficiencies and rates for the electrons can be found in Figure 7.3 and for muons in Figure 7.4. The distinction between whether or not the lepton passed or failed the trigger is made in the legend. For the HF and LF muon fake rate, this distinction is not made since the variation was found to be negligible compared to the statistical error of further dividing this sample.

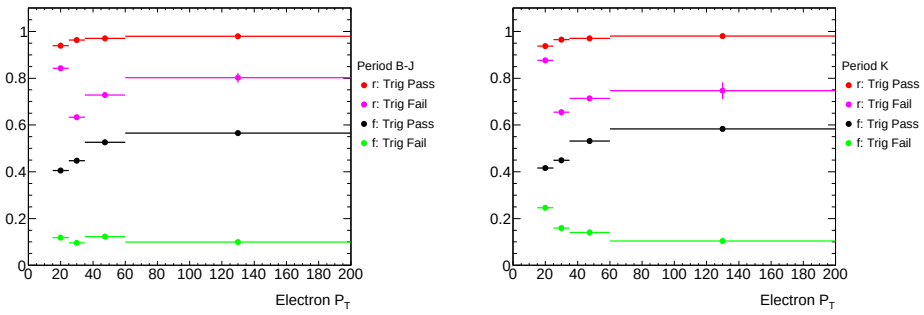

Figure 7.3: Electron bin-parameterization for f and r as a function of E_T, for passed trigger and failed trigger. No MC background subtraction was applied, since contamination was found to be negligible. Similar to muons, when the analysis trigger became tighter, the fake rate shifted, and we take this into account. Again, the shape for periods B through J (Left) is comparable to period K (Right), where the largest difference is seen in the low P_T region.

Validation Region In order to validate that the matrix method is reproducing the observed fake background, a validation region is constructed to be orthogonal to the signal region by requiring that the subleading lepton satisfies $15 < p_{\mathrm{T}}^{subleading} < 25$ GeV. Only same-sign region is checked as that is where the fake background is dominant.

Figure 7.5 and Figure 7.6 show the predicted and measured fake background as a function of $m_{\ell\ell}$ and p_{T} respectively. The black markers in this histogram show the observed fake leptons by taking the full data yield in the validation region and subtracting off the contribution from prompt leptons. The fake prediction from the matrix method is given in blue, along with the associated errors propagated through the matrix method, which are shown as hatched boxes. The yellow bands shown in the ratio plot below each figure illustrates the additional systematic uncertainty to cover the variations seen in this validation region. A summary of

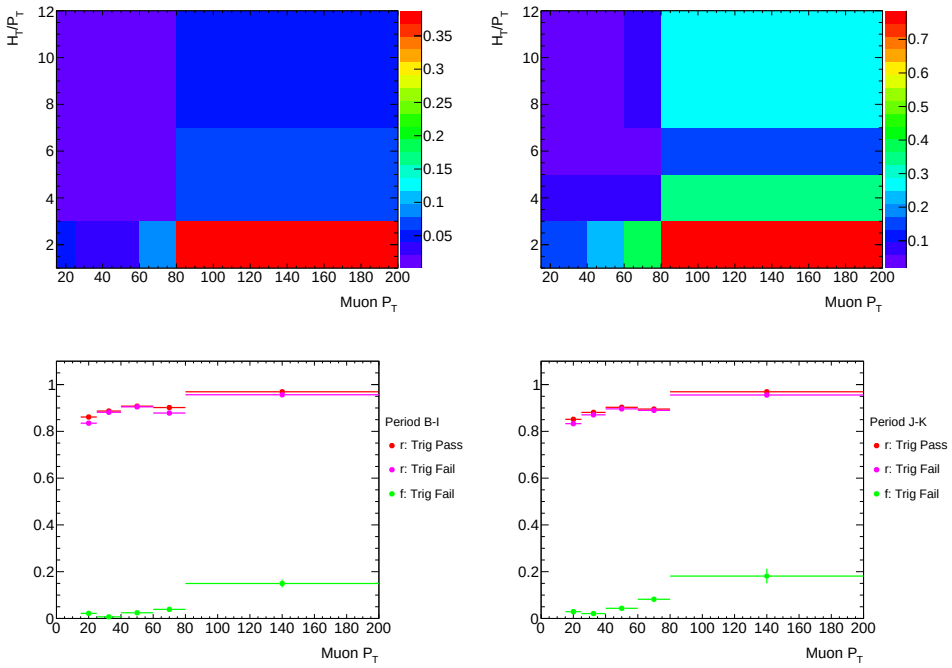

Figure 7.4: Muon bin-parameterization as functions of H_T/P_T vs. P_T for f for triggered muon in the enriched HF sample (top left) and the enriched LF sample(top right), after MC background subtraction. Real efficiency, r, parameterized as a function of P_T for pass and failed trigger muon. Due to low statistics, the failed triggered f is parameterized against P_T only. From period J onward a new analysis trigger was used which impacted the fake rate, and had marginal impact on the real efficiency. The shape for periods B through I (bottom left) are very similar to that of periods J and K (bottom right) however the rates themselves differ, most notably in the low P_T region near trigger threshold.

the total yield can be found in Table 7.10.

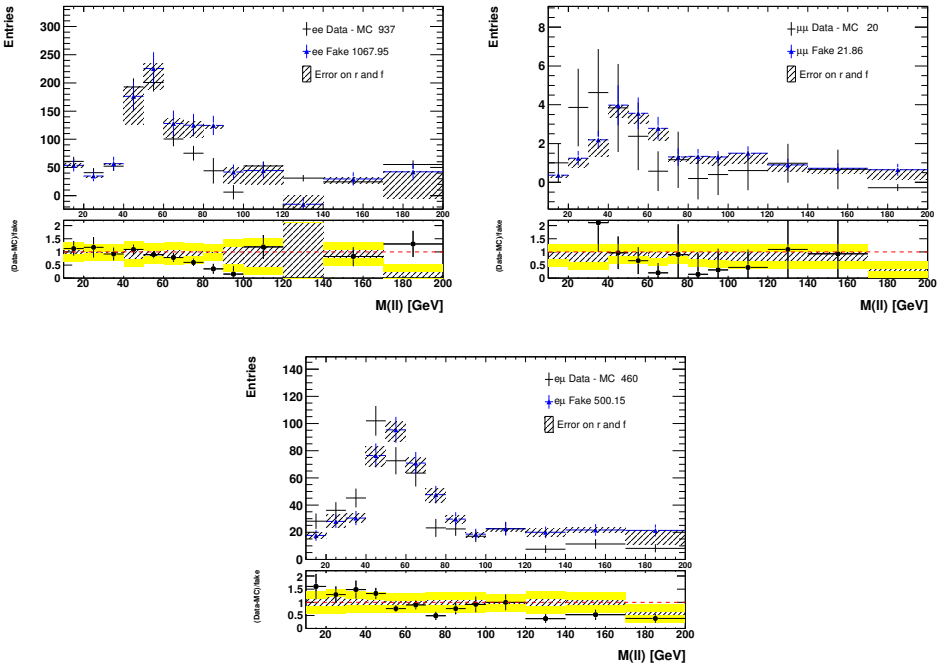

Figure 7.5: The dilepton invariant mass for ee (top left) $\mu\mu$ (top right) and $e\mu$ (bottom) for events where the leading lepton has $p_{\mathrm{T}} > 25$ GeV and subleading lepton satisfies $15 < p_{\mathrm{T}} < 25$ GeV. The hatched boxes show the uncertainties on the real efficiency and fake rate propagated through the matrix method. The yellow band shows the additional uncertainty added in order to cover the the variations seen in the ratio plot.

	$e^{\pm}e^{\pm}$	$\mu^{\pm}\mu^{\pm}$	$e^{\pm}\mu^{\pm}$
Fake Predicted	1067.95 ± 63.53 ± 186.74	21.86 ± 1.81 ± 5.93	500.15 ± 21.49 ± 62.48
Data - MC	937	20	459
Data-MC/Fake Predicted	0.88 ± 0.05 ± 0.15	0.91 ± 0.08 ± 0.25	0.92 ± 0.04 ± 0.11

Table 7.10: Predicted fake and observed fake (Data-MC) for each channel in the validation region for same-sign leptons requiring subleading lepton satisfy $15 < p_{\mathrm{T}}^{subleading} < 25$ GeV.

Uncertainty The first source of uncertainty is simply taken from the statistical uncertainty from the real efficiency and fake rate parameterization. This uncertainty is propagated through the matrix method by varying the real efficiency and fake rate by the uncertainty associated with that particular bin, and then recalculating the event weight.

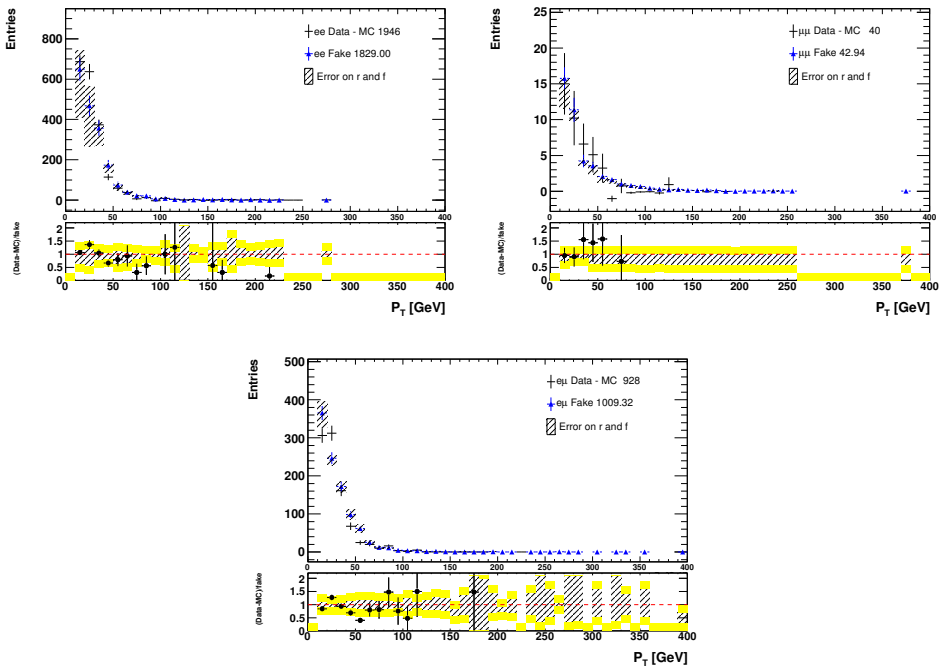

Figure 7.6: Lepton p_{T} for ee (top left) $\mu\mu$ (top right) and $e\mu$ (bottom) for events where the leading lepton has $p_{\mathrm{T}} > 25$ GeV and subleading lepton satisfies $15 < p_{\mathrm{T}} < 25$ GeV. The hatched boxes show the uncertainties on the real efficiency and fake rate propagated through the matrix method. The yellow band shows the additional uncertainty added in order to cover the the variations seen in the ratio plot.

In addition to the nominal statistical error on the estimate, an error associated with the number of tight and loose leptons in the loose sample is estimated. For a given region, or a given bin in a histogram, if one of the necessary pairs appearing on the left hand side of Equation 7.4 is missing an additional statistical error is included by borrowing the necessary pair from a neighboring bin and including the error associated with that particular event.

The third source of uncertainty is derived from the level of agreement in the validation region, as shown in Figure 7.5 and Figure 7.6. This is assessed by looking at how well the data fake (data - MC) is reproduced by the fake prediction from the matrix method. The error is estimated to be a flat 30%.

The final uncertainty is derived from a closure test on the parameterization itself. The data is randomly divided into two equal sets. Measurements of the fake rate and real efficiency are extracted from the first set and are used to predict the fake rate and real efficiency in the second set. The measured and predicted values are then compared as a function of many variables, and an uncertainty is extracted based on the level of agreement. For the electron fake rate the error is found to be 20% if $1 < |\eta| < 2$ and 5% otherwise, while the real efficiency has a flat 2% uncertainty. For the muon fake rate (real efficiency) the uncertainty is a flat 40% (5%). This uncertainty is then propagated through the matrix method to obtain the contribution to the final estimate.

7.4 Signal Regions

7.4.1 LRSM Signal Region

The approach for the LRSM is to utilize the two leptons and up to two jets to reconstruct the hypothetical W_R produced in the event, as shown in Figure 7.2. This is done to remove

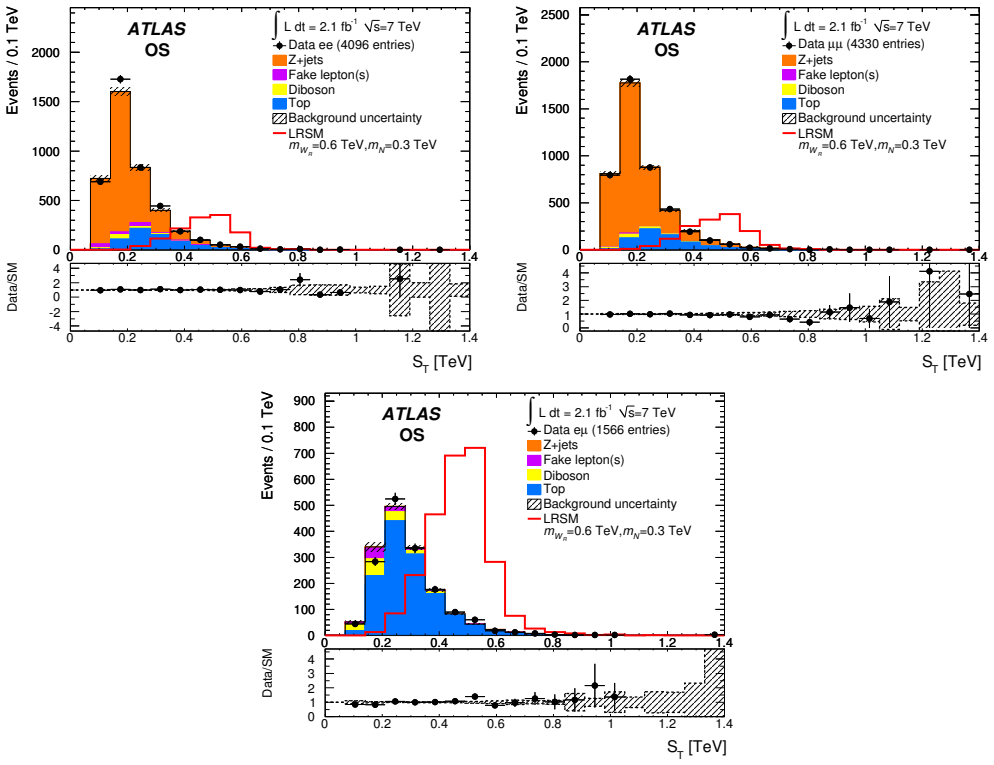

Figure 7.7: The distribution for the sum of transverse energy of the two leptons and up to two leading jets (S_T) for the opposite-sign ee (top-left), $\mu\mu$ (top-right), and $e\mu$ (bottom) channels for events with two leptons and at least one jet and $m_{\ell\ell} > 110$ GeV. The hypothetical signal distribution for $m_{W_R} = 0.6$ TeV and $m_N = 0.3$ TeV in the case of maximal mixing is overlaid.

the ambiguity in reconstructing the heavy neutrino, which requires just one lepton from the dilepton final state.

Two separate signal regions are defined based on the charge of the leptons: same-sign or opposite-sign. For both regions a minimum reconstructed W_R mass of 400 GeV is imposed. In addition, the opposite-sign region must have the scalar sum of transverse momentum of the objects used to reconstruct the W_R (two leptons and at most two jets) be greater than 400 GeV. The dominant backgrounds for the opposite-sign region peak for values less than 400 GeV, while several signal points extend well beyond this region as illustrated in Figure 7.7.

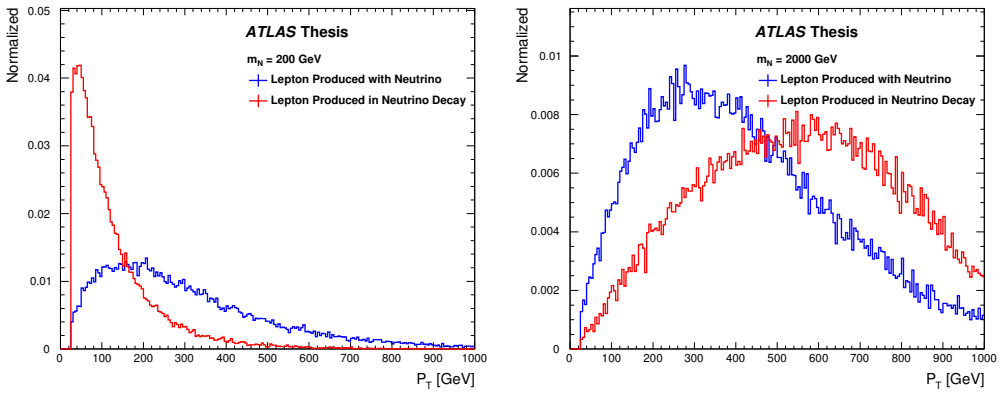

Figure 7.8: Lepton p_{T} distributions for $m_N = 200$ GeV (left) and $m_N = 2000$ GeV (right). This figure illustrates how the neutrino mass influences the final state kinematics.

7.4.2 HNEO Signal Region

In the effective operator approach the search variable is the hypothetical neutrino mass. The final state includes two leptons and two jets, as illustrated in the Feynman diagram in Figure 7.1, which presents a problem since one must choose a lepton to use in the reconstruction of the neutrino mass.

It was found that for lighter N masses, the lepton from the decay of the N was found to have a softer p_{T} spectrum when compared with the lepton produced with N. This situation changed as the mass of N increases as seen in Figure 7.8. A set of criteria based on the angular information and the reconstructed neutrino mass ($m_N = m_{\ell jj}$) was used to determine which lepton fit best. It was found that that if the angle between the the leading lepton and the leading jet was greater than 0.00157 of the reconstructed neutrino mass using the leading lepton, then the leading lepton was chosen. That is if $\alpha(\ell_0, j_0) > 0.00157 \cdot m_{\ell_0 j_0 j_1}$, then use $m_{\ell_0 j_0 j_1}$. Otherwise the subleading lepton was used for the reconstructed neutrino mass ($m_{\ell_1 j_0 j_1}$). This set of criteria was derived by studying the relationship between $\alpha(\ell_0, j_0)$ and $m_{\ell_0 j_0 j_1}$ for the N mass spectrum considered. The net effect is that for $m_N \geq \Lambda/2$ (= 1.5 TeV) the leading lepton is chosen, while for $m_N \leq 1.5$ TeV the subleading lepton is chosen.

After choosing the lepton for the reconstructed N mass, the events are separated into two categories based on the lepton charge: same-sign and opposite-sign. No additional selection is placed on the same-sign region. The opposite-sign region needed further requirements in order to reduce the background from Z+jet and $t\bar{t}$ production. A requirement on the scalar sum of transverse energy from the two leptons and up to two jets (called S_T) was required to be greater than 400 GeV.

7.5 Results

The number of events expected and observed for each dilepton final state for HNEO signal region and LRSM signal region can be found in Table 7.11 and Table 7.12 for the opposite-sign and same-sign channels respectively. In addition, the kinematic variables of interest, $m_{\ell\ell j(j)}$ in the case of LRSM and $m_{\ell j(j)}$ in the case of HNEO, can be found for opposite sign (same-sign) in Figure 7.9 (Figure 7.10) and Figure 7.11 (Figure 7.12). Good agreement is found in all channels and signal regions.

Physics Processes	$e^{\pm}e^{\mp}$	$\mu^{\pm}\mu^{\mp}$	$e^{\pm}\mu^{\mp}$	Total
Z/γ^*+jets	136.1 ± 12.5	173.2 ± 15.1	0.8 ± 0.8	310 ± 20
Diboson	4.3 ± 1.8	7.3 ± 1.9	5.9 ± 1.6	18 ± 3
Top	103.1 ± 12.3	100.9 ± 12.0	199.4 ± 23.3	403 ± 46
Fake lepton(s)	12.5 ± 8.1	-0.2 ± 0.7	6.1 ± 4.2	18 ± 9
Total Background	256.0 ± 26.2	281.2 ± 27.9	212.3 ± 33.8	750 ± 78
Observed events	248	245	247	740
	$m_{\ell\ell j(j)} \geq 400$ GeV			
Total Background	254.8 ± 25.8	279.7 ± 27.6	210.9 ± 33.4	745 ± 77
Observed events	246	241	244	731

Table 7.11: Summary of the expected background yields and observed numbers of events for the OS dilepton channels. The top part of the table shows the numbers obtained for events with two leptons, ≥ 1 jet, $m_{\ell\ell} > 110$ GeV and $S_{\mathrm{T}} > 400$ GeV. The bottom part of the table shows the numbers for the final LRSM selection, where an additional requirement $m_{\ell\ell j(j)} \geq 400$ GeV is imposed. The quoted uncertainties include statistical and systematic components, excluding the luminosity uncertainty of ±3.7%. The latter is relevant for all backgrounds except for the fake lepton(s) background, which is measured using data.

Physics Processes	$e^{\pm}e^{\pm}$	$\mu^{\pm}\mu^{\pm}$	$e^{\pm}\mu^{\pm}$	Total
Z/γ^*+jets	26.1 ± 5.6	$0.0\ ^{+1.6}_{-0}$	1.2 ± 0.7	27 ± 6
Diboson	12.7 ± 2.3	7.2 ± 1.7	18.8 ± 3.0	39 ± 6
Top	5.8 ± 1.3	0.7 ± 0.3	6.8 ± 1.6	13 ± 3
Fake lepton(s)	93.6 ± 35.7	3.1 ± 1.6	53.8 ± 20.3	151 ± 50
Total Background	138.3 ± 36.5	$11.0\ ^{+2.9}_{-2.5}$	80.7 ± 20.8	230 ± 52
Observed events	155	14	99	268
	$m_{\ell\ell j(j)} \geq 400$ GeV			
Total Background	48.4 ± 16.1	$4.4\ ^{+2.1}_{-1.3}$	24.6 ± 7.6	77 ± 21
Observed events	59	8	39	106

Table 7.12: Summary of the expected background yields and observed numbers of events for the SS dilepton channels. The top part of the table shows the numbers obtained for events with two leptons, ≥ 1 jet and $m_{\ell\ell} > 110$ GeV. The bottom part of the table shows the numbers for the final LRSM selection, where an additional requirement $m_{\ell\ell j(j)} \geq 400$ GeV is imposed. The quoted uncertainties include statistical and systematic components, excluding the luminosity uncertainty of $\pm 3.7\%$. The latter is relevant for all backgrounds except for the fake lepton(s) background, which is measured using data.

Model Independent Limits Overall good agreement is observed in Table 7.11 and Table 7.12 between the SM prediction and the observed values in data. These results are used to set 95% C.L. limits on the visible cross section, $\sigma\mathcal{A}\epsilon$, where σ is the cross section for a new process, $\mathcal{A}$ is representative of the acceptance (the fraction of events passing the selection requirements at particle level), and ϵ is the detector reconstruction and identification efficiency. The expected and observed values can be found in Table 7.13.

Channels	$\langle\sigma\mathcal{A}\epsilon\rangle^{95}_{\text{obs}}$ [fb]	$\langle\sigma\mathcal{A}\epsilon\rangle^{95}_{\text{exp}}$ [fb]
$e^{\pm}e^{\mp}$	28.6	31.0
$\mu^{\pm}\mu^{\mp}$	25.1	36.7
$e^{\pm}\mu^{\mp}$	50.9	36.4
$e^{\pm}e^{\pm}$	37.6	29.6
$\mu^{\pm}\mu^{\pm}$	6.1	4.6
$e^{\pm}\mu^{\pm}$	25.4	16.2

Table 7.13: Observed (obs) and expected (exp) 95% C.L. upper limits on the visible cross section, $\langle\sigma\mathcal{A}\epsilon\rangle^{95}$, for each OS and SS dilepton channel after the baseline selection.

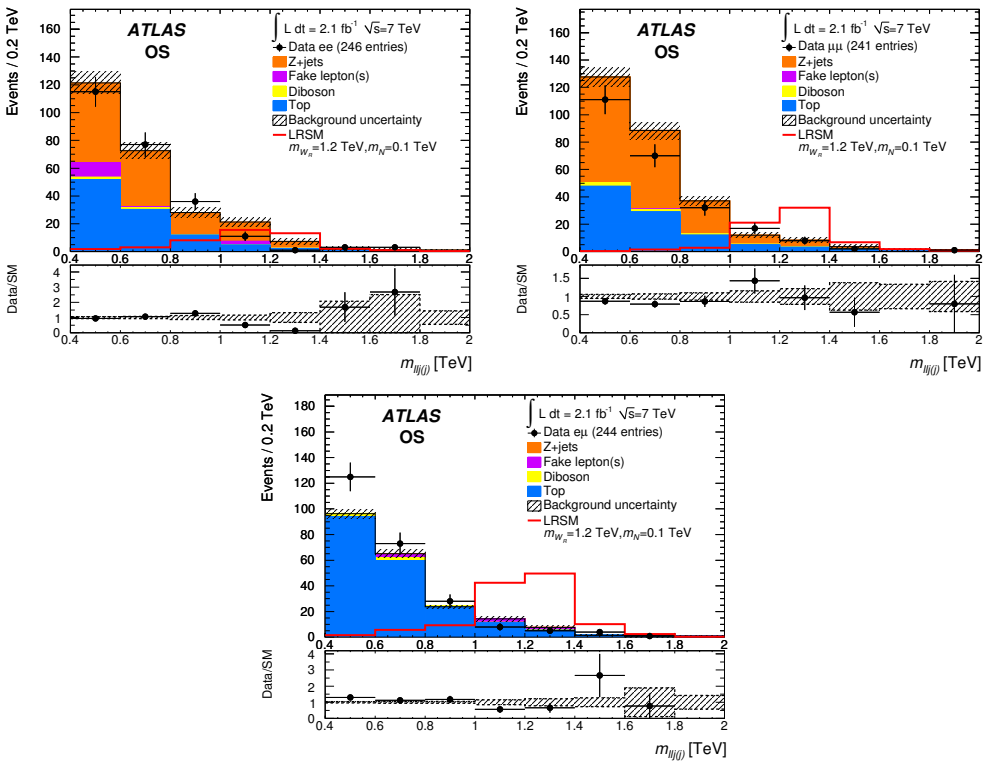

Figure 7.9: Distribution of the invariant mass of two leading leptons and up to two leading jets (only one is used if no second jet is found) for opposite-sign events with ≥ 1 jets, $m_{\ell\ell} > 110$ GeV and $m_{\ell\ell j(j)} > 400$ GeV. The distribution is shown for the ee (top left), $\mu\mu$ (top right) and $e\mu$ (bottom) channels. The events have an additional requirement of $S_T \geq 400$ GeV. The hypothetical signal distribution for $m_{W_R} = 1.2$ TeV and $m_N = 0.1$ TeV for the case of maximal mixing is overlaid.

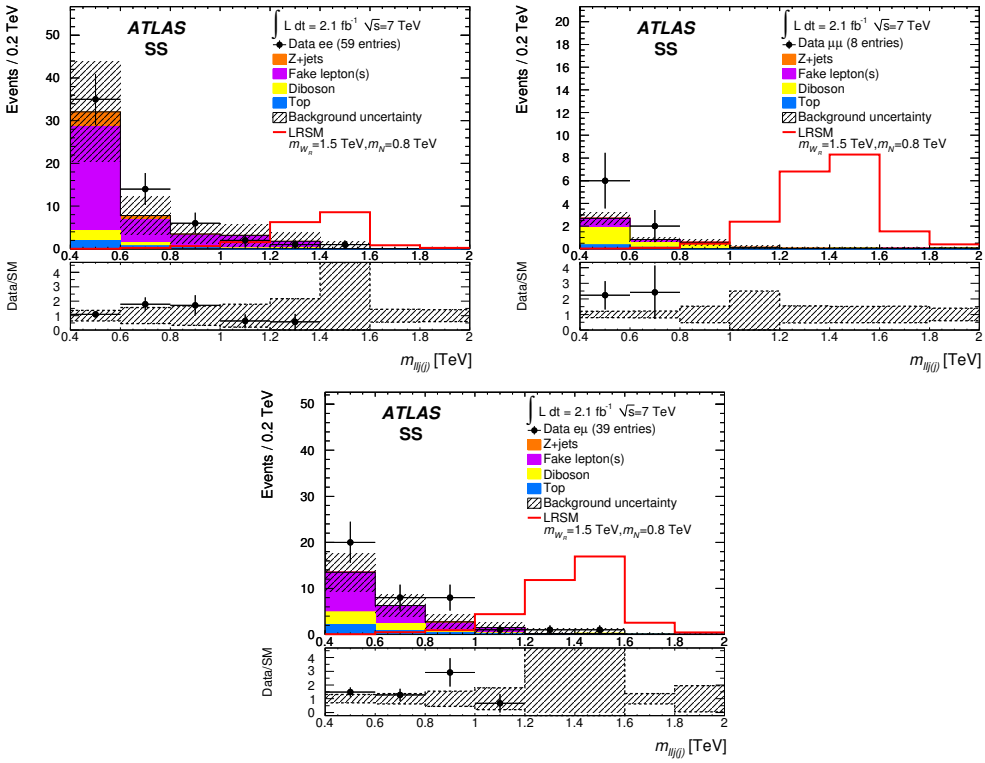

Figure 7.10: Distribution of the invariant mass of two leading leptons and up to two leading jets (only one is used if no second jet is found) for same-sign events with ≥ 1 jets, $m_{\ell\ell} > 110$ GeV and $m_{\ell\ell j(j)} > 400$ GeV. The distribution is shown for the ee (top left), $\mu\mu$ (top right) and $e\mu$ (bottom) channels. The hypothetical signal distribution for $m_{W_R} = 1.2$ TeV and $m_N = 0.1$ TeV for the case of maximal mixing is overlaid.

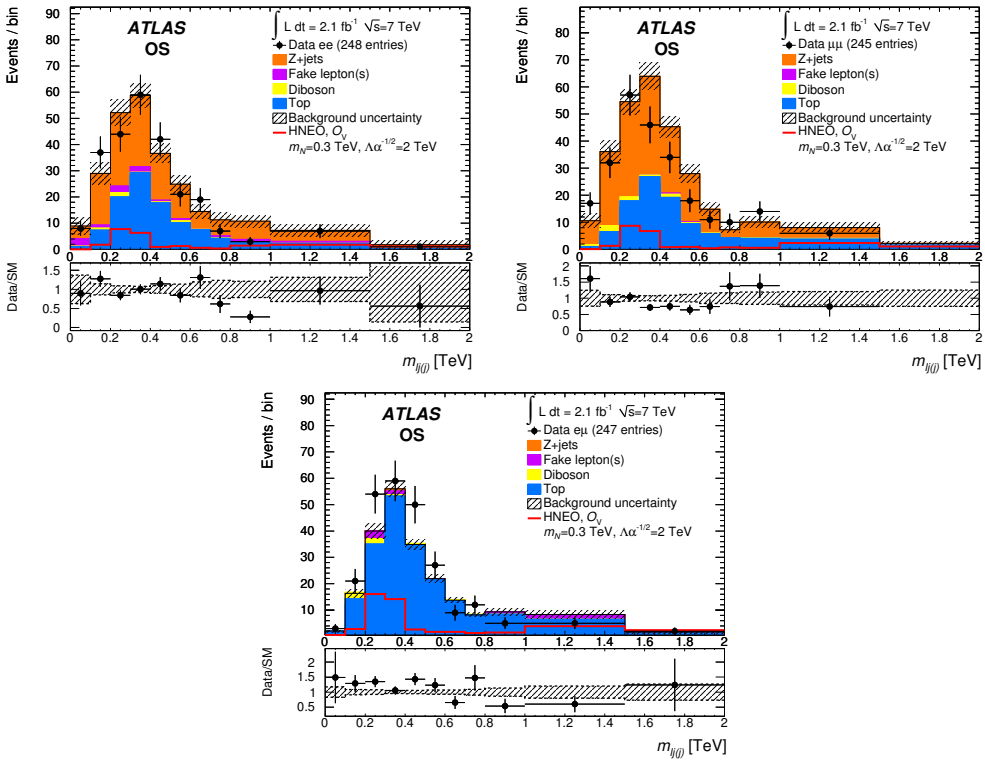

Figure 7.11: Distribution of the invariant mass of a leading lepton and up to two leading jets (only one is used if no second jet is found) for opposite-sign events with ≥ 1 jets and $m_{\ell\ell} > 110$ GeV. The distribution is shown for the ee (top left), $\mu\mu$ (top right) and $e\mu$ (bottom) channels. The events have an additional requirement of $S_T \geq 400$ GeV. The hypothetical signal distribution for $m_N = 0.3$ TeV for the vector operator and $\Lambda/\sqrt{\alpha} = 2$ TeV is overlaid

.

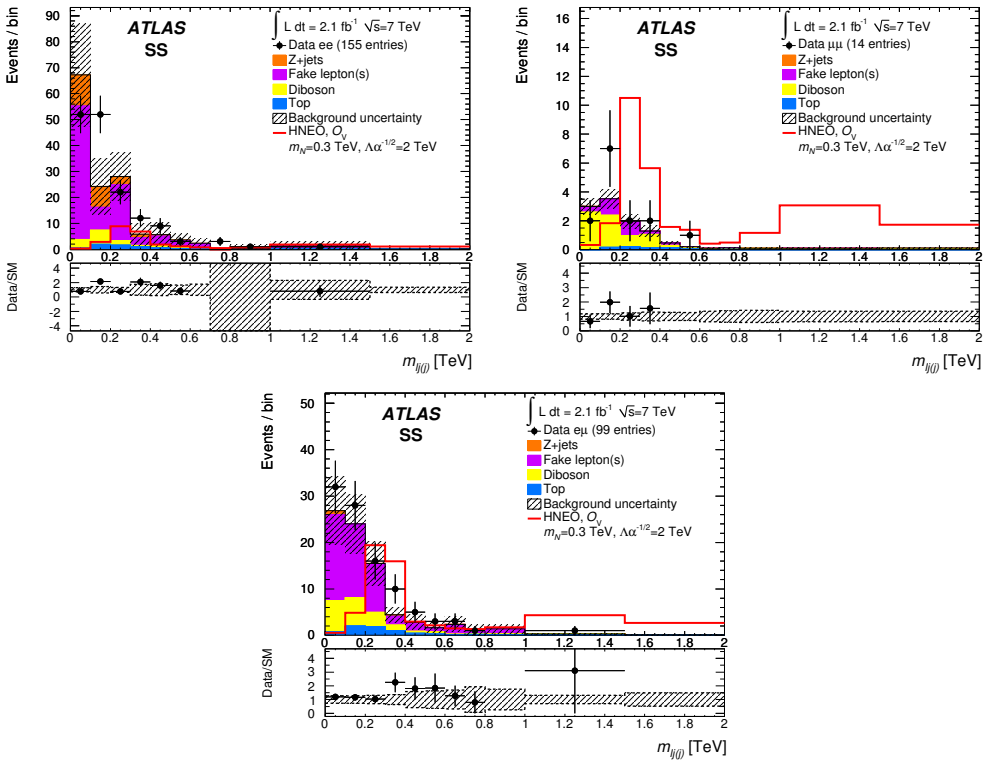

Figure 7.12: Distribution of the invariant mass of a leading lepton and up to two leading jets (only one is used if no second jet is found) for opposite-sign events with ≥ 1 jets and $m_{\ell\ell} > 110$ GeV. The distribution is shown for the ee (top left), $\mu\mu$ (top right) and $e\mu$ (bottom) channels. The hypothetical signal distribution for $m_N = 0.3$ TeV for the vector operator and $\Lambda/\sqrt{\alpha} = 2$ TeV is overlaid

.

Model Dependent Limits In the absence of a signal, 95% C.L. exclusion limits are set in the context of HENO and LRSM using the Bayesian approach [57]. In this approach the systematic uncertainties are treated as nuisance parameters with a truncated Gaussian used as a prior shape. The parameter of interest ($\sigma\times$ BR) is assumed to be flat.

The 95% C.L. exclusion limits for HNEO are set as a function of neutrino mass (m_N) and the ratio of the scale of new physics (Λ) and the square root of the coupling ($\sqrt{\alpha}$). These limits for the case of Majorana and Dirac neutrino types can be found in Figure 7.13.

In the case of LRSM, 95% exclusion limits are placed in the two dimensional space of m_N and m_{W_R}. Both cases of Majorana and Dirac neutrino types are considered, and exclusion limits are given in Figure 7.14.

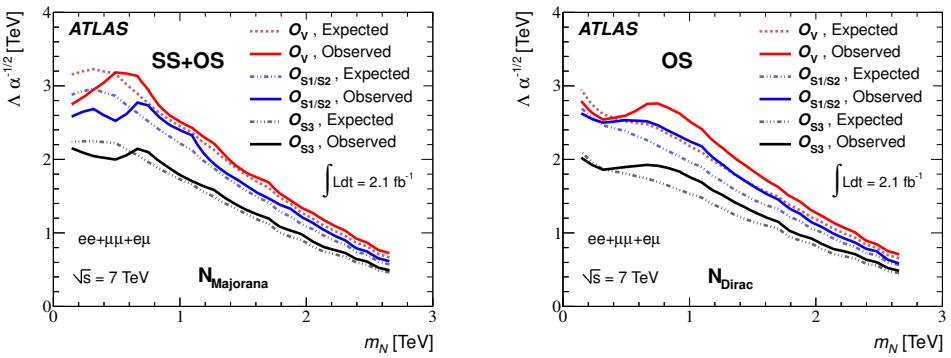

Figure 7.13: Expected and observed 95% C.L. upper limits on $\Lambda/\sqrt{\alpha}$ as a function of the hypothetical neutrino mass for the operators $\mathcal{O}_V$, $\mathcal{O}_{s1}/\mathcal{O}_{s2}$, and $\mathcal{O}_{s3}$ in the framework of HNEO. These limits are for the case where the neutrino is Majorana (left) and Dirac (right).

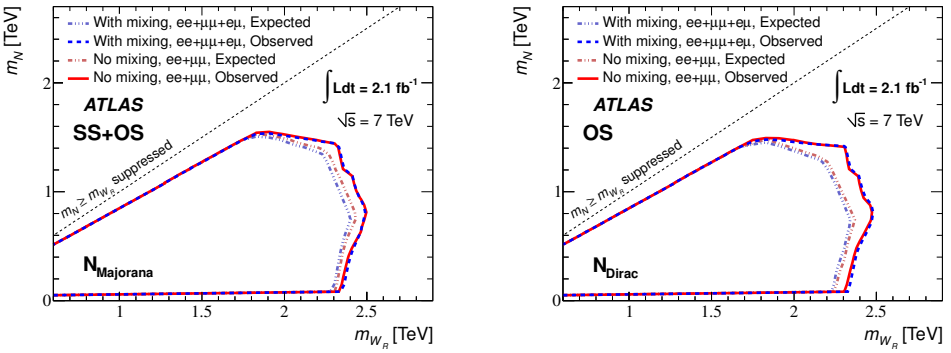

Figure 7.14: Expected and observed 95% C.L. upper limits on the heavy neutrino mass and the mass of W_R for the no mixing and maximal mixing scenarios. These limits are for the case where the neutrino is Majorana (left) and Dirac (right).

Chapter 8

Search for Weakly Produced SUSY

8.1 Interpretations

The search for direct SUSY electroweak production of neutralinos, charginos, and sleptons with R-parity conservation are addressed in this dissertation. The simplified model approach is utilized for these searches, which builds upon the assumptions of the pMSSM discussed in Section 3.2 in order to create general models probing final states with two leptons and missing energy. The details for the chargino and neutralino search are detailed in Subsection 8.1.1, while the details for slepton pair production can be found in Subsection 8.1.2. All samples are generated with `HERWIG++` [58] and the signal cross sections are calculated using `PROSPINO2.1` [1] at NLO.

8.1.1 Chargino and Neutralino Production

The simplified model approach is to reduce the parameter space of SUSY down to the relevant particle content that will dictate the kinematics of the final state. This gives particle

physicists the ability to scan parameters that correspond to physical observables, for example mass. The parameters include the gaugino masses, the masses of intermediate particles, and the mass of the LSP [59]. If no new physics signature is found, this framework allows one to set upper limits on cross-section times the brancing ratio ($\sigma\times$BR), which allows the limit result to be applied to other models with similar kinematic features, making this a powerful search strategy.

All of the gaugino masses and the mixing parameters can be determined from M_1, M_2 and μ [12]. An interesting limit exists where $|\mu| \gg |M_1, M_2| \gg m_Z$, where m_Z is the mass of the SM Z boson. In this limit, $\tilde{\chi}_1^0$ is $\tilde{B}$, $\tilde{\chi}_2^0$ is $\tilde{W}^0$, and $\tilde{\chi}_1^\pm$ is $\tilde{W}^\pm$ [12]. Additionally, it is assumed $M_1 \approx M_2/2$, which is indirectly implied when imposing unification of the gauge couplings [12]. This implies that $\tilde{\chi}_1^\pm$ and $\tilde{\chi}_2^0$ are degenerate. The higgsino component is relegated to the higher mass gaugino terms and does not participate. These simplifying assumptions, along with the possibility for the gauginos to decay to on-shell left-handed sleptons dictate the decays of $\tilde{\chi}_1^\pm$ and $\tilde{\chi}_2^0$.

In this search, only the lightest gauginos resulting in a dilepton final state need to be considered: $\tilde{\chi}_1^\pm\tilde{\chi}_1^\mp$, $\tilde{\chi}_1^\pm\tilde{\chi}_2^0$, and $\tilde{\chi}_2^0\tilde{\chi}_2^0$. In this analysis $\tilde{\chi}_2^0\tilde{\chi}_2^0$ is disregarded due to a lack of sensitivity. In the case of $\tilde{\chi}_1^\pm\tilde{\chi}_1^\mp$, each chargino decays into either a slepton or a sneutrino with equal branching fractions. The slepton (sneutrino) then promptly decays to a lepton (neutrino) and a $\tilde{\chi}_1^0$, yielding a dilepton final state with missing energy from the neutrinos and $\tilde{\chi}_1^0$. The mass range for $\tilde{\chi}_1^\pm$ ($\tilde{\chi}_1^0$) scanned in this analysis is 100-600 GeV (0-500 GeV), which is dictated by the experimental sensitivity. The intermediate sleptons are set such that $m_{\tilde{l}} = m_{\tilde{\nu}} = (m_{\tilde{\chi}_1^0} + m_{\tilde{\chi}_1^\pm})/2$.

For $\tilde{\chi}_1^\pm\tilde{\chi}_2^0$, the $\tilde{\chi}_1^\pm$ decays to $W^\pm\tilde{\chi}_1^0$ and $\tilde{\chi}_2^0$ decays to $Z\tilde{\chi}_1^0$. In this scenario the slepton masses are assumed to be much larger than $\tilde{\chi}_1^\pm$ and $\tilde{\chi}_2^0$, suppressing their branching fraction and favoring the production of SM W and Z boson. Only the cases where W decays hadronically and Z decays leptonically are considered in this dilepton search. The masses for $\tilde{\chi}_1^\pm$ and $\tilde{\chi}_2^0$

are degenarate and the search is performed in the range 100-500 GeV, while the mass of $\tilde{\chi}_1^0$ is scanned from 0-450 GeV.

8.1.2 Slepton Pair Production

Direct slepton production is searched for using a similar framework as described in Subsection 8.1.1 but following the simplifications described in [60]. The mass parameter M_1 is kept at the electroweak scale such that $\tilde{\chi}_1^0$ is accessible at the LHC, while M_2 and μ are set such that all other neutralinos and charginos are not accessible. All sfermion masses except the left- and right-handed selectron and smuon masses are assumed too large to be produced given that this search is for direct production of the light charged sleptons in a dilepton final state.

In this search, the $\tilde{\chi}_1^0$ mass can range from 0-200 GeV, while the selectron and smuon masses are scanned from 100-370 GeV. The lower bounds are influenced by the limits from LEP [61] and the upper bounds are dictated by the estimated sensitivity. The selectron and smuon masses are required to satisfy $m_{\tilde{\ell}} \geq m_{\tilde{\chi}_1^0} + 30$ GeV in order to insure that the lepton produced in the decay will be above the energy threshold to be included in this analysis.

8.2 Selection

8.2.1 Event Selection

Events selected for this analysis are required to satisfy a suite of quality criteria to insure that the data is free from instrumental effects and beam backgrounds. In addition, there must be one primary vertex with at least 5 tracks originating from it. If additional vertices are reconstructed, the one having the highest $\Sigma(p_{\mathrm{T}}^{track})^2$ is chosen.

Within each event, "candidate" electrons, muons, and jets are selected and required to be non-overlapping, following the criteria outlined in Table 8.1.

ΔR Requirement	Comment
$\Delta R(e_1, e_2) < 0.05$	Remove the electron with the lowest cluster E_T.
$\Delta R(j, e) < 0.2$	Remove the jet. A jet can be counted as an electron in reconstruction and this removes the ambiguity.
$\Delta R(\tau, e) < 0.2$	The tau is removed.
$\Delta R(\tau, \mu) < 0.2$	The tau is removed.
$\Delta R(j, e) < 0.4$	The electron is removed. An electron inside a jet is not characteristic of our signal samples.
$\Delta R(j, \mu) < 0.4$	The muon is removed. A muon inside a jet is not characteristic of our signal samples.
$\Delta R(\mu, \mu) < 0.01$	Both electron and muon are removed as this is not characteristic of our signal samples.
$\Delta R(\mu, \mu) < 0.05$	Both muons are removed as this is not characteristic of our signal samples.
$\Delta R(j, \text{signal}\tau) < 0.2$	The jet is removed to eliminate the ambiguity between the two objects.

Table 8.1: Details of the various overlap requirements. The requirements are applied from top to bottom in order to remove any duplication of objects from the various reconstruction algorithms.

Throughout the remainder of this chapter, reference will be made to **baseline** and **signal** objects (eg. baseline electron, signal muon, etc). This analysis selects events with exactly two baseline light leptons after overlap removal, a distinction that will become relevant when discussing the background estimation technique for fake leptons. Only leptons with opposite charge are considered, and the invariant mass of the dilepton system must be greater than 20 GeV to remove any low-mass resonances. The following paragraphs will detail the object selection and the corresponding baseline and signal criteria.

Electron Baseline electrons are required to pass the "medium" selection criteria [41], which is based on of the EM calorimeter shower shape, energy leakage in the hadronic calorimeter, track-cluster matching and track properties. Baseline electrons must also have $E_T > 10$ GeV after applying energy scale and resolution corrections and have $|\eta| < 2.47$ to satisfy the

offline trigger and geometrical acceptance requirements.

Signal electrons must satisfy the "tight" selection criteria [41] along with additional requirements on the impact parameters to further insure prompt electrons are chosen. Specifically, they must have $|d_0/\sigma_{d_0}| < 5$ and $|z_0 \times \sin(\theta)| < 0.4$ mm, which acts to reduce the contributions for electrons produced in the decay of long lived particles (eg. semi-leptonic decay of b quark) that will have a displaced vertex with respect to the primary vertex. In addition, signal electrons are required to pass both calorimeter and track isolation.

The calorimeter isolation is measured from the topological cluster in a cone of $R = 0.3$ around the electron and corrected on average for the dependence on pileup. A relative cut at 18% of the electron p_{T} is used. The track isolation is measured by summing the transverse momentum of tracks with $p_{\mathrm{T}} > 400$ MeV in a cone of $R = 0.3$ around the electron. A relative cut at 16% of the electron p_{T} is used. These requirements aid to reduce the effect of jets being selected as electrons.

Muon Baseline muons are reconstructed by matching a muon spectrometer track to and ID track. They must satisfy the kinematic requirements of $p_{\mathrm{T}} > 10$ GeV and $|\eta| < 2.4$. Muons must also be reconstructed with sufficient hits in the inner detector in order to be considered for this analysis.

Signal muons are required to have $|d_0/\sigma_{d_0}| < 3$ and $|z_0 \times \sin(\theta)| < 1$ mm, which are tighter than the requirements on the impact parameters for electrons. Muons must also pass a track isolation requirement, where the sum of the transverse momentum of the tracks with $p_{\mathrm{T}} > 1$ GeV in a cone of $R = 0.3$ around the muon must be less than 12% of the muon p_{T}. This, along with the impact parameter requirements, aid to reduce the number of non-prompt muons contributing to the signal regions.

Jet This analysis uses LCW jets with a distance parameter of $R = 0.4$. Baseline jets are required to have $p_{\mathrm{T}} > 20$ GeV and $|\eta| < 4.5$. A jet is tagged as a b-jet using the multivariate approach described in [28].

The jets are then divided into three categories of signal jets: central light jets, central b-jets, and forward jets. The classification is based on p_{T}, η, whether or not the jet is b-tagged, and the requirement on JVF. The requirements are given in Table 8.2.

Variable	Central Light Jets	Central b-jets	Forward Jets
p_{T} [GeV]	> 20	> 20	> 30
$\|\eta\|$	< 2.4	< 2.4	[2.4,3.4]
b-tagged	no	yes	not checked
|JVF|	> 0 if $p_{\mathrm{T}} < 50$ GeV	–	–

Table 8.2: Signal jet definitions for central light jets, central b-jets, and forward jets.

Taus Even though taus are not explicitly searched for in this analysis, they are required to be vetoed in order to remain orthogonal to the 2-lepton search with taus [62] and the 3-lepton [63] analyses. Baseline taus must have $p_{\mathrm{T}} > 20$ GeV, $|\eta| < 2.47$, satisfy loose identification criteria [64], and have either 1 or 3 associated tracks. Signal taus must pass the medium identification criteria [64].

8.2.2 Triggers

There are two trigger steps: event level and object level. The event level stage requires that there are two leptons and that they fall into the allowed p_{T} range in order to trigger the event. At this level the dilepton triggers are required with the offline p_{T} requirement detailed in Table 8.3.

The leptons are then required to each match the dilepton trigger. The choice is based on the relative performance of the trigger matching in data and simulation. The trigger regions

Trigger	L1 Seed	Offline p_{T} Threshold [GeV]
EF_2e12Tvh_loose1	L1_2EM10VH	$p_{\mathrm{T}}(e_1) > 14$, $p_{\mathrm{T}}(e_2) > 14$
EF_e24vh_medium1_e7_medium1	L1_EM18VH	$p_{\mathrm{T}}(e_1) > 25$, $p_{\mathrm{T}}(e_2) > 8$
EF_2mu13	L1_2MU10	$p_{\mathrm{T}}(\mu_1) > 14$, $p_{\mathrm{T}}(\mu_2) > 14$
EF_mu18_tight_mu8_EFFS	L1_MU15	$p_{\mathrm{T}}(\mu_1) > 18$, $p_{\mathrm{T}}(\mu_2) > 8$
EF_e12Tvh_medium1_mu8	L1_EM10VH_MU6	$p_{\mathrm{T}}(e) > 14$, $p_{\mathrm{T}}(\mu) > 8$
EF_mu18_tight_e7_medium1	L1_MU15	$p_{\mathrm{T}}(e) > 8$, $p_{\mathrm{T}}(\mu) > 18$

Table 8.3: The lowest un-prescaled dilepton trigger list including the event filter trigger, the level 1 seed, and the p_{T} threshold for the offline leptons.

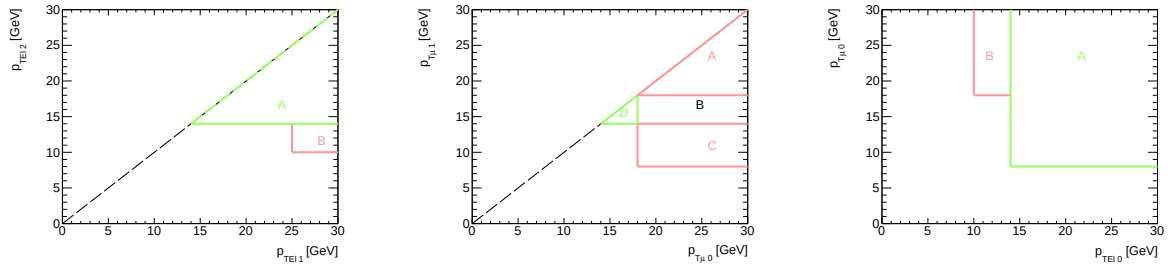

Figure 8.1: The trigger regions in lepton p_{T} space for ee (left) $\mu\mu$ (middle) and $e\mu$ (right). The corresponding trigger is outlined in Table 8.4.

are defined in Table 8.4 and are based on the p_{T} of leading and subleading lepton, as shown in Figure 8.1.

The matching of leptons to trigger objects is only done in data. In simulation, a reweighting scheme is used whereby the efficiency of the trigger as measured in data is applied to simulation to weight the events in order to emulate the application of the trigger. The trigger efficiencies are extracted in events containing a Z boson decay to two leptons using a tag-and-probe method. For electrons, the efficiencies are parameterized as a function of p_{T} and η in order to account for variations seen across the electron energy spectrum and the amount of material it has traversed. For muons, the efficiencies are parameterized as a function of η and ϕ to take into account detector effects. The dependence on energy was found to be negligible compared to the location in the detector. The energy dependence was used to assess a systematic error.

ee channel	
region A	EF_2e12Tvh_loose1
region B	EF_e24vh_medium1_e7_medium1
$\mu\mu$ channel	
region A	EF_mu18_tight_mu8_EFFS
region B	EF_mu18_tight_mu8_EFFS or EF_2mu13
region C	EF_mu18_tight_mu8_EFFS
region D	EF_2mu13
$e\mu$ channel	
region A	EF_e12Tvh_medium1_mu8
region B	EF_mu18_tight_e7_medium1

Table 8.4: Dilepton triggers utilized in the various regions of lepton p_{T} space. The regions are chosen based on the performance of the trigger in data and simulation.

8.3 Standard Model Backgrounds

All signal regions are characterized by the presence of two opposite-charge leptons and $E_{\mathrm{T}}^{\mathrm{miss}}$, for which the SM has many contributing processes such as $t\bar{t}$, single-top, dibosons (WW, WZ and ZZ), and Z/γ^*. There are other sources of reconstructed dilepton signatures from events containing zero or one prompt lepton. For example, W boson produced ($W \to \ell\nu$) in association with a jet can be reconstructed as a dilepton event if a lepton is produced in the hadronization process of the quark. These processes involve *fake* leptons and will be discussed in detail in Subsection 8.3.5.

Given the complexity of the signal regions and the processes considered, a mixture of methods are used to estimate the expected number of background events. For the dominant backgrounds, or where simulation cannot be relied upon, the use of data-driven methods are employed.

The estimates for SR-m_{T2} rely on data-driven techniques for the fake leptons (Subsection 8.3.5), a pure MC estimate for Z/γ^* production, and the use of simultaneously fitting for correction factors for WW, $t\bar{t}$+Wt (collectively called Top), and $ZZ + WZ$ (collectively called ZV), which is described in Subsection 8.3.3. Even though WZ is a three lepton pro-

cess, one lepton could be lost due to detector acceptance and therefore end up contributing to a two lepton final state.

The only difference for SR-Zjets is that Z/γ^* is estimated using a data-driven template method (Subsection 8.3.4) and ZV is estimated from MC. The background sources and the techniques used are summarized in Table 8.5.

Background Source	SR-m_{T2}	SR-Zjets
Fake Leptons	Matrix Method	Matrix Method
Top	Simultaneous Fit	Simultaneous Fit
WW	Simultaneous Fit	Simultaneous Fit
ZV	Simultaneous Fit	MC
Z/γ^*	MC	Template Method

Table 8.5: Summary of the background techniques used to estimate the contributions from each process in the two signal regions.

8.3.1 Monte Carlo Samples

Each background estimate relies on Monte Carlo simulation for either the central value, as a cross check against the data-driven estimate, or as input into a data-driven technique. For this reason, much care has gone into selecting generators and showering software to produce the most reliable estimate in a variety of control regions.

Top Top-quark pair production is simulated at next-to-leading order (NLO) PDF set `CT10` [65] with `MC@NLO` [42, 43, 44]. Systematic variations are evaluated by comparing the results of this generator with those of `POWHEG` [66] plus `PYTHIA` and `ALPGEN` [48] plus `HERWIG` [46]. Single top s-channel production is modeled with `MC@NLO` using NLO PDF set `CT10` for Wt, while the t-channel process is modeled with `ACER` [67]. Production of $t\bar{t}$ with an additional boson (W or Z) is simulated with the leading-order (LO) generator `Madgraph` [47] and scaled to the NLO cross-section [68, 69, 70].

Diboson and Triboson Diboson samples for this analysis simulated for WW, WZ, and ZZ with POWHEG using the NLO PDF set CT10, with additional contributions from the gluon-gluon fusion which is simulated with gg2WW [71] and gg2ZZ [72]. Samples generated with aMC@NLO [73] are used to assess systematic uncertainties at the generated particle level.

The triboson samples contribute very little to the signal regions due to the low cross-section and kinematic selection, however they are taken into account. Madgraph is used to simulate WWW, ZWW, and ZZZ production that result in a dilepton final state.

V+jet Processes involving W or Z produced in association with a jet are simulated using a combination of ALPGEN and SHERPA [74] using the PDF set CTEQ6L1 [75] and CT10 respectively. The samples involving a Z boson are directly used for the signal region SR-m_{T2}, while they only serve as a cross-check to the template method for SR-Zjets. The samples involving a W boson are used as input to the matrix method, as $W(\rightarrow \ell\nu)$ + jet constitutes one of the dominant processes that give fake leptons.

Higgs Higgs decays leading to a dilepton final state are also considered. Gluon and vector boson fusion production modes are simulated with POWHEG using the PDF set CT10 with a Higgs mass of 125 GeV. Diboson production involving a Higgs and a W or Z is simulated using PYTHIA.

QCD Heavy flavor $b\bar{b}$ and $c\bar{c}$ are simulated with PYTHIA. These samples contribute very little to the signal regions, however they are necessary as inputs to the matrix method (8.3.5).

8.3.2 Monte Carlo Systematic Uncertainties

The dominant uncertainty arising from the simulated samples is attributed to the choice of generator and the subsequent modeling of difficult kinematic variables used to define the signal regions. For top events, POWHEG plus JIMMY is the nominal generator and is compared with MC@NLO in order to assess a systematic uncertainty. In addition, an uncertainty based on the amount of initial and final state radiation is estimated by comparing AcerMC with PYTHIA, which is summarized in Table 8.6. POWHEG plus HERWIG is compared with POWHEG plus PYTHIA for WW events. The uncertainty on ZV is obtained by comparing POWHEG plus PYTHIA to SHERPA. The generator uncertainties are signal region dependent, and can be found in Table 8.7.

Process	SR-m_{T2},90 [%]	SR-m_{T2},120 [%]	SR-m_{T2},150 [%]	SR-Zjets [%]
Top	8 ± 8	6 ± 13	0 ± 34	12 ± 8

Table 8.6: The uncertainty associated with the amount of initial and final state radiation in $t\bar{t}$ for each signal region considered.

Process	SR-m_{T2},90 [%]	SR-m_{T2},120 [%]	SR-m_{T2},150 [%]	SR-Zjets [%]
Top	13 ± 19	15 ± 21	14 ± 42	10 ± 17
WW	18 ± 3	34 ± 5	43 ± 8	80 ± 33
ZV	12 ± 5	30 ± 14	17 ± 12	55 ± 21

Table 8.7: The uncertainty associated with the choice of generator for backgrounds estimated from simulated processes in the signal regions considered in this dissertation.

The dominant experimental systematic uncertainty is attributed to the jet energy scale [29, 31, 76, 30, 77, 78] and resolution [79]. A p_{T} and η scale factor is used to modify the energy of the jets in each event, which accounts for uncertainties due to pile up, nearby jets, and origin corrections. The typical size of the uncertainty for the jets are 0.5%-3.0% [31]. The resolution systematic uncertainty is calculated by smearing each jet according to a Gaussian distribution with a mean and width given by a p_{T}-dependent function. The scale of the resolution uncertainty ranges from 10%-20% [79]. In addition, a systematic uncertainty

for identifying b-jets is included [80].

The remaining uncertainties are relatively small in comparison. A 2.8% uncertainty is attributed to the luminosity measurement. The energy scale and resolution uncertainty associated for leptons as well as the identification efficiency [41, 49, 81, 50] amount to a few percent each, and contribute negligibly in the signal regions. Uncertainty on the missing energy is estimated by propagating all of the systematic shifts on the energy of the leptons and jets to the missing energy. In addition, an uncertainty on the resolution and scale of the energy deposits not assigned to any reconstructed objects is included. Finally, an uncertainty associated with the limited MC statistics is evaluated for each signal and control region.

These errors are combined taking into account any correlations. The final uncertainties for each signal region can be found in Table 8.8.

	SR-m_{T2},90		SR-m_{T2},120		SR-m_{T2},150		SR-Zjets
Process	$ee+\mu\mu$ [%]	$e\mu$ [%]	$ee+\mu\mu$ [%]	$e\mu$ [%]	$ee+\mu\mu$ [%]	$e\mu$ [%]	$ee+\mu\mu$ [%]
MC statistics	5	7	7	12	10	23	14
Jet	4	1	2	1	5	7	11
Lepton	1	2	1	1	2	8	4
Soft term	3	4	1	1	2	8	5
b-tagging	1	2	< 0	< 0	< 0	< 0	2
Luminosity	< 0	< 0	< 0	< 0	< 0	< 0	2
Theory and modeling	11	13	21	31	18	40	42
Total	13	16	24	34	23	47	42

Table 8.8: The final uncertainties in the signal regions from each source of uncertainty on the simulated background given as a percentage.

8.3.3 MC Validation

The strict signal region requirements on sophisticated search variables requires validation of the simulated backgrounds. Dedicated control regions for WW, ZV, and Top have been developed where these individual processes dominate in order to obtain a data driven correction factor. The control regions are defined to be as close to the signal region as possible but

also remain orthogonal. The desired number of events from a particular background source N_B^{SR} ($B = WW$,Top, ZV) in the signal region is given by,

$$N_B^{SR} = \frac{N_{data}^{CR} - N_{non-B,MC}^{CR}}{N_{B,MC}^{CR}} \times N_{B,MC}^{SR}, \tag{8.1}$$

where $N_{B,MC}^{CR}$ ($N_{non-B,MC}^{CR}$) is the number of events from simulation in the control region for process B (contamination) and $N_{B,MC}^{SR}$ is the number of simulated events from process B in the signal region. The "scale factor" is defined as $\frac{N_{data}^{CR} - N_{non-B,MC}^{CR}}{N_{B,MC}^{CR}}$, which will be unity if the number of simulated events correctly predicts process B in the control region.

For each control region, the background estimate is computed from simulation for WW, ZV, Top, Z+jets, and SM Higgs, while the fake is taken from the data-driven matrix method described in Section 8.3.5. Then a simultaneous likelihood fit [82] is performed to obtain a normalization for the process that the control region is targeting. The event yields are treated with a Poisson probability density function (PDF) and the systematic uncertainties on the expected yield are included as nuisance parameters that are constrained to be Gaussian with a width determined by the magnitude of the uncertainty. A set of these PDFs is made for each process (WW, Top, and ZV for SR-m_{T2} and Top for SR-Zjets) and is used to construct a likelihood function by taking the product of the PDFs. The likelihood is then maximized by adjusting the free parameters and the nuisance parameters. The free parameters are then used to adjust the background estimate from the source that the control region is targetting.

Validation in SR-m_{T2} The simultaneous fit for SR-m_{T2} is performed for WW, ZV, and Top in the control regions defined in Table 8.9. The WW control region is obtained by requiring $50 < m_{\mathrm{T2}} < 90$ GeV, which is orthogonal to the signal region. The fit is performed in the $e^{\pm}\mu^{\mp}$ channel only due to the contamination from Z/γ^*+jets found in the $e^{\pm}e^{\mp}$ and $\mu^{\pm}\mu^{\mp}$ channel. The dominant contamination in WW control region is from processes involving the top quark and is found to be 12%. Contamination from the SUSY processes

considered is less than 10%. The scale factor is found to be 1.14 ± 0.04, where the error includes the statistical uncertainties.

The scale factor for $t\bar{t}$ and Wt production is evaluated in the same control region by requiring $m_{\mathrm{T2}} > 70$ GeV and including at least one central b-tagged jet. Only the $e^{\pm}\mu^{\mp}$ channel is used, and the contamination is found to be around 1% from SM sources, and negligible for any SUSY signal points considered. The scale factor is found to be consistent with unity at 1.02 ± 0.02, where the error includes the statistical uncertainties.

The ZV background is estimated from the same flavor channels by requiring the dilepton mass to be consistent with the Z boson and $m_{\mathrm{T2}} > 90$ GeV. Contamination from WW is the largest (4.5%). The contamination from SUSY is found to be less than 5%. The scale factor is 1.08 ± 0.10, where the error includes the statistical uncertainties.

Validation in SR-Zjets The simultaneous fit for SR-Zjets is performed for Top only, while WW and ZV are taken directly from simulation. The contribution from WW is found to be negligible after requiring the dilepton mass to be consistent with Z boson. A control region that is dominated by ZV with minimal contamination and close to the signal region was not found, therefore the central value is taken from simulation with no adjustment. The background from WZ and ZZ are validated in separate control regions requiring three and four leptons respectively. Good agreement is found in these control regions, and a conservative 20% systematic uncertainty is applied to cover the variations seen.

The Top control region requires opposite flavor leptons, reversal of the Z veto, and at least one central b-tagged jet, thus remaining orthogonal to the signal region. The contamination from non-Top processes is around 1% or less, and the contamination from SUSY processes considered in this analysis is found to be less than 1%. The scale factor for Top is 0.99 ± 0.06, where the error includes the statistical uncertainties.

	Control Region for SR-m_{T2},90,120,150
Charge	Opposite-sign
$p_T^{\ell 1}$	>35 GeV
$p_T^{\ell 2}$	>20 GeV
$m_{\ell\ell}$	>20 GeV
CR-WW	
Lepton Flavor	eμ
N_{B20}	=0
N_{L20}	=0
N_{F30}	=0
m_{T2}	[50,90] GeV
CR-Top	
Lepton Flavor	eμ
N_{B20}	$\geq$1
N_{L20}	=0
N_{F30}	=0
m_{T2}	>70 GeV
CR-ZV	
Lepton Flavor	ee,$\mu\mu$
N_{B20}	=0
N_{L20}	=0
N_{F30}	=0
m_{T2}	>90 GeV

Table 8.9: Definition of control regions for jet-veto signal region SR-m_{T2}.

	Control Region for SR-Zjets
Charge	Opposite-sign
Lepton Flavor	Same Flavor
$p_T^{\ell 1}$	>35 GeV
$p_T^{\ell 2}$	>20 GeV
CR-Top	
$m_{\ell\ell}$	$\lvert m_{\ell\ell} - m_Z\rvert$ >10 GeV
N_{L20}	—
N_{B20}	$\geq$1
N_{F30}	=0
$\Delta R_{\ell\ell}$	[0.3,1.5]
$E_T^{miss,rel}$	>80 GeV
$p_{T,\ell\ell}$	>80 GeV

Table 8.10: Definition of control regions for SR-Zjets.

8.3.4 Z+jet Template Method

The Z+jet template method is used to estimate the contribution from Z boson production in association with a jet in the high relative missing energy region. This background falls off sharply as a function of $E_{\mathrm{T}}^{\mathrm{miss,rel}}$, as shown in Figure 8.2. The small contribution from this background source to the signal region cannot be reliably estimated from simulation due to the lack of statistics in the MC sample and the poor modeling of missing energy in simulated $Z \to \ell\ell$ events with hadronic jets, which is why this high statistics data driven method has been incorporated to this analysis. A data driven approach based on the "jet smearing" method described in [83, 84] is used to estimate this background.

Origin of Fake $E_{\mathrm{T}}^{\mathrm{miss}}$ The dominant source of missing energy in Z+jet events comes from mismeasured physics objects and detector effects. Jets are obvious candidates to attribute the inaccurate momentum measurement given the complexity of the object itself. With a fixed cone size at $R = 0.4$, it is possible for tracks associated with the hadronization of the quark to migrate outside the cone. It is also possible for tracks not associated with the hadronization process (ie. tracks from pileup) to become a part of the jet. This type of activity will lead to a momentum imbalance in the event, thus creating $E_{\mathrm{T}}^{\mathrm{miss}}$ where there is none.

In addition to the contributions from jets, there are soft objects and unclustered calorimeter energy deposits in the event that are not identified as electrons, muons, photons, or jets that can contribute to the overall energy of the event, and can create a momentum imbalance leading to fake $E_{\mathrm{T}}^{\mathrm{miss}}$. These are collectively the "soft terms", and are the final piece incorporated into the $E_{\mathrm{T}}^{\mathrm{miss}}$, as explained in Section 5.5.

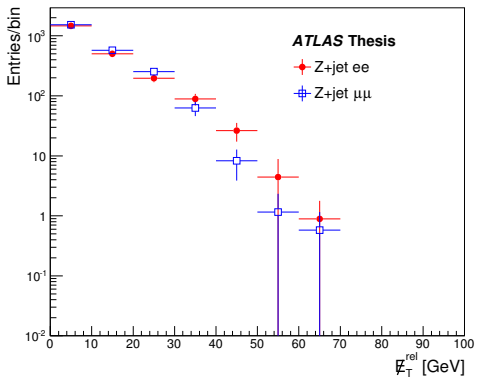

Figure 8.2: The $E_{\mathrm{T}}^{\mathrm{miss,rel}}$ distribution from simulated Z+jet events for ee and $\mu\mu$ for SR-Zjets selection (Table 8.20) prior to the $E_{\mathrm{T}}^{\mathrm{miss,rel}}$ requirement. The distribution falls off sharply and is limited by statistics.

Method Overview The method aims to take well measured Z+jet events and smear the jet and soft term components of the missing energy using templates. This will introduce momentum imbalance artificially in order to generate fake $E_{\mathrm{T}}^{\mathrm{miss}}$ into these events.

A template for the jet smearing is constructed by looking at the resolution in the measured response (R),

$$R = \frac{p_{\mathrm{T}}^{reco}}{p_{\mathrm{T}}^{true}}, \tag{8.2}$$

where "reco" is the reconstructed p_{T}, and "true" is the true particle jet p_{T} [84]. The response is measured in control regions containing two or three jets in simulated events and then corrected by observations in data. This measurement is done in bins of p_{T} for the jet, as shown in Figure 8.3 for the entire p_{T} spectrum as well as the projection for a particular bin in jet p_{T} ($40 < p_{\mathrm{T}}^{jet} < 60$ GeV).

The magnitude of the soft term used in the $E_{\mathrm{T}}^{\mathrm{miss}}$ calculation is smeared and the direction is left fixed. At the analysis level, the individual components used to calculate the soft term is not available, therefore an overall adjustment to the collection of objects is made. This is done by parameterizing the vector sum of the soft objects ($E_T^{softterm}$) as a function of the

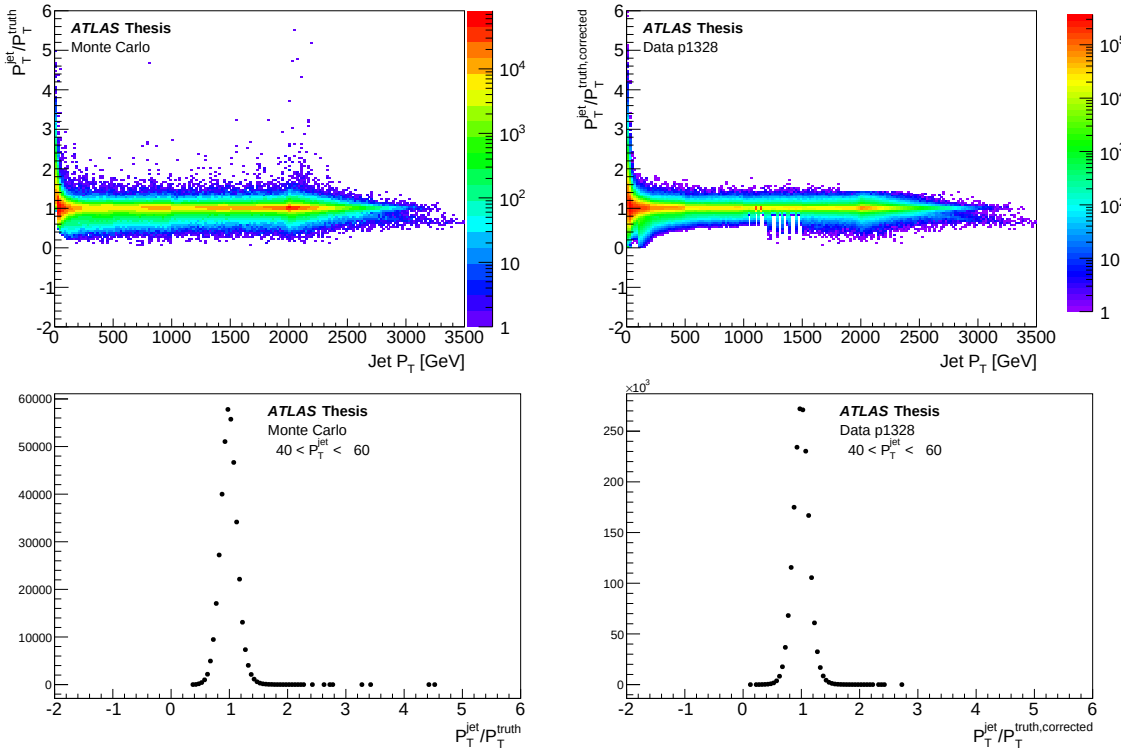

Figure 8.3: This figure includes the response as a function of p_{T}^{jet} (upper two) and the response for a specific bin in p_{T}^{jet} (lower two).

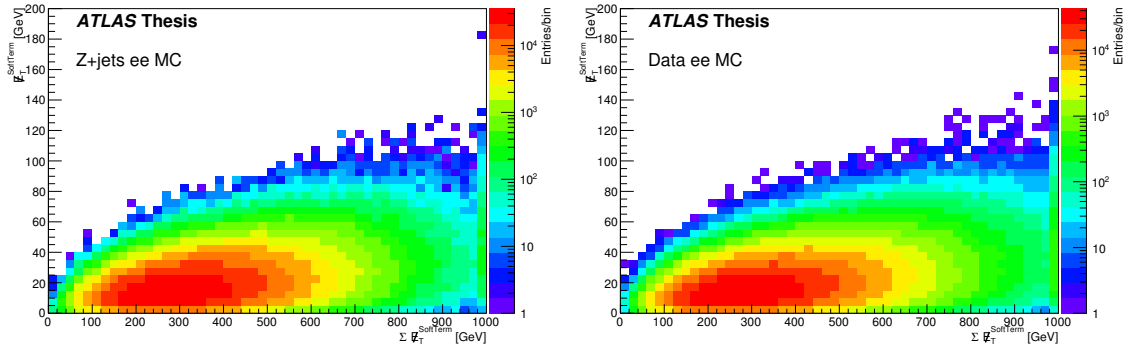

Figure 8.4: The response function for the soft term of the $E_{\mathrm{T}}^{\mathrm{miss}}$ that has been parameterized as a function of $\sum E_T^{softterm}$.

scalar sum of the soft objects ($\sum E_T^{softterm}$), as illustrated in Figure 8.4. The distributions in Figure 8.4 are measured in a dilepton control region by requiring $|m(\ell\ell) - m(Z)| < 10$ GeV and a veto for the three jet categories outlined in Subsection 8.2.1.

The responses derived in data (MC) are applied to data (MC) events. The same soft term response is used for both ee and $\mu\mu$ channels given minimal differences observed in the overall shape.

The application of the jet and soft term smearing is used to rebuild the $E_{\mathrm{T}}^{\mathrm{miss}}$ for a given event introducing the shifted energy of the objects following Equation 8.3:

$$E_{x,y}^{miss,smeared} = E_{x,y}^{miss} - \sum_{Jets} p_{x,y} + \sum_{SmearedJets} p_{x,y} + \Delta E_{x,y}^{SoftTerm} \tag{8.3}$$

Essentially, one takes the originally computed $E_{\mathrm{T}}^{\mathrm{miss}}$ and remove the original jets. Then, the jets are smeared and reintroduced into the $E_{\mathrm{T}}^{\mathrm{miss}}$. Additionally, the magnitude of the soft term is adjusted based on the value for $E_T^{softterm}$ chosen from the response function.

Seed Region Events that are to be smeared are selected from the "seed" region. These events are selected to contain well balanced calorimeter activity so that the smearing functions shown in Figure 8.3 and Figure 8.4 are applicable. Each seed event can be used N

times, which yields a high statistic sample thus taking care of the initial problem found with the simulated statistics.

The seed region is chosen in order to be orthogonal to the signal region by reversing the requirement on $E_{\mathrm{T}}^{\mathrm{miss,rel}}$, as well as introducing a requirement which will insure well measured calorimeter activity. A cut on $E_T^{miss,significance}$ is placed at 1.5 GeV^{-1}, where $E_T^{miss,significance}$ is defined as,

$$E_T^{miss,significance} = \frac{E_{\mathrm{T}}^{\mathrm{miss}}}{\sum(E_T^{jet} + E_T^{softterm})}, \tag{8.4}$$

where the numerator is the total $E_{\mathrm{T}}^{\mathrm{miss}}$ in the system and the denominator is the $\sum E_T$ for the jet and soft term [84].

Each signal or validation region where one wants to use the template method will require a dedicated seed region. For this analysis, there are two regions where the method is needed: the signal region (SR-Zjets) and a validation region where the prediction can be checked. These regions and their corresponding seed regions are given in Table 8.11.

Choosing Seed Region The requirement on $E_T^{miss,significance}$ is what defines the seed region, and there is no a priori way of choosing where to place the requirement. In order to decide where this cut should be placed for data, a study of simulated Z+jet events is carried out to determine which requirement will give the best agreement as a function of the variable that will define the signal region. For this analysis, $E_{\mathrm{T}}^{\mathrm{miss,rel}}$ is the defining variable, so the $E_T^{miss,significance}$ requirement is chosen such that the $E_{\mathrm{T}}^{\mathrm{miss,rel}}$ distribution is adequately reproduced.

The solid black distributions in Figure 8.5 show the prediction from Z+jet MC for both signal and validation regions prior to any $E_{\mathrm{T}}^{\mathrm{miss,rel}}$ requirement. The various colored points on the figures show the result of the smearing procedure after using different $E_T^{miss,significance}$

Region	SR-Zjets	SR-Zjets Seed	Validation	Validation Seed
$p_T^{\ell 1} >$ [GeV]	35			
$p_T^{\ell 2} >$ [GeV]	20			
charge	OS			
flavor	same flavor			
$\lvert m_{\ell\ell} - m_Z \rvert$	< 10			
central light jets	$>= 2$			
signal b-jets	$= 0$			
signal forward jets	$= 0$			
$p_T^{\mathrm{j}1} >$ [GeV]	45			
$p_T^{\mathrm{j}2} >$ [GeV]	45			
$p_{T,ll}$ [GeV]	> 80		< 80	
$\lvert \Delta R \ell\ell \rvert$	$[0.3, 1.5]$		–	
$m_{\mathrm{j}1,\mathrm{j}2}$ [GeV]	$[50, 100]$		–	
$E_{\mathrm{T}}^{\mathrm{miss,rel}}$ [GeV]	> 80	< 80	> 40	< 40
$E_T^{miss,significance}$ [GeV$^{-1/2}$]	–	< 1.5	–	< 1.5

Table 8.11: The definition of SR-Zjets and the validation region along with the corresponding seed regions.

cut values in order to define the seed region. The ratio plot illustrates how well the various seed regions reproduce the expected distribution. From these figures, a cut value of 1.5 on $E_T^{miss,significance}$ is chosen for both the signal and validation seed regions based on the agreement observed in the ratio plot. This will now define the seed region that will be used in data.

Validation Region Results In order to assess how well the template method reproduces the shape and yield, a validation region is constructed where Z+jet is the dominant background. This region is defined in Table 8.11. The selection mirrors the signal region, except that several requirements are dropped to gain statistics, as well as the $p_{\mathrm{T}}(\ell\ell)$ requirement is reversed to remain orthogonal to the signal region.

A comparison between the template method applied to data and simulated Z+jet events can be seen in Figure 8.6. The overall shape in the bulk of the distribution is reproduced quite well by the template method and the tails of the distribution have been extended. Table 8.12

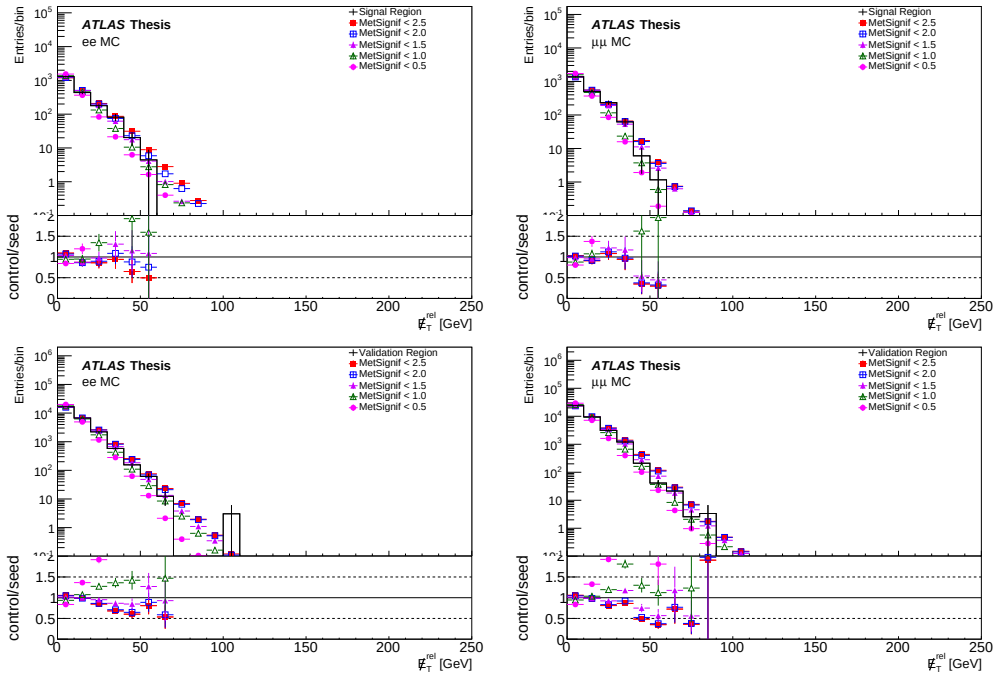

Figure 8.5: The distributions for $E_{\mathrm{T}}^{\mathrm{miss,rel}}$ for signal region (top) and the validation region (bottom). The solid black distribution is the MC prediction, and the colored markers are the prediction from the template applied to MC for various seed region definitions. The difference between each seed region is the requirement on $E_T^{miss,significance}$, which is given in the legend.

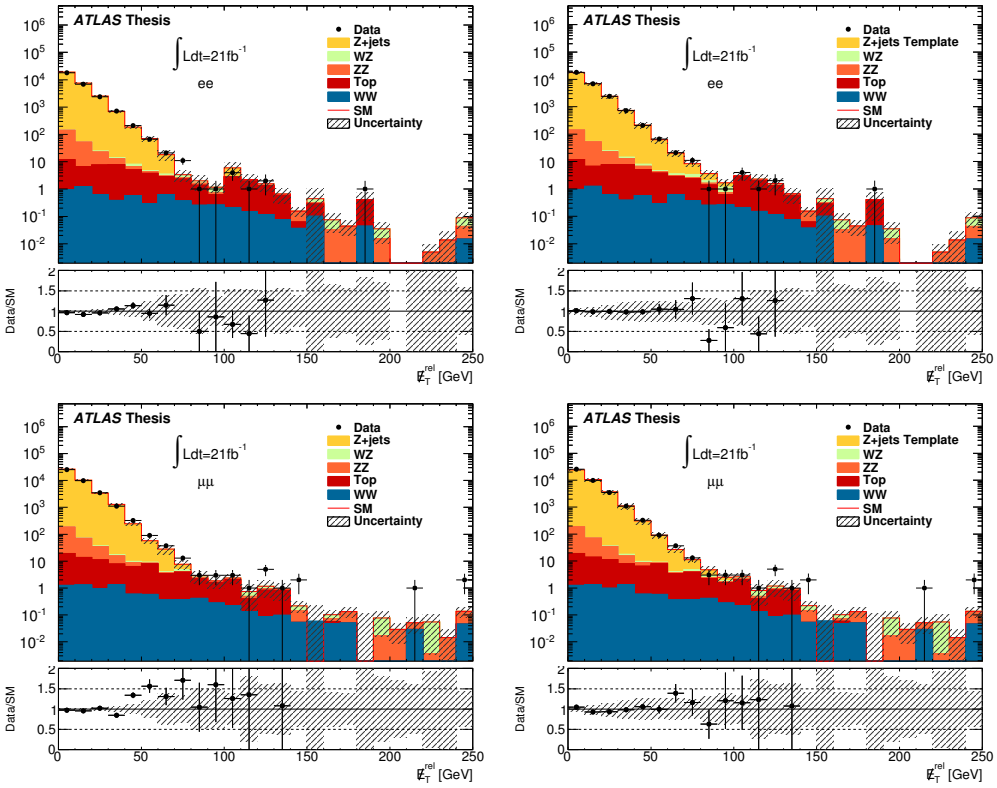

Figure 8.6: The results in the validation region using Z+jet MC (left) and the template method applied to data (right) for both ee (top) and $\mu\mu$ (bottom). The errors included are the statistical from all MC samples considered as well as the statistical and systematic errors from the template method.

gives the yield for two regions in $E_{\mathrm{T}}^{\mathrm{miss,rel}}$, and good agreement is observed in both.

Signal Region Results Similar to the validation region results presented previously, the shape and yield of the template distributions are presented. Figure 8.7 shows the gains of using the template method by comparing side-by-side the predictions from MC and the template method. Stability in the bulk of the $E_{\mathrm{T}}^{\mathrm{miss,rel}}$distribution is achieved, and the tails are extended. Table 8.13 shows the agreement in two bins of $E_{\mathrm{T}}^{\mathrm{miss,rel}}$ where the good agreement prior to the signal region cut can be seen.

Systematic Errors There are three sources of systematic uncertainty that are considered.

	$40 < E_{\mathrm{T}}^{\mathrm{miss,rel}} < 80$									$80 < E_{\mathrm{T}}^{\mathrm{miss,rel}}$								
Process	ee	(stat)	(sys)	$\mu\mu$	(stat)	(sys)	ee+$\mu\mu$	(stat)	(sys)	ee	(stat)	(sys)	$\mu\mu$	(stat)	(sys)	ee+$\mu\mu$	(stat)	(sys)
Z+jets Template	286.066	2.673	$^{+53.044}_{-54.884}$	412.999	3.483	$^{+83.935}_{-80.317}$	699.065	4.391	$^{+99.629}_{-97.502}$	2.345	0.037	$^{+0.211}_{-0.609}$	2.812	0.057	$^{+0.638}_{-0.526}$	5.158	0.068	$^{+0.809}_{-0.857}$
WZ	3.282	0.471		3.349	0.438		6.631	0.643		1.445	0.307		1.680	0.312		3.125	0.438	
ZZ	2.848	0.700		3.539	0.694		6.388	0.986		0.917	0.119		1.202	0.134		2.119	0.179	
Top	13.293	3.209		21.429	3.528		34.722	4.769		8.182	2.202		6.112	2.164		14.294	3.088	
WW	2.127	0.331		2.304	0.280		4.431	0.434		1.268	0.275		1.504	0.230		2.772	0.359	
Total SM	307.62	4.27	$^{+53.04}_{-54.88}$	443.62	5.03	$^{+83.93}_{-80.32}$	751.24	6.60	$^{+99.63}_{-97.50}$	14.16	2.24	$^{+0.21}_{-0.61}$	13.31	2.20	$^{+0.64}_{-0.53}$	27.47	3.14	$^{+0.81}_{-0.86}$
Observed	308			471			779			10			21			31		

Table 8.12: Data and SM comparison for validation region in two bins of $E_{\mathrm{T}}^{\mathrm{miss,rel}}$. The first is $40 < E_{\mathrm{T}}^{\mathrm{miss,rel}} < 80$ GeV and second is $E_{\mathrm{T}}^{\mathrm{miss,rel}} > 80$ GeV. These two met bins are split at 80 GeV to mimic the signal region. Overall good agreement is observed. The region $E_{\mathrm{T}}^{\mathrm{miss,rel}} < 40$ is not shown given that this is the normalization region and agrees by definition.

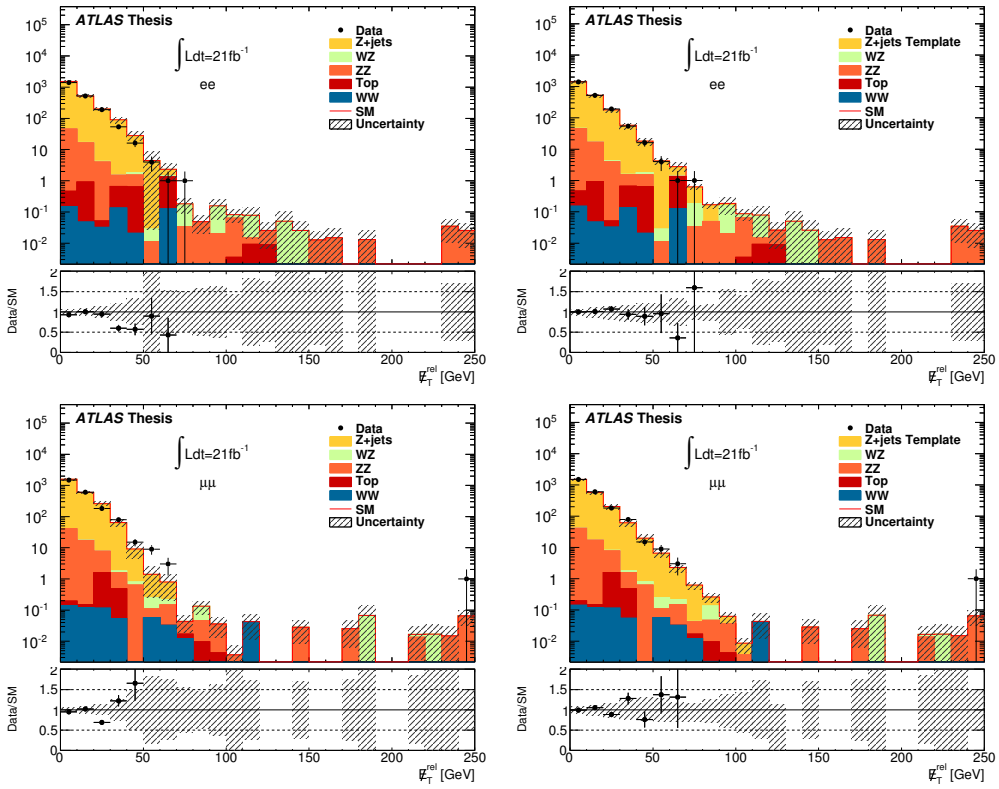

Figure 8.7: The results in the signal region prior to the $E_{\mathrm{T}}^{\mathrm{miss,rel}}$ requirement using Z+jet MC (left) and the template method applied to data (right) for both ee (top) and $\mu\mu$ (bottom). The errors included are the statistical from all MC samples considered as well as the statistical and systematic errors from the template method. The data in the signal region has been blinded.

	$40 < E_{\mathrm{T}}^{\mathrm{miss,rel}} < 80$									$80 < E_{\mathrm{T}}^{\mathrm{miss,rel}}$								
Process	ee	(stat)	(sys)	$\mu\mu$	(stat)	(sys)	ee+$\mu\mu$	(stat)	(sys)	ee	(stat)	(sys)	$\mu\mu$	(stat)	(sys)	ee+$\mu\mu$	(stat)	(sys)
Z+jets Template	22.164	0.963	$^{+3.598}_{-4.420}$	27.969	1.087	$^{+6.038}_{-5.330}$	50.133	1.452	$^{+7.037}_{-6.929}$	0.152	0.007	$^{+0.005}_{-0.022}$	0.161	0.018	$^{+0.010}_{-0.056}$	0.313	0.019	$^{+0.013}_{-0.060}$
WZ	0.511	0.199		0.462	0.149		0.973	0.249		0.296	0.131		0.174	0.088		0.470	0.158	
ZZ	1.014	0.496		0.860	0.331		1.874	0.596		0.255	0.062		0.219	0.059		0.474	0.086	
Top	1.828	0.987		0.012	0.009		1.839	0.987		0.022	0.013		0.011	0.008		0.034	0.016	
WW	0.146	0.091		0.104	0.050		0.250	0.104		0.000	0.000		0.045	0.031		0.045	0.031	
Total SM	25.66	1.48	$^{+3.60}_{-4.42}$	29.41	1.15	$^{+6.04}_{-5.33}$	55.07	1.87	$^{+7.04}_{-6.93}$	0.72	0.15	$^{+0.01}_{-0.02}$	0.61	0.11	$^{+0.01}_{-0.06}$	1.34	0.18	$^{+0.01}_{-0.06}$
Observed	22			27			49			0			1			1		

Table 8.13: Data and SM comparison for SR-Zjets in two bins of $E_{\mathrm{T}}^{\mathrm{miss,rel}}$. The first is prior to the signal region requirement ($E_{\mathrm{T}}^{\mathrm{miss,rel}} > 80$ GeV) and second is in the signal region. The data have been blinded for the SR. Overall good agreement is observed. The region $E_{\mathrm{T}}^{\mathrm{miss,rel}} < 40$ is not shown given that this is the normalization region and agrees by definition.

1. **Statistical Uncertainty of seed events**

   Given that a seed event is used an infinite amount of times, the statistical error for that event is correlated among bins. This is taken into account by assuming that one has N_i seed events in the i-th bin of a variable x that have been smeared M times, which can be represented as

   $$N_i = \frac{1}{M} \sum_j n_{ij} \tag{8.5}$$

   where the j-th bin is representative of the smeared distribution. The error on the j-th bin is given as

   $$\Delta N_j(x) = \sqrt{M \times \sum_i \frac{n_{ij}^2}{\sum_j n_{ij}}}. \tag{8.6}$$

   The relative statistical error from the seed events is sufficiently small to be ignored given that for one seed event, an infinite number of pseudo-data events can be generated. For this analysis, each seed event is used 10k times.

2. **Systematic uncertainty from tail fluctuations**

   The uncertainty associated to fluctuations in the tails of the jet resolution function is determined from a fitted response function for the jet. In order to take into account

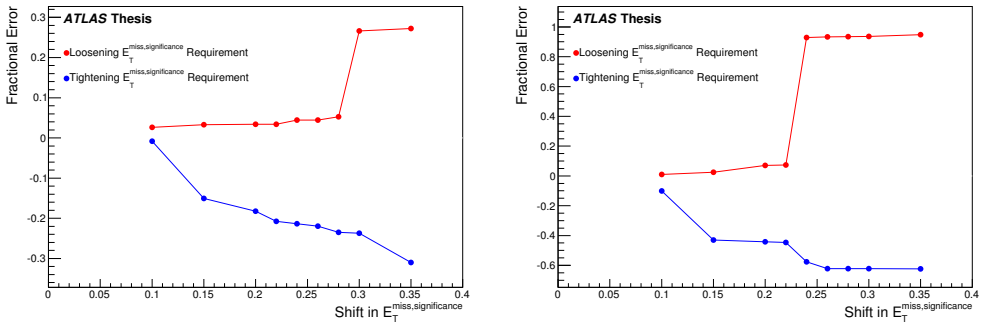

Figure 8.8: The relative systematic uncertainty as a function of the met significance variation from the nominal value of 1.5 $\text{GeV}^{1/2}$.

tail fluctuations, which have the largest impact at high $E_{\text{T}}^{\text{miss}}$, systematic shifts on these fitted responses are propagated through to the missing energy distributions.

3. $E_T^{miss,significance}$ **cut choice**

It was found that varying the cut on missing energy significance can alter the overall prediction of the method. The variations are attributed to introducing biases in the $E_{\text{T}}^{\text{miss}}$ distribution for the seed events. Cutting too tight on $E_T^{miss,significance}$ will restrict the initial $E_{\text{T}}^{\text{miss}}$ distribution to lower values and therefore makes it difficult to fill in the high $E_{\text{T}}^{\text{miss}}$ tails. Cutting too loose on $E_T^{miss,significance}$ will allow contamination from other processes, as well as contamination from mismeasured Z+jet events. A systematic uncertainty is assessed by varying the cut on $E_T^{miss,significance}$ from the nominal 1.5 $\text{GeV}^{1/2}$ by ± 0.2 $\text{GeV}^{1/2}$. This follows from a study of the impact on the signal region by varying the cut threshold and computing the relative error, as seen in Figure 8.8. It is determined that a shift of 0.2 $\text{GeV}^{1/2}$ yields sufficient uncertainty while not biasing the uncertainty with a requirement that is too tight.

8.3.5 Fake Lepton Background

The Matrix Method (MM) used in this analysis follows from that described in Subsection 7.3.5 with several updates to address the needs for this analysis. The procedure utilizes

the system of equations expressed as a matrix given in Equation 7.4, but the new approach includes an updated method for deriving the real efficiency and fake rates which populate the matrix elements.

In addition to the updates on the derivation of the efficiencies and rates, the definitions of "tight" and "loose" leptons are also modified to fit the lepton selection for this analysis. Signal leptons satisfy the tight criteria, while baseline leptons pass a looser criteria. For muons, this means dropping the isolation requirement, and for electrons we loosen the identification criteria from tight++ to medium++ and we drop the isolation. For both electron and muon, $|d_0^{\mathrm{PV}}/\sigma_{d_0^{\mathrm{PV}}}|$ and $|z_0^{\mathrm{PV}} \times \sin(\theta)|$ are also not applied.

Unlike the implementation of this method in Subsection 7.3.5, this analysis requires exactly two baseline leptons. This implies that there will never be a case of having more than two loose leptons in the event, so cycling through the tight-loose permutations is not necessary.

Weighted Average Fake Rate and Real Efficiency This method utilizes the weighted average fake rate and real efficiency as inputs to the matrix method described previously. This is a sophisticated procedure where one tries to take into account the difference in the fake rate from various sources (eg. $t\bar{t}$ vs. W+jet) and the type of process producing fake leptons, for example fake leptons from converted photon as compared with those originating from the semi-leptonic decay of a b-quark. Each signal region will receive a unique fake rate and real efficiency which represents the combination of the previously mentioned factors. This detailed information about the sources and the fake type are extracted from simulation. For a lepton flavor ℓ and region X the fake rate is expressed as,

$$f_X^\ell = \sum_{i,P} (sf^i \times R_P^i \times f^i), \tag{8.7}$$

where the summation over i denotes the type of fake (jet fake or conversion) and P denotes the process contributing fake leptons (eg. $t\bar{t}$). The individual inputs into Equation 8.7 are:

- $\boldsymbol{sf^i}$ is the scale factor for the type of fake i which accounts for differences between data and simulation as measured in dedicated control regions.
- $\boldsymbol{R^i_P}$ represents is the fraction of fake type i for process P. This quantity will give the relative percentage to weight the rate from a specific process in a specific region.
- $\boldsymbol{f^i}$ is the probability for a lepton originating from process i to pass the tight selection criteria. This rate is measured in MC for each process utilizing the generator information and is parameterized as a function of p_{T}.

These factors all are combined to construct a fake rate for electrons and muons separately for each region where the prediction is needed, which is motivated by the fact that the fake rates for different processes can be quite different, as seen in Figure 8.9. One caveat is that the contribution from muon conversions is negligible and ignored. This results in the summation over i being dropped in Equation 8.7.

The real efficiency is handled in the same way as the fake rate, with the modification to Equation 8.7 to remove the summation over i,

$$r^{\ell}_X = \sum_P (sf^i \times R_P \times r). \tag{8.8}$$

The $\boldsymbol{sf}$, $\boldsymbol{R_P}$, and $\boldsymbol{r}$ hold the same meaning as they did for Equation 8.7, except in the case of the real efficiency r is substituted for f.

Monte Carlo Rates and Efficiencies The fake rates and real efficiencies are derived in MC by requiring exactly two baseline leptons and requiring $E_{\mathrm{T}}^{\mathrm{miss}} > 20$ GeV. Each lepton is then put into three categories:

1. **Real Lepton:** Real leptons are leptons from the decay of W, Z, or from the leptonic decay of a τ lepton. All leptons from sparticle decays are also classified as real.

2. **Jet Fake:** These are either jets that have been mis-identified as leptons or leptons from non-isolated sources, such as the semi-leptonic decay of b-quark.

3. **Conversion Fake:** These are leptons that are produced form converted photons.

After sorting into each category, the fake rate or real efficiency is constructed by checking whether or not the baseline lepton satisfies the signal lepton requirements,

$$r(p_{\mathrm{T}}), f(p_{\mathrm{T}}) = \frac{N(p_{\mathrm{T}})^{signal}}{N(p_{\mathrm{T}})^{baseline}}. \tag{8.9}$$

This is measured for each process that contributes real and fake leptons to the dilepton channel. The MC fake rates (real efficiencies) can be found in Figure 8.9 (Figure 8.10), which represent the inputs into Equation 8.7 (Equation 8.8).

Scale Factors The purpose of the scale factor is to correct the rates and efficiencies extracted from simulation for what is observed in data. This is a necessary step given that these rates will be applied to data in order to extract the final estimate. The scale factors are measured in dedicated control regions for real leptons, jet fakes, and conversions, which will then be applied to the appropriate rate or efficiency.

The real control region utilizes a Z boson tag-and-probe and requires:

1. Exactly two baseline leptons of the same flavor

2. At least one lepton must be a signal lepton (tag)

3. $|m(\ell\ell) - m(Z)| < 10$ GeV

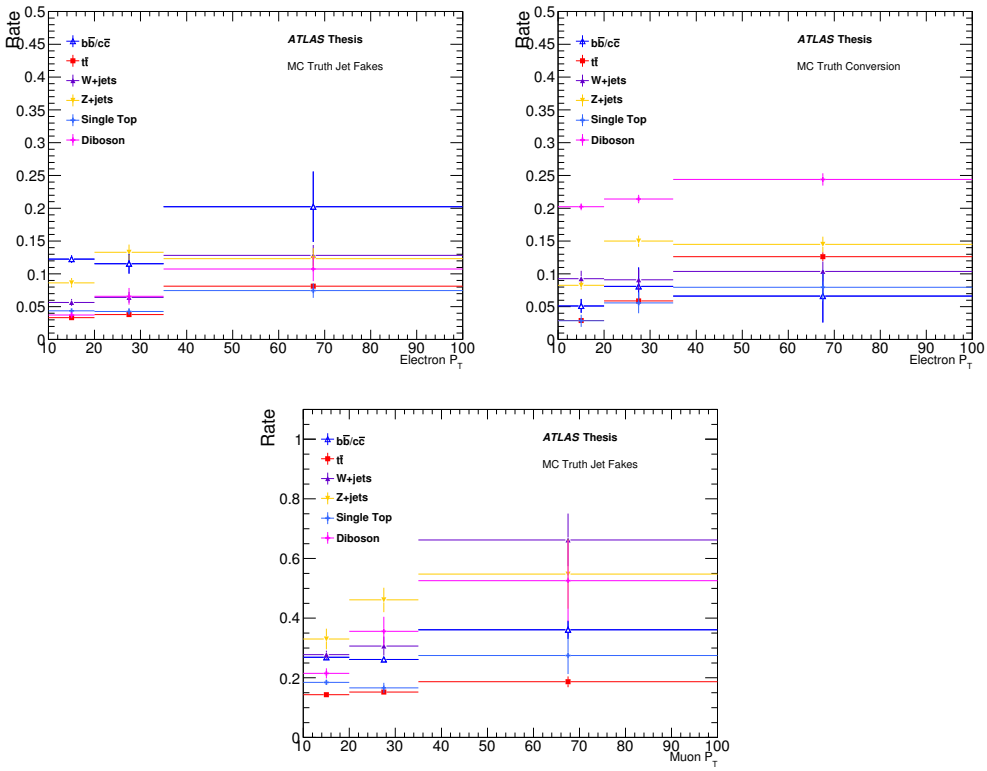

Figure 8.9: The MC fake rates for electron (top) and muon (bottom). The muon conversion rate is estimated to have negligible contributions to the signal regions and is therefore ignored. The figure contains many processes, which are listed in the legend.

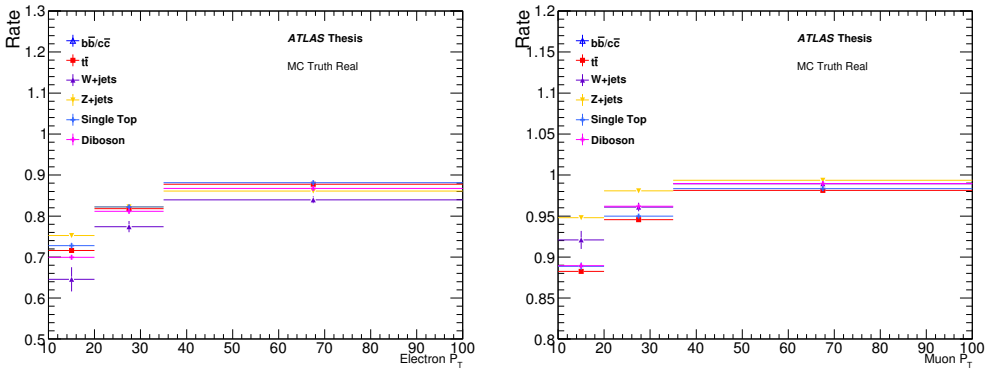

Figure 8.10: The MC real efficiency for electron (left) and muon (right). The figure contains many processes, which are listed in the legend.

The scale factors were found to be consistent with one, however the measured values were applied. The results can be found in Table 8.14.

The jet fake control region is a $b\bar{b}$ tag-and-probe region which requires:

1. Exactly two baseline leptons prior to overlap requirement outlined in Subsection 8.2.1.
2. The tag muon is required to be within $\Delta R < 0.4$ of a b-tagged jet.
3. There can be only one tag muon and only one b-tagged jet in the event.
4. The probe lepton cannot overlap with any jet.
5. Tag muon must have $p_{\mathrm{T}} > 20$ GeV
6. The transverse mass (M_T) of the probe lepton and $E_{\mathrm{T}}^{\mathrm{miss}}$must be less than 40 GeV.
7. Veto events where the probe is a muon and the dimuon mass is within 10 GeV of the Z boson mass.
8. $m(\ell\ell) > 20$ GeV when the probe is a muon.

Even with the tight selection, significant electroweak contamination was found in this region. Two methods were employed to remove this contamination. The first was a simple MC subtraction, where one takes the data and removes the MC contributions from $t\bar{t}$, V+jet, and diboson. What is left is considered to be from $b\bar{b}$ and $c\bar{c}$.

The second procedure involves an iterative subtraction in order to correct the rate measured in data for electroweak contamination. In addition to the $b\bar{b}$ tag-and-probe region defined previously, an additional region is constructed with identical selection except for the requirement on M_T is loosened to 100 GeV in order to allow more contamination into the region. The first region will be referenced as the "low" region, while the looser region ($M_T < 100$

GeV) will be referred to as the "high" region. The fake rate for iteration i is estimated in the low region as

$$f^i = \frac{N_S^{data-low} - c_S^i N_S^{MC-low}}{N_B^{data-low} - c_B^i N_B^{MC-low}}, \tag{8.10}$$

where N_B is the number of baseline leptons and N_S is the number of signal leptons. The coefficients are scale factors for the MC to adjust the expected number of events in the low region for signal and baseline leptons using a one lepton matrix method with the low M_T fake rate to estimate the number of fake leptons $N(fake)^i_{S,B}$. The scale factors are defined as

$$c^i_{S,B} = \frac{N_{S,B}^{data-high} - N(fake)^i_{S,B}}{N_{S,B}^{MC-high}}. \tag{8.11}$$

It was found that the stability for f in Equation 8.10 was reached after 10 iterations, which was then used for this analysis.

The MC subtraction and the iterative subtraction results were found to be consistent in the region where the scale factor was extracted. The iterative result was used since it was less susceptible to statistical fluctuations. The results can be found in Table 8.14.

The final scale factor needed is for the electron conversion fake rate. This is measured in a $Z \to \mu\mu + \gamma$ control region defined by the following requirements:

1. Exactly two opposite-sign signal muons and one baseline electron.
2. Require $|m(\mu\mu e) - m(Z)| < 10$ GeV.
3. Require $m(\mu\mu) > 20$ GeV.
4. Veto events with b-tagged jets.
5. Require $E_{\mathrm{T}}^{\mathrm{miss}} < 50$ GeV.

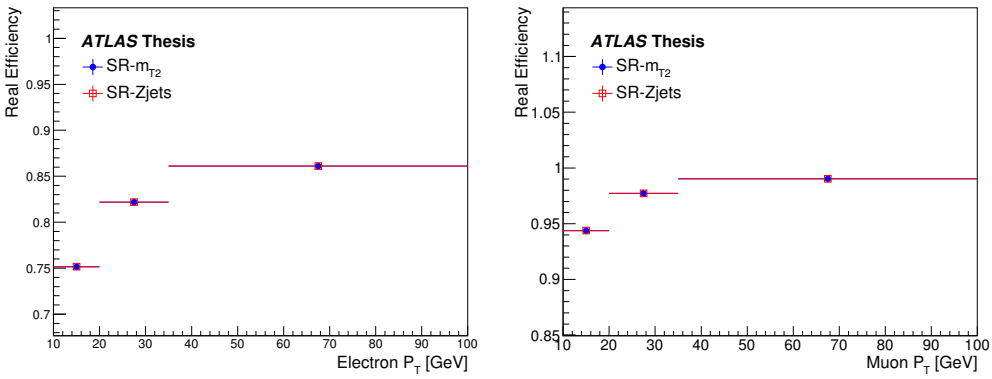

Figure 8.11: The weighted average real efficiency for electrons (left) and muons (right) constructed following Equation 8.8.

6. Transverse mass of the electron and $E_{\mathrm{T}}^{\mathrm{miss}}$ must be less than 40 GeV.

The contamination from WZ production was found to be negligible and was not subtracted from the data. The scale factor can be found in Table 8.14.

Scale Factor	e	μ
Real	1.00	1.00
Jet Fake	0.71	0.88
Conversion	1.23	–

Table 8.14: The scale factors for the real efficiency, the jet fake rate and the conversion fake rate for electrons and muons as measured in the dedicated control regions.

Final Fake Rates and Efficiencies Due to the stringent requirements on m_{T2} and $E_{\mathrm{T}}^{\mathrm{miss,rel}}$ for SR-m_{T2} and SR-Zjets there were not sufficient statistics in order to extract the region percentages (R_P in Equation 8.7, 8.8) therefore these requirements were loosened to allow fake and real leptons to populate the regions. A result of loosening this requirement is that the same fake rate and real efficiency are used for SR-m_{T2} with m_{T2} cuts at 90, 120, and 150. The weighted average real efficiencies can be found in Figure 8.11 and the weighted average fake rate can be found in Figure 8.12.

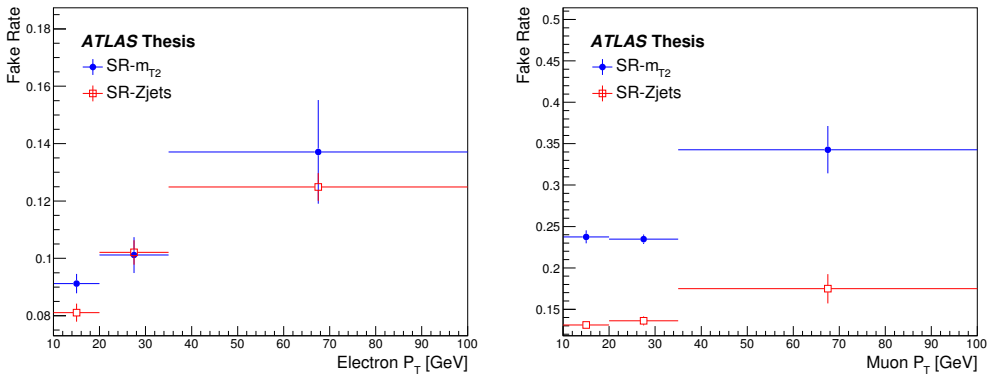

Figure 8.12: The weighted average fake rate for electrons (left) and muons (right) constructed following Equation 8.7.

Validation Region In order to assess how the fake background prediction is performing, and to assess any issues, a validation region is constructed where the background form fake leptons is dominant. The requirements for the region can be found in Table 8.15. The dilepton requirement for the ee channel is to reduce the background from the so called "charge-flip" electrons, described in Subsection 7.3.4. Therefore a window around the Z boson mass is rejected in order to have a region more enriched in fake leptons. An additional dilepton requirement is in place for $\mu\mu$ channel in order to remain orthogonal to another search.

Selection	ee	$\mu\mu$	$e\mu$
$m(\ell\ell)$	$\lvert m(\ell\ell) - m(Z)\rvert > 10$ GeV	Reject $90 < m(\ell\ell) < 120$ GeV	–
Lepton Charge	same-sign		
$E_{\mathrm{T}}^{\mathrm{miss,rel}}$	> 40 GeV		

Table 8.15: The fake validation region requirements for ee, $\mu\mu$, and $e\mu$ channels.

Overall good agreement is observed in the fake validation region. The numerical yield can be found in Table 8.16. The matrix method prediction also reproduces several kinematic variables, as can be seen in Figures 8.13 to Figures 8.16.

Process	ee	(stat)	(sys)	$\mu\mu$	(stat)	(sys)	eμ	(stat)	(sys)
Z+X	233.35	8.10	$--$	198.95	2.92	$--$	296.88	3.52	$--$
Top	56.59	0.84	$--$	6.69	0.23	$--$	68.41	0.79	$--$
WW	25.79	0.36	$--$	16.09	0.36	$--$	42.06	0.46	$--$
Fake	668.94	9.86	$^{+226.07}_{-187.54}$	570.22	15.00	$^{+72.54}_{-71.33}$	1419.45	18.45	$^{+306.92}_{-255.46}$
Total SM	984.66	12.79	$^{+226.07}_{-187.54}$	791.96	15.29	$^{+72.54}_{-71.33}$	1826.80	18.81	$^{+306.92}_{-255.46}$
Observed	969	31.13	$--$	922	30.36	$--$	1995	44.67	$--$

Table 8.16: The SM prediction and the observed events for fake validation region defined in Table 8.15. The MC samples have only the statistical error, while the fake prediction has statistical and the systematic.

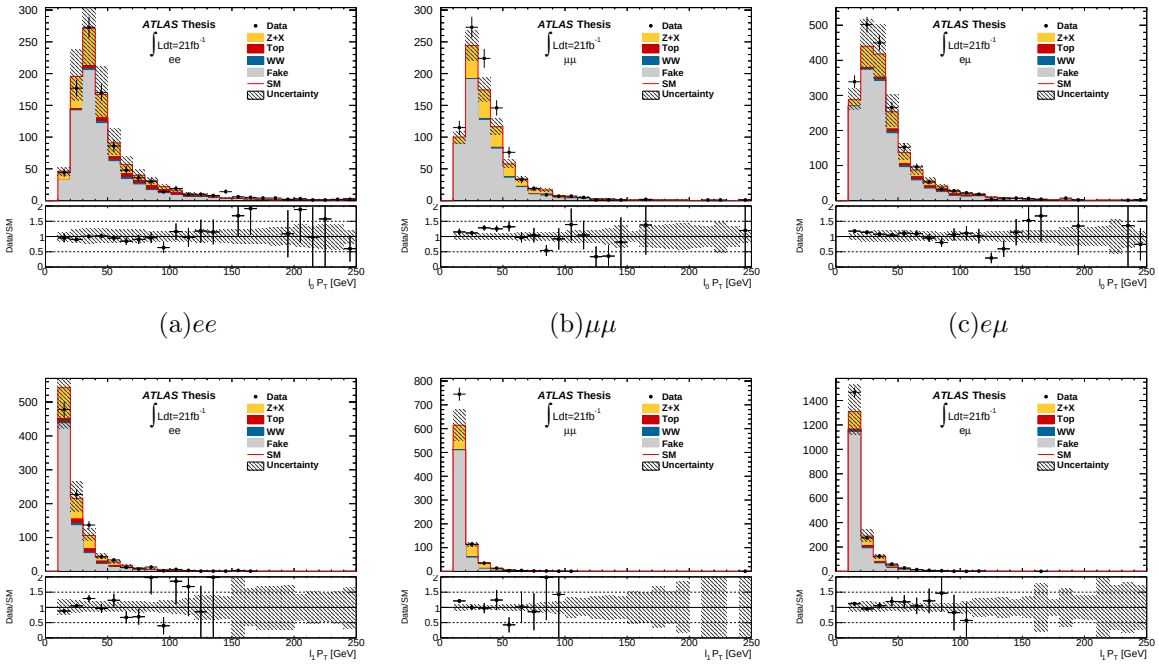

(a)ee (b)$\mu\mu$ (c)eμ

(d)ee (e)$\mu\mu$ (f)eμ

Figure 8.13: The leading (top) and subleading (bottom) lepton P_T for the ee, $\mu\mu$, and eμ channels in the validation region. The errors shown are the statistical from both MC and the matrix method prediction, as well as the systematic errors from the matrix method prediction.

Uncertainties Several sources of systematic uncertainty are considered on the method. All uncertainties are attached to the real efficiencies and fake rates and then propogated through the matrix method to the final prediction. The final uncertainy for the fake rate (real efficiency) is summarized in Table 8.17 (Table 8.18). The details for each uncertainty follow.

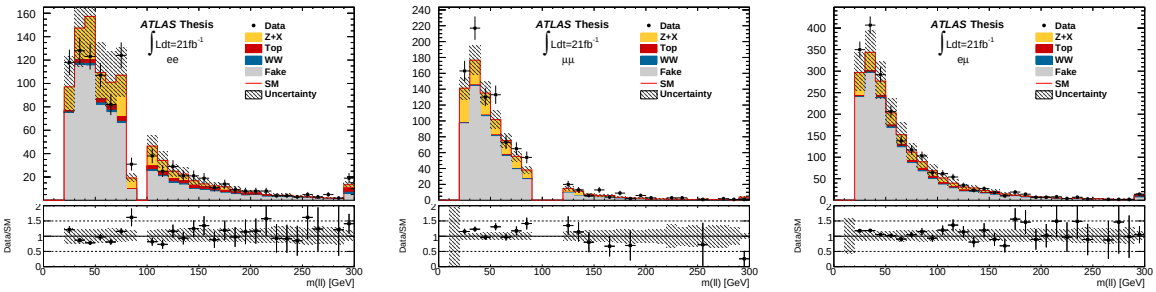

(a)ee (b)$\mu\mu$ (c)$e\mu$

Figure 8.14: The invariant mass of the dd-lepton pair for the ee, $\mu\mu$, and eμ channels in the validation region. The errors shown in the ratio are only statistical. The errors shown are the statistical from both MC and the matrix method prediction, as well as the systematic errors from the matrix method prediction.

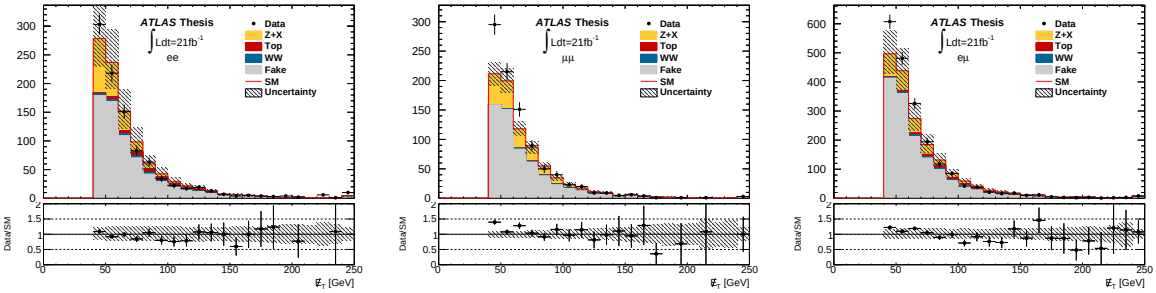

(a)ee (b)$\mu\mu$ (c)$e\mu$

Figure 8.15: The $E_{\mathrm{T}}^{\mathrm{miss}}$energy distribution for TT ee, $\mu\mu$, and eμ channels in the validation region. The errors shown in the ratio are only statistical. The errors shown are the statistical from both MC and the matrix method prediction, as well as the systematic errors from the matrix method prediction.

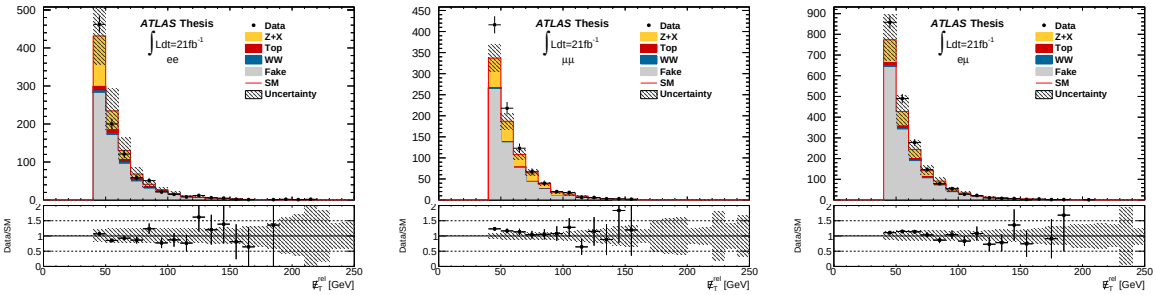

(a)ee (b)$\mu\mu$ (c)$e\mu$

Figure 8.16: The $E_{\mathrm{T}}^{\mathrm{miss,rel}}$ energy distribution for the ee, $\mu\mu$, and eμ channels in the validation region. The errors shown in the ratio are only statistical. The errors shown are the statistical from both MC and the matrix method prediction, as well as the systematic errors from the matrix method prediction.

The first uncertainty applies only to electrons, and it is the dependence on $|\eta|$. It was found that the fake rates and real efficiencies have some small η dependence. Using a parameterization of p_{T} and η was attempted, however when the MC samples were further split up large statistical fluctuations became a problem in the fake rate. For this reason, an η parameterizaiton was not used. To assess the uncertainty the p_{T} averaged fake rate is compared to the rate in two bins of $|\eta|$. The first bin ($|\eta| < 1.47$) has a downward fluctuation of 25%, while the second bin ($|\eta| > 1.47$) has an upward fluctuation of 30%.

The second source of uncertainty also only applies to electrons. The jet fake rate is composed of both light and heavy flavor jets which can have different fake rates. Measuring these two is trivial in MC, however a suitable control region in data to derive the necessary scale factor was not obtainable on the time scale of this analysis. Therefore these two rates are combined in MC, and a systematic error is assessed based on the differences observed between light flavor (LF) jet fake rate and heavy flavor (HF) jet fake rate. This was not an issue for muons, since the relative amount of HF dominates in the weighted average. The uncertainty is $\pm$ 5 %.

The next uncertainty is related to the scale factor. The scale factor is extracted by comparing the data and MC rates in the control region as a function of p_{T}. The ratio is fit with a constant. The maximum deviations with respect to this fitted value is assessed as a systematic. The final uncertainty has maximum of $\pm$ 20% ($\pm$ 5%) for electrons (muons).

The fourth uncertainty is associated with the percentage used in the weighted average fake rate (the R_P in Equation 8.7). This is evaluated in each individual signal region and control region used in this analysis for each sample, and then propagated to the final fake rate used. The maximum deviation of 5% and 10% is found for electrons and muons respectively.

The final uncertainty is the statistical uncertainty on the final fake rate and real efficiency. This is propagated to the matrix method prediction in the same fashion as the other uncer-

tainties discussed.

Systematic	Electron [%]	Muon [%]
η Dependence	[-25,30]	Within Stat Error
HF/LP	$\pm$ 5	N/A
Scale Factor	$\pm$ 20	$\pm$ 5
Region Error	$\pm$ 5	$\pm$ 10
Statistical (Maximum)	$\pm$ 14	$\pm$ 14

Table 8.17: Summary table of the various sources of systematic error and their ranges for the applied fake rate. The maximum shifts are quoted, however in some signal regions the errors can be lower. The errors in brackets implies this is taken from a distribution and those quoted with a shift up or down are flat.

Systematic	Electron [%]	Muon [%]
η Dependence	$\pm$ 2	< 1
Scale Factor	< 1	< 1
Statistical	< 1	< 1

Table 8.18: Summary table of the various sources of systematic error and their ranges for the applied real efficiency.

8.4 Signal Regions

8.4.1 SR-m_{T2}

A powerful discriminating variable has been developed [85, 86, 87, 88] in order to separate SM processes from SUSY called the "Stransverse Mass" (m_{T2}). m_{T2} is built from the reconstructed lepton momentum and the missing transverse momentum. m_{T2} is defined as,

$$m_{\mathrm{T2}} = \underset{\mathbf{q}_T}{min}[max(m_T(\mathbf{p}_T^{\ell_1}, \mathbf{q}_T), m_T(\mathbf{p}_T^{\ell_2}, \mathbf{p}_T^{miss} - \mathbf{q}_T))], \tag{8.12}$$

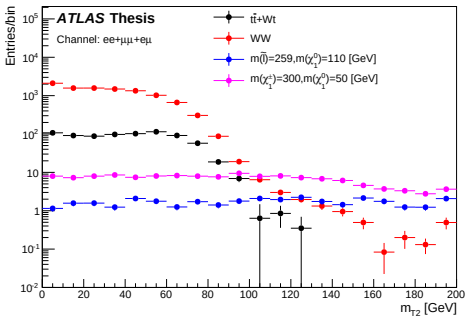

Figure 8.17: m_{T2} distribution for $t\bar{t}$+Wt, WW, and two simplified model grid points for slepton pair production and chargino pair production normalized to 20.3 fb^{-1}. The two SM backgrounds shown have a characteristic cutoff near the W mass. The two SUSY points extend well beyond the W mass.

where $\mathbf{p}_T^{\ell_1}$ and $\mathbf{p}_T^{\ell_2}$ are the transverse momentum of the two leptons in the event and $\mathbf{q}_T$ is the transverse vector that minimizes the following expression:

$$m_T(\mathbf{p}_T, \mathbf{q}_T) = \sqrt{2(p_T q_T - \mathbf{p}_T \cdot \mathbf{q}_T)}. \tag{8.13}$$

The benefit of this variable is that it can take on values between 0 and the mass of the parent particle that produced the invisible particle. This presents an upper bound for events containing SM processes such as $t\bar{t}$ and WW, in which two on-shell W bosons decay leptonicaly and the missing momentum is given by the neutrinos. For this case, m_{T2} can take on values between 0 and the mass of the W, however due to reconstruction effects and the width of the W boson mass there are small tails in the m_{T2} distribution for these processes, as shown in Figure 8.17. The signal points will have tails extending well beyond the W boson mass given that the parent particle is much heavier, thus providing a useful discriminant to separate SM processes from signal like processes.

SR-m_{T2} has three distinct regions based on the m_{T2} threshold of 90, 120, and 150 GeV. Each region has the common event quality criteria and object selection outlined in Subsection 8.2.1, with the additional requirements on dilepton mass and jets given in Table 8.19. This selection

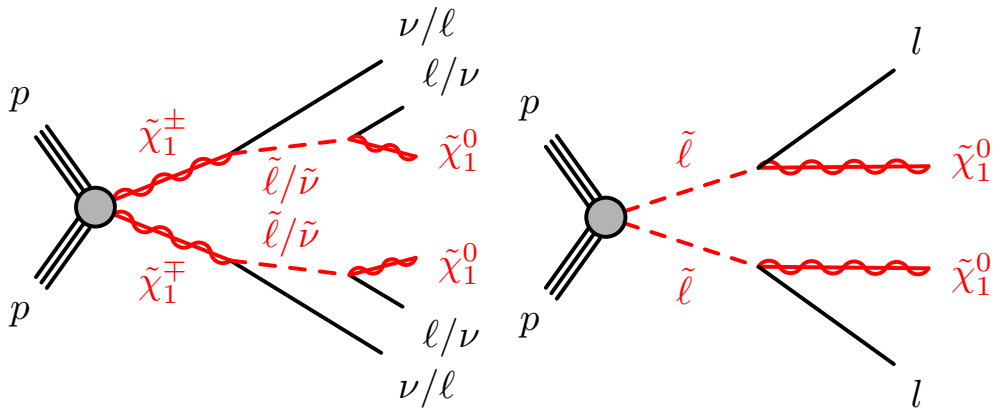

Figure 8.18: Feynman diagrams for chargino pair production with intermediate sleptons (left) and direct slepton production (right).

criteria has been optimized to target the processes in Figure 8.18. The three increasing requirements on m_{T2} are useful for targeting increased slepton or chargino masses. The regions are overlapping and cannot be statistically combined to achieve the final result, therefore the region with the best exclusion power defines the signal region for that particular grid point. The future analysis will explore the possibility of doing a shape analysis as a function of m_{T2}. Due to time constraints, this could not be done for this analysis.

Signal Region	SR-m_{T2}
charge	OS
flavor	ee,$e\mu$,$\mu\mu$
$\lvert m(\ell\ell) - m(Z)\rvert$	> 10 GeV
central light jets	$= 0$
central b-tagged jets	$= 0$
forward jets	$= 0$
m_{T2}	> 90, 120, 150 GeV

Table 8.19: Signal region requirements for SR-m_{T2}. Event quality and object selection criteria are implicitly satisfied.

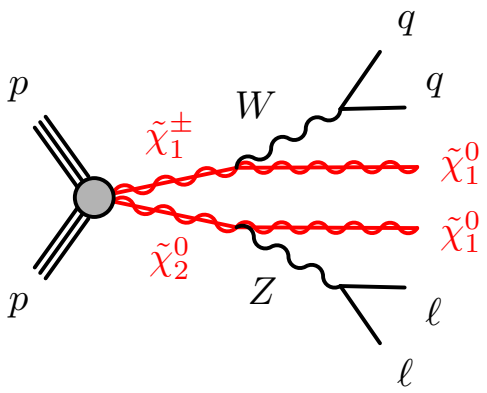

Figure 8.19: Feynman diagrams for $\tilde{\chi}_2^0$ and $\tilde{\chi}_1^{\pm}$ production with on-shell W and Z bosons.

8.4.2 SR-Zjets

For the first time at ATLAS, a search for pair production of $\tilde{\chi}_2^0\tilde{\chi}_1^{\pm}$ where $\tilde{\chi}_2^0$ decays to an on-shell Z boson and $\tilde{\chi}_1^{\pm}$ decays to an on-shell W boson has been carried out. The final state includes two same-flavor, opposite-charge leptons and two hadronic jets, as shown in Figure 8.19. Due to the different final state objects, as compared with Figure 8.18, a separate signal region has been developed.

The events are required to satisfy the selection outlined in Subsection 8.2.1, with the additional requirement that two same-flavor, opposite-charge leptons compatible with the Z boson mass be present, as well as two hadronic jets compatible with the W boson mass. After selecting events containing a Z, the dominant background becomes Z+jets and $t\bar{t}$. Several other criteria have been developed by collaborators working on this analysis to further suppress these backgrounds. The full selection for SR-Zjets can be found in Table 8.20. Requiring $m(j_0, j_1)$ to be consistent with the W boson mass is a charachteristic of the signal, but also reduces the amount of $t\bar{t}$ in the signal region. The requirements on $p_{\mathrm{T}}^{\ell\ell}$, $\Delta R(\ell, \ell)$, and $E_{\mathrm{T}}^{\mathrm{miss,rel}}$ are all used to suppress background from Z+jets events.

Signal Region	SR-Zjets
charge	OS
flavor	same-flavor
$\lvert m(\ell\ell) - m(Z)\rvert$	< 10
central light jets	≥ 2
central b-tagged jets	$= 0$
forward jets	$= 0$
p_{T}^{jet1}	> 45 GeV
p_{T}^{jet2}	> 45 GeV
$E_{\mathrm{T}}^{\mathrm{miss,rel}}$	> 80 GeV
$p_{\mathrm{T}}(\ell\ell)$	> 80 GeV
$\Delta R(\ell, \ell)$	[0.3, 1.5]
m(jet1,jet2)	[50, 100] GeV

Table 8.20: Signal region requirements for SR-Zjets. Event quality and object selection criteria are implicitly satisfied.

8.5 Results

No excess above SM prediction is observed in SR-m_{T2},90,120,150 or in SR-Zjets, as indicated in Table 8.21 and Table 8.22. A comparison between SM prediction and data for key kinematic variables can be found in Figure 8.20 for SR-m_{T2} and Figure 8.21 for SR-Zjets.

	SR-m_{T2},90			SR-m_{T2},120			SR-m_{T2},150		
Process	ee	$\mu\mu$	$e\mu$	ee	$\mu\mu$	$e\mu$	ee	$\mu\mu$	$e\mu$
$t\bar{t}+Wt$	$0.90^{+0.99}_{-0.90}$	2.14 ± 1.21	5.53 ± 1.88	$0.33^{+0.36}_{-0.33}$	0.00 ± 0.00	0.00 ± 0.00	0.00 ± 0.00	0.00 ± 0.00	0.00 ± 0.00
WW	9.22 ± 1.94	12.83 ± 2.57	16.18 ± 3.22	1.53 ± 0.65	1.96 ± 0.72	3.29 ± 1.19	0.40 ± 0.32	0.57 ± 0.29	0.90 ± 0.46
ZX	0.00 ± 0.00	$0.00^{+0.01}_{-0.00}$	0.00 ± 0.00	0.00 ± 0.00	0.00 ± 0.00	0.00 ± 0.00	0.00 ± 0.00	0.00 ± 0.00	0.00 ± 0.00
ZV	6.01 ± 1.15	6.84 ± 1.23	0.76 ± 0.22	2.18 ± 0.76	2.76 ± 0.92	0.15 ± 0.08	0.89 ± 0.23	1.26 ± 0.31	0.03 ± 0.02
$Higgs$	0.11 ± 0.04	0.08 ± 0.05	0.19 ± 0.05	0.04 ± 0.03	0.05 ± 0.02	0.10 ± 0.04	0.01 ± 0.01	0.01 ± 0.01	0.04 ± 0.03
$Fake$	$0.08^{+0.25}_{-0.08}$	$0.00^{+0.01}_{-0.00}$	0.59 ± 0.55	$0.01^{+0.10}_{-0.01}$	$0.00^{+0.34}_{-0.00}$	$0.01^{+0.09}_{-0.01}$	$0.06^{+0.12}_{-0.06}$	$0.00^{+0.35}_{-0.00}$	0.00 ± 0.37
Total SM	16.31 ± 2.50	21.89 ± 3.22	23.26 ± 3.72	4.10 ± 1.05	4.77 ± 1.17	3.55 ± 1.20	1.36 ± 0.40	1.84 ± 0.43	0.96 ± 0.46
Observed	13	20	21	3	2	5	2	1	2

Table 8.21: Predicted and observed events in SR-m_{T2},90,120,150 for ee, $\mu\mu$, and $e\mu$ events in 20.3 fb^{-1} of data. The errors shown are the statistical plus systematic uncertainties.

SR-Zjets		
Process	ee	$\mu\mu$
$t\bar{t}+Wt$	0.02 ± 0.02	0.01 ± 0.01
WW	0.00 ± 0.00	$0.07^{+0.09}_{-0.07}$
ZX	0.15 ± 0.04	0.16 ± 0.04
ZV	0.56 ± 0.36	0.41 ± 0.30
$Higgs$	0.00 ± 0.00	0.00 ± 0.00
$Fake$	$0.00^{+0.12}_{-0.00}$	$0.00^{+0.09}_{-0.00}$
Total SM	0.74 ± 0.37	0.65 ± 0.32
Observed	0	1

Table 8.22: Predicted and observed events in SR-Zjets for ee and $\mu\mu$ events in 20.3 fb^{-1} of data. The errors shown are the statistical plus systematic uncertainties.

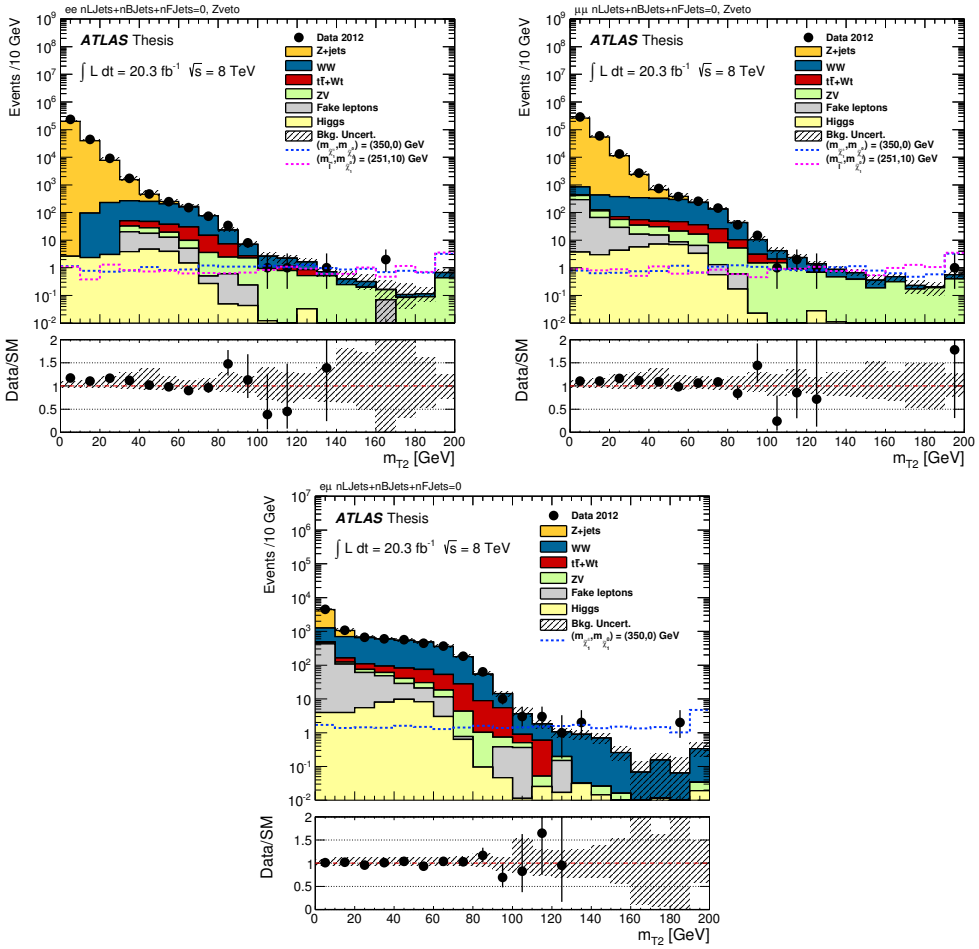

Figure 8.20: The m_{T2} distribution for SR-m_{T2} prior to the m_{T2} requirement for ee (top-left), $\mu\mu$ (top-right), and $e\mu$ (bottom). The distribution from two signal points can be found in the figure. All systematic and statistical uncertainties are included on the background estimate.

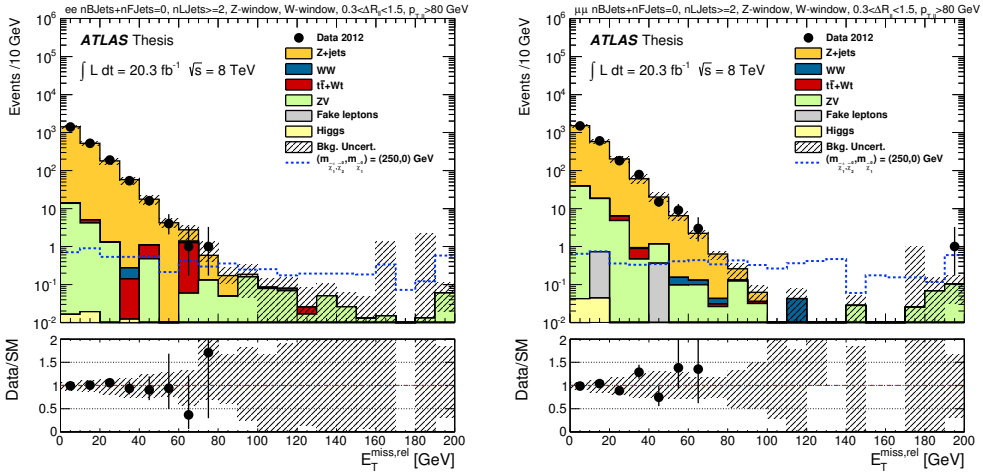

Figure 8.21: The $E_{\mathrm{T}}^{\mathrm{miss,rel}}$ distribution for SR-Zjets prior to the $E_{\mathrm{T}}^{\mathrm{miss,rel}}$ requirement for ee (left) and $\mu\mu$ (right). The distribution from two signal points can be found in the figure. All systematic and statistical uncertainties are included on the background estimate.

8.5.1 Limits

Given the good agreement observed between the SM prediction and the observed data in all signal regions, upper limits on beyond the SM cross-section in each signal region and for the simplified model grids considered. The search carried out in this dissertation is a counting experiment in the signal regions and no shape information is used to set limits.

Limits are calculated in the modified frequentist CL_S approach [89]. The frequentist approach constructs a likelihood function that is dependent on the signal strength μ and the nuisance parameters θ [90]. In order to test μ a ratio of the profiled likelihoods is taken,

$$\lambda(\mu) = \frac{L(\mu, \hat{\hat{\theta}})}{L(\hat{\mu}, \hat{\theta})}, \tag{8.14}$$

where $\hat{\theta}$ and $\hat{\mu}$ represent the most probable values for the parameters and $\hat{\hat{\theta}}$ denotes the value of θ that maximizes the likelihood [90].

The likelihood ratio ranges from 0-1, with $\lambda \approx 1$ representing good agreement between data and prediction. It is convenient to express the test statistic as a logarithm of the ratio of

likelihoods,

$$t_\mu = -2ln(\lambda(\mu)), \tag{8.15}$$

since higher values of t_μ will imply good compatibility of data with SM prediction [90]. In order to quantify the level of disagreement, the p-value is computed utilizing this test statistic,

$$p_\mu = \int_{t_{\mu,obs}}^{\text{inf}} f(t_\mu|\mu)dt_\mu, \tag{8.16}$$

where t_μ is the observed value from data and $f(t_\mu|\mu)$ is the probability distribution function (pdf) of the test statistic under the assumption of a given signal strength μ [90]. The p-value can then be computed in the signal+background and background only hypothesis by using toy experiments to obtain the CL_S value,

$$\text{CL}_S = \frac{p_{s+b}}{1 - p_b} \tag{8.17}$$

[90]. In the case of the simplified model limits if the CL_S value is less than 0.05, then the signal point is excluded at 95% confidence level.

Model dependent exclusion limits are set in the context of $\chi_1^\pm\chi_1^\mp$ production with intermediate sleptons, $\tilde{\ell}^\pm\tilde{\ell}^\mp$ production, and $\chi_2^0\chi_1^\pm$ with intermediate W and Z bosons. In the case of SR-m_{T2}, the various signal regions are nested and are therefore not mutually exclusive. In this scenario, the best expected limit defines which signal region will be chosen.

Chargino pair production with intermediate sleptons The 95% CL exclusion limits for direct chargino pair production for the simplified model can be found in Figure 8.22. The exclusion limit for allowed $\tilde{\chi}_1^\pm$ has been extended by over 100 GeV in the case of massless $\tilde{\chi}_1^0$

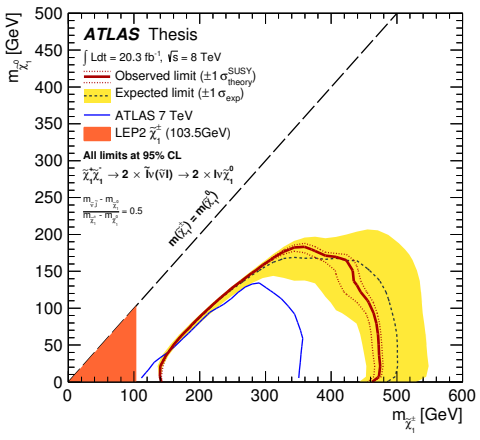

Figure 8.22: The 95% CL exclusion limit for $\tilde{\chi}_1^{\pm}\tilde{\chi}_1^{\mp}$ pair production in the simplified model with sleptons and sneutrinos. The solid red line represents the observed exclusion limit. The dashed red lines surrounding this represent the $\pm 1\sigma$ uncertainty obtained when shifting the cross-section up and down by $\pm 1\sigma$ to account for the theoretical uncertainty. The grey dashed line represents the expected exclusion limit, and the yellow band around this is representative of the $\pm 1\sigma$ result when all uncertainties, except the signal cross-section uncertainty, are included.

when compared with the 7 TeV result.

Slepton pair production In the case of direct slepton pair production, limits are set for a variety of scenarios. The combined selectron and smuon exclusion limits can be found in Figure 8.23 for right-handed, left-handed, and the combined right-handed and left-handed scenario. The individual slepton cases for selectron (smuon) and be seen in Figure 8.24 (Figure 8.25). These results cannot be directly compared to the previous ATLAS slepton limits in [91] which used a flavor-blind signal region and searched for a single slepton flavor with both right-handed and left-handed contributions.

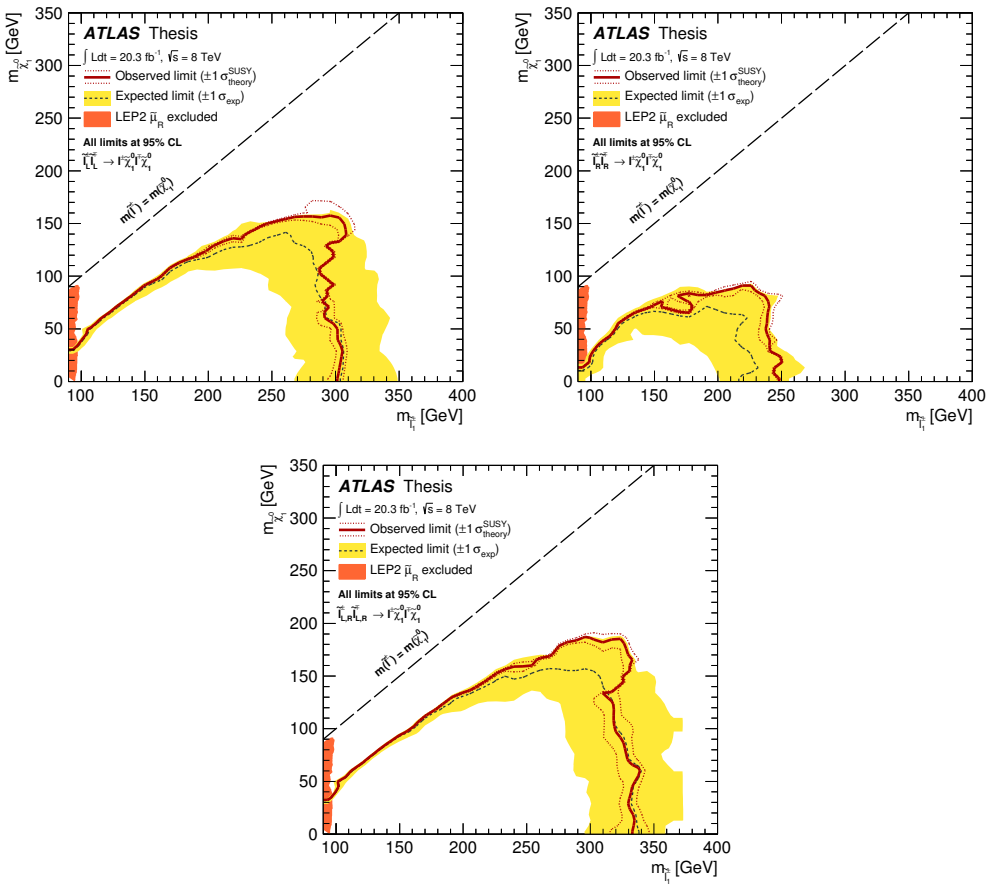

Figure 8.23: The 95% CL exclusion limit for $\tilde{\ell}_L^{\pm}\tilde{\ell}_L^{\mp}$ (top-left), $\tilde{\ell}_R^{\pm}\tilde{\ell}_R^{\mp}$ (top-right) and $\tilde{\ell}^{\pm}\tilde{\ell}^{\mp}$ (bottom) pair production in the simplified model. The solid red line represents the observed exclusion limit. The dashed red lines surrounding this represent the $\pm 1\sigma$ uncertainty obtained when shifting the cross-section up and down by $\pm 1\sigma$ to account for the theoretical uncertainty. The grey dashed line represents the expected exclusion limit, and the yellow band around this is representative of the $\pm 1\sigma$ result when all uncertainties, except the signal cross-section uncertainty, are included.

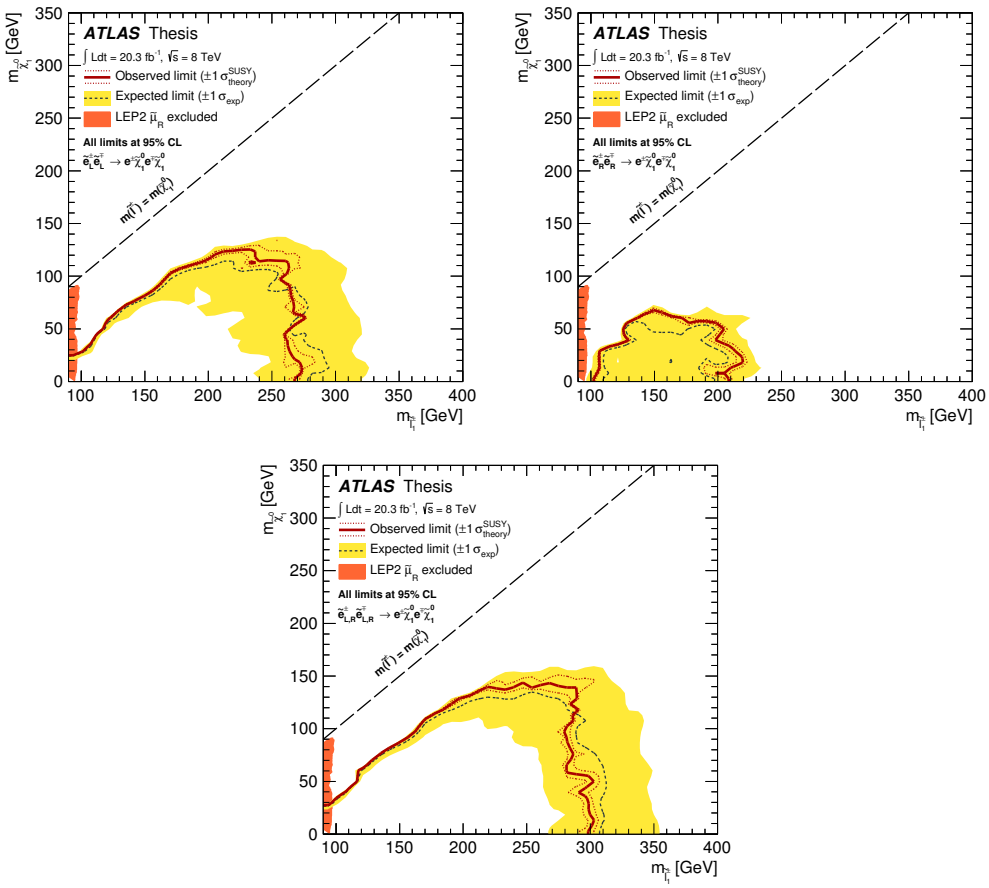

Figure 8.24: The 95% CL exclusion limit for $\tilde{e}_L^{\pm}\tilde{e}_L^{\mp}$ (top-left), $\tilde{e}_R^{\pm}\tilde{e}_R^{\mp}$ (top-right) and $\tilde{e}^{\pm}\tilde{e}^{\mp}$ (bottom) pair production in the simplified model. The solid red line represents the observed exclusion limit. The dashed red lines surrounding this represent the $\pm 1\sigma$ uncertainty obtained when shifting the cross-section up and down by $\pm 1\sigma$ to account for the theoretical uncertainty. The grey dashed line represents the expected exclusion limit, and the yellow band around this is representative of the $\pm 1\sigma$ result when all uncertainties, except the signal cross-section uncertainty, are included.

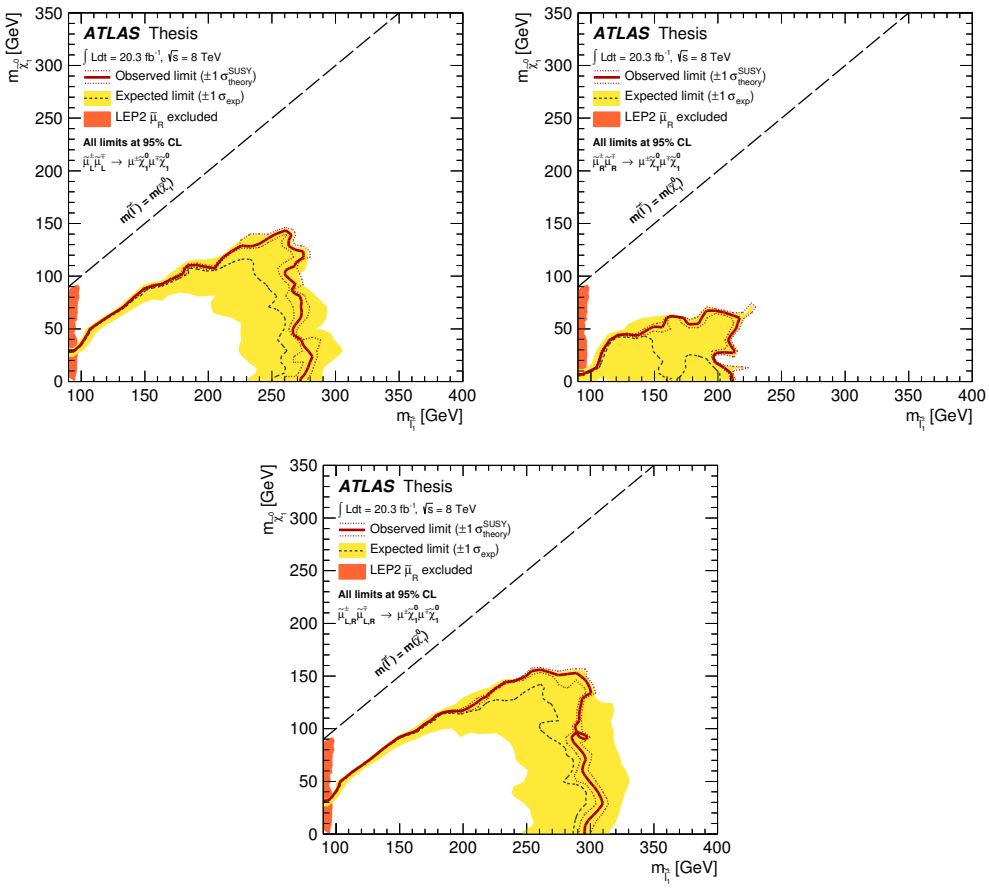

Figure 8.25: The 95% CL exclusion limit for $\tilde{\mu}_L^{\pm}\tilde{\mu}_L^{\mp}$ (top-left), $\tilde{\mu}_R^{\pm}\tilde{\mu}_R^{\mp}$ (top-right) and $\tilde{\mu}^{\pm}\tilde{\mu}^{\mp}$ (bottom) pair production in the simplified model. The solid red line represents the observed exclusion limit. The dashed red lines surrounding this represent the $\pm 1\sigma$ uncertainty obtained when shifting the cross-section up and down by $\pm 1\sigma$ to account for the theoretical uncertainty. The grey dashed line represents the expected exclusion limit, and the yellow band around this is representative of the $\pm 1\sigma$ result when all uncertainties, except the signal cross-section uncertainty, are included.

$\tilde{\chi}_1^{\pm}\tilde{\chi}_2^0$ production The exclusion limit for the simplified model targeting $\tilde{\chi}_1^{\pm}\tilde{\chi}_2^0$ production with an on shell W and Z boson is shown in Figure 8.26. The mass range from 175 to 368 is excluded at 95% CL for degenerate $\tilde{\chi}_1^{\pm}$ and $\tilde{\chi}_2^0$ in the case of a massless $\tilde{\chi}_1^0$. These results represent the first search ever performed in this complicated channel.

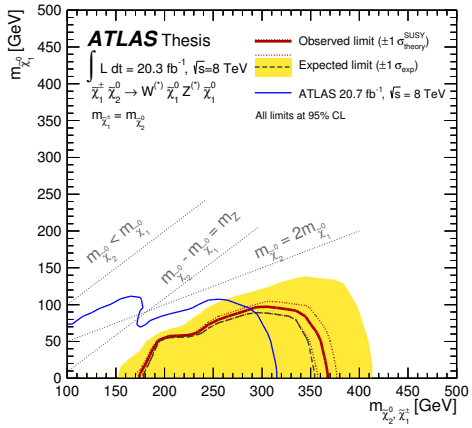

Figure 8.26: The 95% CL exclusion limit for $\tilde{\chi}_1^{\pm}\tilde{\chi}_2^0$ pair production with in the simplified model with intermediate W and Z. The solid red line represents the observed exclusion limit. The dashed red lines surrounding this represent the $\pm 1\sigma$ uncertainty obtained when shifting the cross-section up and down by $\pm 1\sigma$ to account for the theoretical uncertainty. The grey dashed line represents the expected exclusion limit, and the yellow band around this is representative of the $\pm 1\sigma$ result when all uncertainties, except the signal cross-section uncertainty, are included.

Model Independent Limits Model independent upper limits are set on the visible cross-section $\sigma_{vis} = \sigma \cdot A \cdot \epsilon$, where A and ϵ are the analysis acceptance and efficiency, respectively. Each limit is calculated using the CL_S prescription described previously at 95% confidence level. Unlike the model dependent limits, there is no signal hypothesis in this case. The background prediction is compared directly with the observed data to obtain an upper bound on the allowed cross-section for some new physics process contributing to the signal region but still remaining consitent with the observation. The results for each signal region are summarized in Table 8.23.

Signal channel	$\langle\epsilon\sigma\rangle^{95}_{\text{obs}}$[fb]	S^{95}_{obs}	S^{95}_{exp}	CL_B	$p(s=0)$
SRm_{T2},90 $ee+\mu\mu$	0.56	11.3	$14.5^{+6.2}_{-4.3}$	0.24	0.50
SR-m_{T2},90 $e\mu$	0.51	10.4	$11.6^{+5.2}_{-3.4}$	0.38	0.50
SR-m_{T2},120 $ee+\mu\mu$	0.23	4.7	$7.3^{+3.6}_{-2.2}$	0.13	0.50
SR-m_{T2},120 $e\mu$	0.35	7.2	$6.5^{+3.0}_{-1.8}$	0.59	0.36
SR-m_{T2},150 $ee+\mu\mu$	0.24	4.8	$5.0^{+2.7}_{-1.7}$	0.47	0.50
SR-m_{T2},150 $e\mu$	0.24	4.8	$3.5^{+2.2}_{-1.3}$	0.74	0.19
SR-Zjets $ee+\mu\mu$					

Table 8.23: Left to right: 95% CL upper limits on the visible cross section ($\langle\epsilon\sigma\rangle^{95}_{\text{obs}}$) and on the number of signal events (S^{95}_{obs}). The third column (S^{95}_{exp}) shows the 95% CL upper limit on the number of signal events, given the expected number (and $\pm1\sigma$ excursions on the expectation) of background events. The last two columns indicate the CL_B value, i.e. the confidence level observed for the background-only hypothesis, and the discovery p-value ($p(s=0)$), which is a statement of how consistent the observed events are with the SM prediction in the absence of a new physics signal.

Chapter 9

Conclusions

A search for new physics signals using final states with exactly two leptons in order to explain the observed neutrino masses and find a particle dark matter candidate have been presented. The observed events in all signal regions were found to be consistent with the standard model, which resulted in stringent bounds on theoretical models for heavy neutrino, direct gaugino, and direct slepton production.

In addition to the searches for new physics, an analysis to calibrate the energy of hadronic jets has been presented. This analysis utilized a novel technique that exploited the most coveted law of physics: energy conservation. The results of this analysis have been used to provide excellent agreement for the calibrated jet energy between data and MC, as well as reduce the overall uncertainty on this measurement. All physics analyses using jets have gained from this work.

The ATLAS community continues to mark dead-ends on our map, and the theory community has responded to the null results by presenting new directions to be explored. It is only a matter of time and dedication from the analyzers before physicists are able to find the right path for physics beyond the Standard Model.

Bibliography

[1] W. Beenakker, M. Klasen, M. Kramer, T. Plehn, M. Spira, *et al.*, "The Production of charginos/neutralinos and sleptons at hadron colliders," *Phys. Rev. Lett.* **83** (1999) 3780–3783, arXiv:hep-ph/9906298 [hep-ph].

[2] W.M. Alberico, S.M. Bilenky, Phys. Part. Nucl. **35**, 297 (2004), and references therein.

[3] T. Araki *et al.* (KamLAND Collaboration), "Measurement of neutrino oscillation with kamland: Evidence of spectral distortion," *Phys. Rev. Lett.* **94** (2005) 081801.

[4] S. van den Bergh, "The early history of dark matter," astro-ph/9904251.

[5] G. Altarelli, "Collider Physics within the Standard Model: a Primer," arXiv:1303.2842 [hep-th].

[6] **ATLAS** Collaboration, "Observation of a new particle in the search for the Standard Model Higgs boson with the ATLAS detector at the LHC," *Phys.Lett.B* (2012) , 1207.7214 [hep-ex].

[7] S. Chatrchyan *et al.*, "Observation of a new boson at a mass of 125 GeV with the CMS experiment at the LHC," *Phys.Lett.B* (2012) , 1207.7235 [hep-ex].

[8] R. N. Mohapatra and G. Senjanovic, "Neutrino Mass and Spontaneous Parity Violation," *Phys. Rev. Lett.* **44** (1980) 912.

[9] R. N. Mohapatra and G. Senjanovic, "Neutrino Masses and Mixings in Gauge Models with Spontaneous Parity Violation," *Phys. Rev.* **D23** (1981) 165.

[10] A. Davidson and K. C. Wali, "Family Mass Hierarchy from Universal Seesaw Mechanism," *Phys. Rev. Lett.* **60** (1988) 1813.

[11] A. Atre, T. Han. S. Pascoli, B. Zhang, "The Search for Heavy Majorana Neutrino," *JHEP* **0905** (2009) 030.

[12] S. P. Martin, "A supersymmetry primer," hep-ph/9709356.

[13] I. . Paul Langacker, *The Standard Model and Beyond*. CRC Press, 2010.

[14] L.susskind, phys. rev. d 20 (1979) 2619; s. dimopoulos and l. susskind, nucl. phys. b155 (1979) 237; e. eichten and k.d. lane, phys. lett. b90 (1980) 125.

[15] G. D. Nima Arkani-Hamed, Savas Dimopoulos, "The hierarchy problem and new dimensions at a millimeter," arXiv:hep-ph/9803315.

[16] Nima Arkani-Hamed, A.G. Cohen, E. Katz, A.E. Nelson, "The littlest higgs," arXiv:hep-ph/0206021.

[17] M. S. David E. Kaplan, "The little higgs from a simple group," arXiv:hep-ph/0302049.

[18] C. F. Berger, J. S. Gainer, J. L. Hewett, and T. G. Rizzo, "Supersymmetry without prejudice," *JHEP* **0902** (2009) 023, 0812.0980 [hep-ph].

[19] **ATLAS** Collaboration, "The ATLAS experiment at the CERN Large Hadron Collider," *JINST* **3** no. S08003, (2008) .

[20] **ATLAS** Collaboration, "Luminosity determination in pp collisions at sqrt(s)=7 tev using the atlas detector at the lhc," *Eur. Phys. J.* **C71** (2011) 1630.

[21] **ATLAS** Collaboration, "Updated Luminosity Determination in pp Collisions at $\sqrt{s}$=7 TeV using the ATLAS Detector." ATLAS-CONF-2011-011, https://cds.cern.ch/record/1334563.

[22] **ATLAS** Collaboration, "Expected electron performance in the ATLAS experiment," ATL-PHYS-PUB-2011-006, CERN, Geneva, Apr, 2011.

[23] Z. van Kesteren, *Identification of muons in ATLAS*. PhD thesis, Universiteit van Amsterdam, 2010.

[24] M. Cacciari, G. P. Salam, and G. Soyez, "The anti-k$_T$ jet clustering algorithm," *JHEP* **04** (2008) 063, arXiv:0802.1189 [hep-ph].

[25] **ATLAS** Collaboration, "Jet energy measurement with the ATLAS detector in proton-proton collisions at $\sqrt{s} = 7$ TeV," *EPJC* **73** (2013) 2304, arXiv:1112.6426 [hep-ex].

[26] **ATLAS** Collaboration, "Performance of the atlas secondary vertex b-tagging algorithm in 7 tev collision data,".

[27] **ATLAS** Collaboration, "Impact parameter-based b-tagging algorithms in the 7 tev collision data with the atlas detector: the trackcounting and jetprob algorithms,".

[28] **ATLAS** Collaboration, "Commissioning of the ATLAS high-performance b-tagging algorithms in the 7 TeV collision data." ATLAS-CONF-2011-102, http://cdsweb.cern.ch/record/1369219.

[29] **ATLAS** Collaboration, "Jet energy measurement with the ATLAS detector in proton-proton collisions at $\sqrt{s} = 7$ TeV," *Eur. Phys. J.* **C73** (2013) 2304, arXiv:1112.6426 [hep-ex].

[30] **ATLAS** Collaboration, "Pile-up corrections for jets from proton-proton collisions at $\sqrt{s} = 7$ TeV in ATLAS in 2011." ATLAS-CONF-2012-064, `http://cds.cern.ch/record/1459529`.

[31] **ATLAS** Collaboration, "Jet energy scale and its systematic uncertainty in proton-proton collisions at $\sqrt{s} = 7$ TeV with ATLAS 2011 data ." ATLAS-CONF-2013-004, `http://cds.cern.ch/record/1509552`.

[32] **ATLAS** Collaboration, "Probing the measurement of jet energies with the ATLAS detector using photon+jet events in proton-proton collisions at $\sqrt{s} = 7$ TeV." Atlas-conf-2012-063 `http://cds.cern.ch/record/1459528` (2011).

[33] **ATLAS** Collaboration, "Measurement of the inclusive isolated prompt photon cross section in pp collisions at $\sqrt{s} = 7$ TeV with the ATLAS detector," *Phys. Rev. D* **83** (2011) , `arXiv:1012.4389 [hep-ex]`.

[34] **ATLAS** Collaboration, "Electron performance measurements with the ATLAS detector using the 2010 LHC proton-proton collision data," *EPJC* **72** (2012) , `arXiv:1110.3174 [hep-ex]`.

[35] "Pythia generator." `http://home.thep.lu.se/~torbjorn/Pythia.html`.

[36] G. Marchesini, B. R. Webber, G. Abbiendi et al., Comput. Phys. Commun. 67, 465 (1992); G. Corcella, I. G. Knowles, G. Marchesini et al., JHEP 0101, 010 (2001); G. Corcella et al., HERWIG 6.5 release note, CERN-TH/2002-270 (2005) [hep-ph/0210213v2].

[37] F. Aguila, S. Bar-Shalom, A. Soni, J. Wudka, "Heavy majorana neutrinos in the effective lagrangian description: Application to hadron colliders," *Phys. Lett.* **B670** (2009) 399.

[38] R. N. Mohapatra, ISBN 0-387-95534-8, *Unification and Supersymmetry*. Springer-Verlag, 3rd ed., 2002.

[39] K. Huitu *et al.*, "Doubly charged higgs at lhc," *Nucl. Phys.* **B487** (1997) 27.

[40] R. N. Mohapatra and P. B. Pal, ISBN 981-238-070-1, *Massive Neutrinos in Physics and Astrophysics*. World Scientific, 3rd ed., 2004.

[41] **ATLAS** Collaboration, "Electron performance measurements with the atlas detector using the 2010 lhc proton-proton collision data," *Eur. Phys. J.* **C72** (2012) 1909.

[42] S. Frixione and B. R. Webber, "Matching NLO QCD computations and parton shower simulations," *JHEP* **0206** (2002) 029.

[43] S. Frixione, P. Nason, and B. R. Webber, "Matching NLO QCD and parton showers in heavy flavour production," *JHEP* **0308** (2003) 007.

[44] S. Frixione, E. Laenen, P. Motylinski, and B. R. Webber, "Single-top production in MC@NLO," *JHEP* **0603** (2006) 092.

[45] J. Pumplin, D. Stump, J. Huston, H. Lai, P. M. Nadolsky, *et al.*, "New generation of parton distributions with uncertainties from global QCD analysis," *JHEP* **0207** (2002) 012, arXiv:hep-ph/0201195 [hep-ph].

[46] G. Corcella *et al.*, "HERWIG 6: An event generator for hadron emission reactions with interfering gluons (including supersymmetric processes)," *JHEP* **0101** (2001) 010, arXiv:hep-ph/0011363.

[47] J. Alwall, M. Herquet, F. Maltoni, O. Mattelaer, and T. Stelzer, "MadGraph 5 : Going Beyond," *JHEP* **1106** (2011) 128, arXiv:1106.0522 [hep-ph].

[48] M. L. Mangano, M. Moretti, F. Piccinini, R. Pittau, and A. D. Polosa, "Alpgen, a generator for hard multiparton processes in hadronic collisions," *JHEP* **0307** (2003) 001, arXiv:hep-ph/0206293.

[49] **ATLAS** Collaboration, "Muon reconstruction efficiency in reprocessed 2010 LHC p-p collision data recorded with the ATLAS detector." ATLAS-CONF-2011-063, http://cds.cern.ch/record/1345743.

[50] **ATLAS** Collaboration, "ATLAS Muon Momentum Resolution in the First Pass Reconstruction of the 2010 p-p Collision Data at $\sqrt{s} = 7$ TeV." ATLAS-CONF-2011-046, http://cds.cern.ch/record/1338575.

[51] **ATLAS** Collaboration, "Single and diboson production cross sections in pp collisions at $\sqrt{s}$s=7 TeV," *ATL-COM-PHYS-2010-695* (2010) .

[52] **ATLAS** Collaboration, "Monte carlo samples used for top physics," *ATL-COM-PHYS-2010-836* (2010) .

[53] **ATLAS** Collaboration, "Search for anomalous production of prompt like-sign muon pairs," *ATL-COM-PHYS-2011-979* (2011) .

[54] M. Botje et al., "The pdf4lhc working group interim recommendations," arXiv:1101.0538v1 [hep-ph].

[55] **ATLAS** Collaboration, "Search for same-sign top-quark production and fourth-generation down-type quarks in pp collisions at $\sqrt{s} = 7$ TeV with the ATLAS detector," *JHEP* **1204** (2012) 069, 1202.5520 [hep-ex].

[56] **ATLAS** Collaboration, "Measurement of the top quark-pair production cross section with ATLAS in pp collisions at $\sqrt{s} = 7$ TeV," *Eur. Phys. J.* **C71** (2011) 1577, arXiv:1012.1792 [hep-ex].

[57] T. Junk, "Confidence level computation for combining searches with small statistics," *Nucl. Instrum. Meth.* **A434** (1999) 435.

[58] M. Bahr *et al.*, "Herwig++ Physics and Manual," *Eur. Phys. J.* **C58** (2008) 639–707, arXiv:0803.0883 [hep-ph].

[59] S. Dube, J. Glatzer, S. Somalwar, A. Sood, and S. Thomas, "Addressing the multi-channel inverse problem at high energy colliders: A model independent approach to the search for new physics with trileptons," *J.Phys.G* **G39** (2012) 085004, arXiv:0808.1605 [hep-ph].

[60] S. AbdusSalam, B. Allanach, H. Dreiner, J. Ellis, U. Ellwanger, *et al.*, "Benchmark Models, Planes, Lines and Points for Future SUSY Searches at the LHC," *Eur. Phys. J.* **C71** (2011) 1835, arXiv:1109.3859 [hep-ph].

[61] LEP SUSY Working Group (ALEPH, DELPHI, L3, OPAL). Notes LEPSUSYWG/01-03.1, 04-01.1, http://lepsusy.web.cern.ch/lepsusy/Welcome.html.

[62] **ATLAS** Collaboration, "Search for direct slepton and gaugino production in final states with hadronic taus and missing transverse momentum with the ATLAS detector in pp collisions at $\sqrt{s} = 8$ TeV ." ATLAS-CONF-2013-028, https://cds.cern.ch/record/1525889.

[63] **ATLAS** Collaboration, "Susy searches in the final states with three leptons and missing transverse momentum at atlas (direct gaugino support note for multileptons)," ATL-COM-PHYS-2011-1725, CERN, Geneva, 2011. https://cdsweb.cern.ch/record/1408811.

[64] **ATLAS** Collaboration, "Identification of the Hadronic Decays of Tau Leptons in 2012 Data with the ATLAS Detector." ATLAS-CONF-2013-064, http://http://cds.cern.ch/record/1562839.

[65] P. M. Nadolsky et al., Phys. Rev. D78 (2008) 013004.

[66] S. Frixione, P. Nason, and C. Oleari, "Matching NLO QCD computations with Parton Shower similations: the POWHEG method," *JHEP* **0711** (2007) 070.

[67] B. P. Kersevan and E. Richter-Was, "The Monte Carlo event generator AcerMC version 2.0 with interfaces to PYTHIA 6.2 and HERWIG 6.5," arXiv:hep-ph/0405247.

[68] A. Lazopoulos, T. McElmurry, K. Melnikov, and F. Petriello, "Next-to-leading order QCD corrections to $t\bar{t}Z$ production at the LHC," *Phys. Lett.* **B666** (2008) 62–65, arXiv:0804.2220 [hep-ph].

[69] J. M. Campbell and R. K. Ellis, "$t\bar{t}W^{\pm}$ production and decay at NLO," *JHEP* **1207** (2012) 052, arXiv:1204.5678 [hep-ph].

[70] M. Garzelli, A. Kardos, C. Papadopoulos, and Z. Trocsanyi, "$t\bar{t}$ $W^{\pm}$ and $t\bar{t}$ Z hadroproduction at NLO accuracy in QCD with parton shower and hadronization effects," *JHEP* **1211** (2012) 056, arXiv:1208.2665 [hep-ph].

[71] T. Binoth, M. Ciccolini, N. Kauer, and M. Kramer, "Gluon-induced W-boson pair production at the LHC," *JHEP* **0612** (2006) 046, arXiv:hep-ph/0611170.

[72] T. Binoth, N. Kauer, and P. Mertsch, "Gluon-induced QCD corrections to $pp \to ZZ \to \ell\bar{\ell}\ell'\bar{\ell}'$," arXiv:0807.0024 [hep-ph].

[73] P. Artoisenet *et al.*, "A framework for Higgs characterisation," arXiv:1306.6464 [hep-ph].

[74] T. Gleisberg *et al.*, "Event generation with sherpa 1.1," *JHEP* **0902** (2009) 007.

[75] J. Pumplin et al., New generation of parton distributions with uncertainties from global QCD analysis, JHEP 07 (2002) 012.

[76] **ATLAS** Collaboration, "In situ jet pseudorapidity intercalibration of the ATLAS detector using dijet events in $\sqrt{s} = 7$ TeV proton-pr oton 2011 data." ATLAS-CONF-2012-124, http://cds.cern.ch/record/1474490.

[77] **ATLAS** Collaboration, "Probing the measurement of jet energies with the ATLAS detector using photon+jet events in proton-proton collisions at $\sqrt{s} = 7$ TeV." ATLAS-CONF-2012-063, http://cds.cern.ch/record/1459528.

[78] **ATLAS** Collaboration, "Probing the measurement of jet energies with the ATLAS detector using Z+jet events from proton-proton collisions at $\sqrt{s} = 7$ TeV." ATLAS-CONF-2012-053, http://cds.cern.ch/record/1452641.

[79] **ATLAS** Collaboration, "Jet energy resolution and selection efficiency relative to track jets from in-situ techniques with the atlas detector using proton-proton collisions at a center of mass energy $\sqrt{s} = 7$ TeV." ATLAS-CONF-2010-054, 2010.

[80] **ATLAS** Collaboration, "Measuring the b-tag efficiency in a ttbar sample with 4.7 fb^{-1} of data from the ATLAS detector." ATLAS-CONF-2012-097, http://cds.cern.ch/record/1460443.

[81] **ATLAS** Collaboration, "A measurement of the muon reconstruction efficiency in 2010 ATLAS data using J/ψ decays." ATLAS-CONF-2012-125, https://cds.cern.ch/record/1474642.

[82] G. Cowan, K. Cranmer, E. Gross, and O. Vitells, "Power-Constrained Limits," arXiv:1105.3166 [physics.data-an].

[83] **ATLAS** Collaboration, "Search for squarks and gluinos using final states with jets and missing transverse momentum with the ATLAS detector in $\sqrt{s} = 7$ TeV proton-proton collisions," *Phys.Lett.* **B701** (2011) 186–203, arXiv:1102.5290 [hep-ex].

[84] **ATLAS** Collaboration, "Search for supersymmetry in final states with jets, missing transverse momentum and a Z boson a t $\sqrt{s} = 8$ TeV with the ATLAS detector." ATLAS-CONF-2012-152, http://cds.cern.ch/record/1493491.

[85] C. G. Lester and D. J. Summers, "Measuring masses of semi-invisibly decaying particles pair produced at hadron colliders," *Phys. Lett.* **B463** (1999) 99–103, arXiv:hep-ph/9906349.

[86] A. Barr, C. Lester, and P. Stephens, "m(T2) : The Truth behind the glamour," *J. Phys.* **G29** (2003) 2343–2363, arXiv:hep-ph/0304226.

[87] D. Tovey, "On measuring the masses of pair-produced semi-invisibly decay ing particles at hadron colliders," *JHEP* **0804** (2008) 034.

[88] D. Costanzo and D. R. Tovey *JHEP* **04** (2009) 084.

[89] A. L. Read, "Presentation of search results: The CL_s technique," *J. Phys.* **G28** (2002) 2693–2704.

[90] G. Cowan, K. Cranmer, E. Gross, and O. Vitells, "Asymptotic formulae for likelihood-based tests of new physics," *EPJ* **C71** (Feb., 2011) 1554, 1007.1727 [physics.data-an].

[91] **ATLAS** Collaboration, "Search for direct slepton and gaugino production in final states with two leptons and missing transverse momentum with the ATLAS detector in pp collisions at $\sqrt{s} = 7$ TeV," *Phys. Lett.* **B718** (2013) 879–901, arXiv:1208.2884 [hep-ex].